

TECHNICAL
LIBRARY

Normal and Oblique Impact of Cylindro-Conical and Cylindrical Projectiles on Metallic Plates

by
Werner Goldsmith
University of California, Berkeley
and
S. A. Finnegan
Research Department

JUNE 1985

**NAVAL WEAPONS CENTER
CHINA LAKE, CA 93555-6001**



Approved for public release; distribution is unlimited.

DTIC QUALITY INSPECTED 3

19970805 118

Naval Weapons Center

AN ACTIVITY OF THE NAVAL MATERIAL COMMAND

FOREWORD

This work constitutes a collaborative effort between the Department of Mechanical Engineering, University of California, Berkeley and the Engineering Sciences Division, Naval Weapons Center, China Lake, performed under the sponsorship of the Army Office of Research pursuant to Contract DAAG29-80-K-0052. The technical monitor on this contract was Dr. E. A. Saibel, Army Research Office. The investigation was executed during the period from June 1982 to January 1984. It is part of a continuing investigation involving the impact on plates by projectiles. The authors are grateful to the following individuals whose assistance immeasurably aided the execution of this project: Mr. S. Vorestek, Mr. M. Shary, Mr. J. Dual, Mr. D. Chen, Dr. J. Liss, Dr. B. Landkof, and Mr. N. Levy.

This report was reviewed for technical accuracy by Jan C. Schulz.

Approved by
E. B. ROYCE
Head, Research Department
22 January 1985

Under authority of
K. A. DICKERSON
Capt., USN
Commander

Released for publication by
B. W. HAYS
Technical Director

NWC Technical Publication 6479

Published by Research Department
Collation Cover, 56 leaves
First printing 220 copies

UNCLASSIFIED

SECURITY CLASSIFICATION OF THIS PAGE

REPORT DOCUMENTATION PAGE

1a. REPORT SECURITY CLASSIFICATION UNCLASSIFIED			1b. RESTRICTIVE MARKINGS		
2a. SECURITY CLASSIFICATION AUTHORITY			3. DISTRIBUTION/AVAILABILITY OF REPORT A Statement; Approved for public release; distribution unlimited.		
2b. DECLASSIFICATION/DOWNGRADING SCHEDULE			4. PERFORMING ORGANIZATION REPORT NUMBER(S) NWC TP 6479		
6a. NAME OF PERFORMING ORGANIZATION Naval Weapons Center			6b. OFFICE SYMBOL (if applicable)		7a. NAME OF MONITORING ORGANIZATION Army Research Office
6c. ADDRESS (City, State, and ZIP Code) China Lake, CA 93555-6001			7b. ADDRESS (City, State, and ZIP Code) Durham, NC 27701		
8a. NAME OF FUNDING/SPONSORING ORGANIZATION		8b. OFFICE SYMBOL (if applicable)		9. PROCUREMENT INSTRUMENT IDENTIFICATION NUMBER DAAG 29-80-K-0052	
8c. ADDRESS (City, State, and ZIP Code)			10. SOURCE OF FUNDING NUMBERS		
			PROGRAM ELEMENT NO.	PROJECT NO.	TASK NO.
			WORK UNIT NO.		
11. TITLE (Include Security Classification) Normal and Oblique Impact of Cylindro-Conical and Cylindrical Projectiles on Metallic Plates (U)					
12. PERSONAL AUTHOR(S) GOLDSMITH, WERNER-Univ. Berkeley, FINNEGAN, STEPHEN A.-NWC					
13a. TYPE OF REPORT Final		13b. TIME COVERED FROM 82 Jun TO 84 Jan		14. DATE OF REPORT (Year, Month, Day) 85 Jun	
15. PAGE COUNT 110					
16. SUPPLEMENTARY NOTATION					
17. COSATI CODES			18. SUBJECT TERMS (Continue on reverse if necessary and identify by block number)		
FIELD	GROUP	SUB-GROUP	Ballistic Impact, Oblique Impact, Perforation, Cylindro-Conical Projectiles, Blunt Cylindrical Projectiles, Steel Targets, and Aluminum Targets.		
19. ABSTRACT (Continue on reverse if necessary and identify by block number)					
<p>(U) An experimental program has been undertaken to study the phenomenon of both normal and oblique impact of cylindro-conical and cylindrical projectiles on metallic plates, a domain where almost no test data is available. Hard-steel strikers of 12.7-mm nominal diameter and either 60-degree conical or blunt tips and blunt soft aluminum cylinders of the same diameter were fired at 2024-0 aluminum targets with thicknesses from 1.78 to 25.4-mm and at both mild steel and medium carbon steel with thicknesses up to 19.05-mm. Initial velocities ranged from about 20 to 1025 m/s, achieved with the aid of a pneumatic cannon at low speeds and a powder gun in the upper velocity range. Initial target obliquity was varied from normal to 50 degrees.</p> <p>(U) The primary results obtained involved the measurement of the velocity drop and change in projectile orientation as the result of passage through the target. Special</p>					
20. DISTRIBUTION/AVAILABILITY OF ABSTRACT <input type="checkbox"/> UNCLASSIFIED/UNLIMITED <input checked="" type="checkbox"/> SAME AS RPT. <input type="checkbox"/> DTIC USERS			21. ABSTRACT SECURITY CLASSIFICATION UNCLASSIFIED		
22a. NAME OF RESPONSIBLE INDIVIDUAL Werner Goldsmith and Stephen A. Finnegan			22b. TELEPHONE (Include Area Code) (619) 939-2206		22c. OFFICE SYMBOL

(20) (Cont.)

attention was devoted to the definition of the ballistic limit for certain projectile-target combinations. The target deformation, consisting of dishing, petals, plugs, and bands separated from the crater, was examined and metallurgical determinations were executed for a selected set of runs. Projectile distortion or fragmentation were also noted and examined. The information obtained should provide an excellent basis for understanding the mechanisms involved in this type of impact and perforation. It will also serve as a reliable source of data for comparison with the predictions from analytical models of the process which do not currently exist, but will most certainly be developed in the future.

CONTENTS

Introduction	7
Apparatus, Instrumentation, and Procedure	7
Metallurgical Analysis	16
Metallurgy of Virgin Materials	17
Results and Discussion	17
Metallurgical Analysis of Target Impact Regions	96
Conclusions	105
References	107

 Figures:

1. Experimental Setup for Low-Velocity Oblique Plate Impact	9
2. Design Sketch of Instrumented Projectile	11
3. Schematic of the Experimental Setup for Force Measurement	13
4. Photographs of High-Velocity Ballistic Arrangement	14
5. Nomenclature Relating to Oblique Impact of Projectiles on Plates	18
6. Photographic Sequence for Run No. C-52. Total time interval: 243.4 μ s	25
7. Photographic Sequence for Run No. C-55. Total time interval: 248.9 μ s	25
8. Photographic Sequence for Run No. C-86. Total time interval: 99.9 μ s	26
9. Photographic Sequence for Run No. C-92. Total time interval: 98.2 μ s	26
10. Photographic Sequence for Run No. C-75. Total time interval: 150.0 μ s	27
11. Photographic Sequence for Run No. C-60. Projectile embedded; total time interval: 244.8 μ s. Gas check detaches from striker back	27
12. Photographic Sequence for Run No. C-73. Total time interval: 125.0 μ s	28
13. Photographic Sequence for Run No. C-106. Total time interval: 245.9 μ s	28

14.	Photographic Sequence for Run No. C-114. Total time interval: 125.0 μ s	29
15.	Photographic Sequence for Run No. C-108. Total time interval: 245.0 μ s	29
16.	Photographic Sequence for Run No. C-109. Total time interval: 244.4 μ s	30
17.	Photographic Sequence for Run No. C-98. Total time interval: 147.2 μ s	30
18.	Photographic Sequence for Run No. C-118. Total time interval: 124.7 μ s	31
19.	Photographic Sequence for Run No. C-115. Total time interval: 149.9 μ s	31
20.	Photographic Sequence for Run No. C-112. Total time interval: 174.6 μ s	32
21.	Photographic Sequence for Run No. C-105. Total time interval: 100.0 μ s	32
22.	Photographic Sequence for Run No. C-110. Total time interval: 174.9 μ s	33
23.	Photographic Sequence for Run No. C-111. Projectile embedded in target, but produced petals and sheared out a plug; total time interval: 173.6 μ s	33
24.	Photographic Sequence for Run No. C-104. Total time interval: 124.7 μ s	34
25.	Photographic Sequence for Run No. C-101. Total time interval: 148.9 μ s	34
26.	Film Sequence at 30-Degree Obliquity for Run No. B-41 from Framing Camera. Rate: 10^4 pictures per second	36
27.	Ballistic Limit as a Function of Initial Obliquity for Various Projectile-Target Combinations	41
28.	Non-Dimensional Velocity Drop as a Function of Initial Obliquity for 3.175-mm-Thick 2024-0 Aluminum Targets Struck by Cylindro-Conical Projectiles	42
29.	Non-Dimensional Velocity Drop as a Function of Initial Obliquity for 6.35-mm-Thick 2024-0 Aluminum Targets Struck by Cylindro-Conical Projectiles	43
30.	Non-Dimensional Velocity Drop as a Function of Initial Obliquity for 3.175-mm-Thick Mild Steel Targets Struck by Cylindro-Conical Projectiles	44
31.	Non-Dimensional Velocity Drop as a Function of Initial Obliquity for 6.35-mm-Thick Mild Steel Targets Struck by Cylindro-Conical Projectiles	45
32.	Non-Dimensional Velocity Drop as a Function of Plate Thickness for 2024-0 Aluminum Targets Struck by Blunt Hard-Steel Projectiles	46
33.	Non-Dimensional Velocity Drop as a Function of Plate Thickness for Various Targets Struck at Normal Incidence by Blunt Soft Aluminum Projectiles	47

34.	Non-Dimensional Velocity Drop as a Function of Plate Thickness for Mild and Medium Carbon Steel Targets Struck by Blunt Hard-Steel Projectiles	48
35.	Final Obliquity as a Function of Initial Obliquity for 3.175-mm-Thick 2024-0 Aluminum Targets Struck by Cylindro-Conical Hard-Steel Projectiles	50
36.	Final Obliquity as a Function of Initial Obliquity for 6.35-mm-Thick 2024-0 Aluminum Targets Struck by Cylindro-Conical Hard-Steel Projectiles	51
37.	Final Obliquity as a Function of Initial Obliquity for 3.175-mm-Thick Mild Steel Targets Struck by Cylindro-Conical Hard-Steel Projectiles	52
38.	Final Obliquity as a Function of Initial Obliquity for 6.35-mm-Thick Mild and Medium Carbon Steel Struck by Cylindro-Conical Hard-Steel Projectiles	53
39.	Angular Change as a Function of Initial Obliquity for 3.175-mm-Thick 2024-0 Aluminum Targets Struck by Cylindro-Conical Hard-Steel Projectiles	54
40.	Angular Change as a Function of Initial Obliquity for 6.35-mm-Thick 2024-0 Aluminum Targets Struck by Cylindro-Conical Hard-Steel Projectiles	55
41.	Angular Change as a Function of Initial Obliquity for 3.175-mm-Thick Mild Steel Targets Struck by Cylindro-Conical Hard-Steel Projectiles	56
42.	Angular Change as a Function of Initial Obliquity for 6.35-mm-Thick Mild and Medium Carbon Steel Targets Struck by Cylindro-Conical Hard-Steel Projectiles	57
43.	Embedment of Cylindro-Conical Steel Projectile in 3.175-mm-Thick Mild Steel Target (Run B-45)	58
44.	Impact of a 39.7 g, 12.7-mm-Diameter Blunt Hard-Steel Projectile on 12.7-mm-Thick 2024-0 Aluminum Plate at 184.2 m/s and Normal Incidence. Projectile perforated and embedded in the target	59
45.	Distal Side of a 3.175-mm-Thick Aluminum Target After Perforation by a Cylindro-Conical Steel Projectile (Run B-35)	60
46.	Distal Side of a 3.175-mm-Thick Aluminum Target After Oblique Perforation by a Cylindro-Conical Steel Projectile (Run B-36)	60
47.	Impact and Distal Sides of a 6.35-mm-Thick Aluminum Target After Oblique Perforation by a Cylindro-Conical Steel Projectile (Run C-9)	61
48.	Impact and Distal Sides of a 6.35-mm-Thick Mild Steel Target Struck Obliquely by a Cylindro-Conical Steel Projectile (Run C-60)	62

49.	Impact and Distal Sides of a 3.175-mm-Thick Aluminum Target After Oblique Perforation by a Cylindro-Conical Steel Projectile (Run C-67)	63
50.	Impact and Distal Sides of a 3.175-mm-Thick Aluminum Target After Oblique Perforation by a Cylindro-Conical Steel Projectile (Run C-22)	64
51.	Distal Side of a 3.175-mm-Thick Mild Steel Target After Oblique Perforation by a Cylindro-Conical Steel Projectile (Run C-8)	65
52.	Distal Side of a 6.35-mm-Thick Steel Plate After Oblique Perforation by a Cylindro-Conical Steel Projectile (Run C-44)	65
53.	Impact and Distal Sides of a 3.175-mm-Thick Mild Steel Plate After Oblique Perforation by a Cylindro-Conical Steel Projectile (Run C-39)	66
54.	Distal Side of a 6.35-mm-Thick Steel Target After Oblique Perforation by a Cylindro-Conical Steel Projectile (Run C-93)	67
55.	Distal Side of a 6.35-mm-Thick Aluminum Target After Normal Perforation by a Blunt Steel Projectile (Run C-49)	67
56.	Distal Side of a 12.7-mm-Thick Aluminum Target After Normal Perforation by a Blunt Steel Projectile (Run C-116)	68
57.	Distal Side of a 6.35-mm-Thick Steel Target Struck by a Blunt Steel Projectile (Run C-118)	68
58.	Distal Side of a 12.7-mm-Thick Mild Steel Target After Normal Perforation by a Blunt Steel Projectile (Run C-115)	69
59.	Distal Side of a 12.7-mm-Thick Aluminum Target After Normal Perforation by a Blunt Aluminum Projectile (Run C-119)	69
60.	Impact and Distal Sides of a 6.35-mm-Thick Steel Target After Normal Perforation by a Blunt Aluminum Projectile (Run C-104)	70
61.	Impact and Distal Sides of a 19.05-mm-Thick Aluminum Target After Normal Impact by a Blunt Aluminum Projectile (Run C-111)	72
62.	Central Contours of Perforated or Deformed Targets . .	73
63.	Distal Side of a 3.175-mm-Thick Aluminum Target for Various Normal Impacts by a Cylindro-Conical Hard Steel Projectile	74
64.	Impact and Distal Sides of a 3.175-mm-Thick Aluminum Target Due to Normal Impact by a Cylindro-Conical Steel Projectile (Run D-8)	76
65.	Distal Side of a 3.175-mm-Thick Aluminum Target Due to Normal Impact by a Hemispherically Tipped Projectile (Run D-30)	77

66.	Distal Side of 1.78-mm-Thick Aluminum Targets After Normal Impact by a Cylindro-Conical Projectile	78
67.	Projectile and Plug Photographs of Runs C-96, C-99, and C-100	81
68.	Projectile, Plug, and Peripheral Target Fragment Photographs of Runs C-102 and C-103	83
69.	Projectile and Plug Photographs for Runs C-104, C-105, and C-106	85
70.	Projectile and Plug Photographs for Runs C-107, C-108, C-112, and C-113	87
71.	Projectile and Plug Photographs for Runs C-115, C-116, C-118, and C-120	89
72.	Projectile and Plug Photographs for Runs C-119 and C-121	91
73.	Force History, Normal Impact of 30.5-g, 12.7-mm-Diameter Hard-Steel Projectile on 3.175-mm-Thick 2024-0 Aluminum Target, Velocity 94.8 m/s. Result was embedment of shank	94
74.	Force History, Normal Impact of a 30.5-g, 12.7-mm-Diameter Hard-Steel Projectile on 3.175-mm-Thick 2024-0 Aluminum Target, Velocity 98.5 m/s. Result was complete perforation	95
75.	Section View of One Side of the Crater in a 6.35-mm Steel Target Perforated by a 12.7-mm Blunt-Ended Steel Cylinder Initially Traveling at 883 m/s. Penetration path shown by arrow. (Run C-48)	98
76.	Micrograph of Concentrated Shear Band Adjacent to Impact Crater in the Target Shown in Figure 75. (400X magnification)	99
77.	Micrograph of Brittle-Appearing Fracture Surface Near the Distal Side of the Perforation Crater Shown in Figure 75. (200X magnification)	99
78.	Section View of the Crater in a 6.35-mm-Thick Steel Target Struck by a 12.7-mm Conical-Tipped Steel Cylinder at 30 Degrees Obliquity and Speed of 325 m/s. Initial penetration path shown by arrow (projectile ricocheted). (Run C-18)	100
79.	Micrograph of Fractured Concentrated Shear Band in Target Shown in Figure 78. (200X magnification) . . .	100
80.	Section View of Crater Formed in a 6.35-mm-Thick Aluminum Target Struck by a 12.7-mm Blunt-Ended Aluminum Cylinder at a Speed of 265 m/s. Penetration path shown by arrow (projectile embedded and was subsequently removed). (Run C-122)	101

81.	Section View of One Side of Crater Formed in 25.4-mm-Thick Aluminum Target by Impact of a 12.7-mm Blunt-Ended Aluminum Cylinder at Speed of 921 m/s. Penetration path shown by arrow (projectile embedded and mushroomed). (Run C-110)	102
82.	Section View of One Side of Crater Formed in 12.7-mm-Thick Aluminum Target Perforated by 12.7-mm-Diameter Blunt-Ended Steel Cylinder Initially Traveling at 594 m/s. Penetration path shown by arrow. (Run C-124)	102
83.	Section View of One Side of the Crater Formed in 6.35-mm-Thick Aluminum Target Perforated by Conical-Tipped Steel Cylinder Initially Traveling at 915 m/s. Penetration path shown by arrow. (Run C-5)	103
84.	Micrograph of Shear Fracture Adjacent to Impact Crater in Target Shown in Figure 82. (100X magnification)	103
85.	Micrograph of Concentrated Shear Band Adjacent to Impact Surface in Mushroomed Aluminum Cylinder Shown in Figure in Figure 81. (100X magnification)	104
86.	Micrograph of Inward Terminus of Concentrated Shear Band Seen in Figure 85. (100X magnification)	104

Tables:

1.	Test Results, Low Velocity Impact of 60-Degree Cylindro-Conical Hard-Steel Projectiles Striking 2024-0 Aluminum Plates. Projectiles 12.5-mm diameter, 29.8-g mass; plates 3.175 mm thick, clamped on 114.3-mm-diameter rings	19
2.	High-Velocity Test Results for Impact of Hard Steel and 2024-0 Aluminum Cylindrical Strikers With Blunt or 60 degree Conical Tips on Metal Plates Clamped on 114.3-mm-Diameter Rings	20
3.	Results of Ballistic Limit Tests on 2024-0 Aluminum at Normal Incidence	40
4.	Selected Plug Data	80

INTRODUCTION

While the normal impact and perforation of thin plates or those of intermediate thickness has been extensively investigated both analytically and experimentally, corresponding studies involving oblique impact have been reported much less frequently (References 1-11). Penetration of targets at obliquity was treated analytically in a general fashion by energy methods (Reference 9) and for cylindro-conical projectiles by momentum considerations (Reference 12). For spherical strikers, an analytical approach has delineated regions of perforation and ricochet and corresponding tests have provided a phase diagram in the plane of initial velocity versus angle of incidence providing for these two eventualities, but involving either intact or shattered projectiles or target regions (References 13 and 14). An experimental program employing 22-caliber lead bullets fired against pure aluminum and aluminum alloy plates at velocities of about 400 m/s at angles of incidence up to about 50 degrees (Reference 15) showed results in reasonable agreement with the predictions of a three-stage phenomenological analysis (Reference 3) when adjusted to take into account a presented target area and thickness for an undeviated projectile path. An extensive experimental investigation of penetration and ricochet of steel spheres on aluminum targets at obliquity has been conducted previously elsewhere (Reference 16).

The objective of the present investigation is to provide an extensive data base of the effect of obliquity on perforation of both aluminum and steel plates. Hard-steel cylinders of 12.7-mm (1/2 inch) nominal diameter, either blunt or with a 60-degree frontal cone, as well as blunt aluminum cylinders of the same diameter were utilized as projectiles. Targets with an effective diameter of 114.3 mm (4 1/2 inches) were clamped in a special holder whose angular position could be adjusted in increments of 5 degrees relative to the direction of firing, although the test sequence was generally spaced at intervals of 10 degrees. It was limited to a maximum obliquity of 50 degrees by safety requirements that demanded avoidance of uncontrolled projectile ricochet posing significant danger to both equipment and personnel.

APPARATUS, INSTRUMENTATION, AND PROCEDURE

Two different ballistic facilities were utilized in the present investigation. Tests involving initial velocities below about 200 m/s were executed at the University of California, Berkeley, utilizing a compressed gas gun with an overall barrel length of 1.40 m. Two slots with centers 152 mm apart, with the initial port opening

1.03 m from the breech, served both to inhibit further projectile acceleration and to measure its muzzle velocity. This was accomplished by the signals generated from the interruption of two light beams focussed on photosensitive elements due to projectile passage, with pulse separation indicated by a time interval meter. A similar arrangement was provided for the measurement of the terminal velocity immediately behind the target, except that the second light ray was replaced by a zigzag path produced by consecutive reflections of the beam between a set of inclined mirrors. This covered a plane perpendicular to the direction of initial projectile travel and served to insure interruption of the laser ray by the projectile even though the striker was turned through an initially unknown angle as the result of perforation for an inclined target. This device was mechanically isolated from the test stand to avoid its actuation by spurious transients. Substantial care was also exercised to insure the appropriate setting of both slope and level of start and stop gates of the recording devices to obtain velocity measurements accurate within 1 percent. This required the simultaneous use of a digital counter and a Biomation digital unit (Gould Corp., Santa Clara, California) an arrangement which could differentiate between the motion of the striker and a preceding plug or petal (Reference 5).

The target holder, which could be clamped rigidly either to a test stand with a horizontal surface or on a 5-degree shimming block, consisted of two parallel circular rings with holes drilled at 10-degree intervals perpendicular to the direction of projectile motion. These holes served to accommodate screws fitting into a plate holder that consisted of two pairs of segments of a plate annulus and permitted clamping the target in place by the tightening of another set of screws. In this manner, the target could be anchored at any desired angle of obliquity in 5-degree increments. A trough filled with Celotex was placed behind the zigzag light grid for projectile recovery, and a witness paper marked initially at the extension of the barrel centerline placed on the front of the catcher tank permitted the determination of the angle of reflection based on the deviation from this mark upon entry and the distance from the paper to the target center. Alternatively, this angle could be ascertained photographically when camera coverage was employed. This occurred in a number of cases where the event was recorded at the rate of 10^4 frames/s by a Photec IV framing camera (Photonic Systems, Sunnyvale, California) with the system illuminated by bulbs supplied with 2400 W of power. The vertical location of the laser net and catcher tank was crucial and required continuous adjustment to allow for the variations in the angle of the projectile deflection for different impact conditions. A diagram of the experimental arrangement for these low-velocity tests is presented in Figure 1.

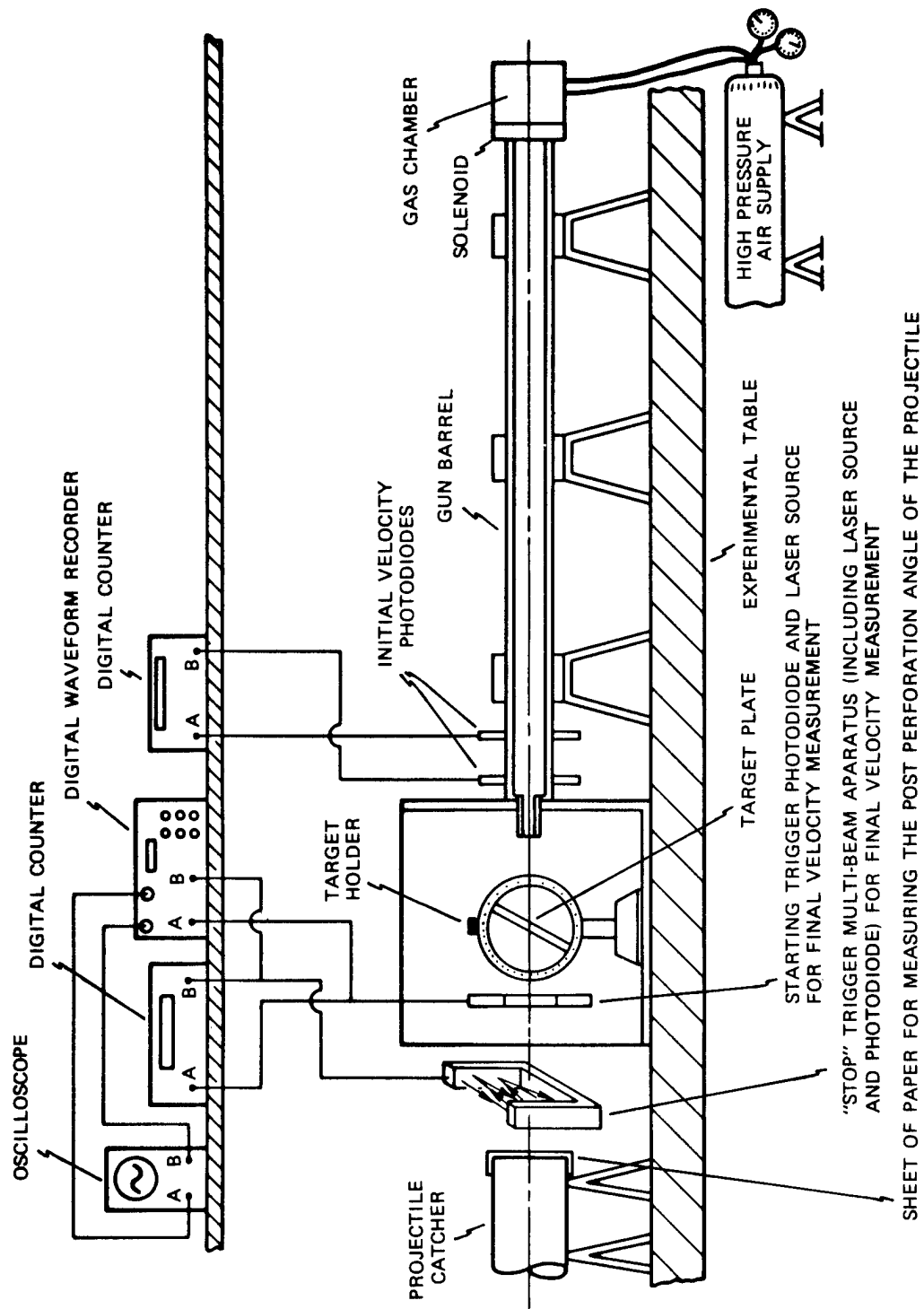
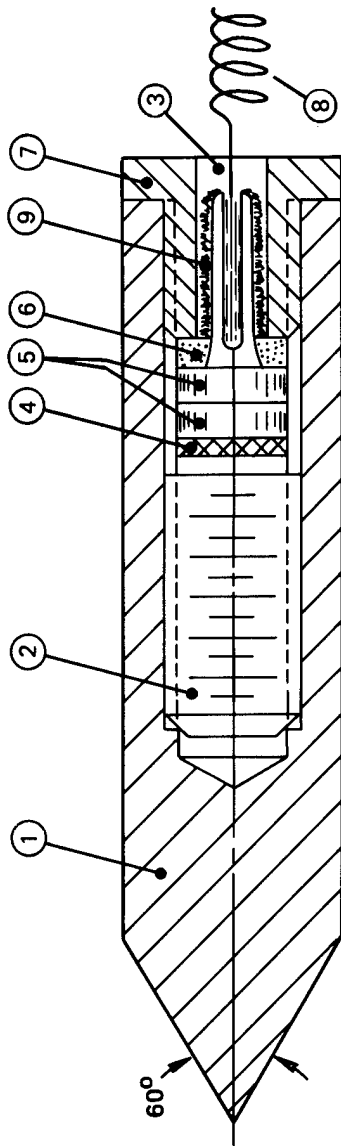


FIGURE 1. Experimental Setup for Low-Velocity Oblique Plate Impact.

The experiments were initiated by emplacement of the projectile in the breech, closure of the firing end, and activation of the solenoid that opened the valve between the gas reservoir and the barrel, thus propelling the striker forward. When the framing camera was not employed, all other measurements were executed automatically. However, when the camera was utilized, triggering of the solenoid was produced by an automatic signal emitted by the camera upon reaching the desired framing rate. This occurred after passage of about 73 m of the 123-m roll of 16-mm black and white film, which had an ASA rating of 400.

In several tests, special conical-headed steel projectiles were fired that incorporated a modified version of the force-measuring device that was subsequently further refined; the latest changes were required to accommodate the oblique impact conditions (References 8 and 5). The unit is sketched in Figure 2. The body consists of a hard-steel cylinder of 12.7-mm diameter with a length of 41.3 mm whose rear surface was tapped along the axis with a 7.9-mm (5/16-inch)-diameter UNC-2B screw thread to a depth of about 26 mm. The front of this unit consisted of a cone of 60-degree total angle. A mating steel screw was inserted tightly into the back of the steel cylinder that still maintained a small air gap at its tip. A 6.35-mm-diameter X-cut quartz crystal, 0.794 mm thick, was fastened with conducting epoxy, Eccobond 56C (Emerson and Cuming, Gardena, California) to the back of the screw shaft, and a 6.35-mm-diameter steel disc, 2 mm thick, was similarly cemented to the back surface of the crystal; the latter represented "an inertial mass." The joints were cured at 75°C for at least 30 minutes to minimize resistivity. The screw was inserted into the hole until the tubular sections were tight. Two copper wires of 0.5-mm-diameter and lengths somewhat greater than that of the gun barrel were soldered to the rear of a second steel disk of similar dimensions and protruded backwards from the projectile. This disk was pressed against the inertial mass by a spring attached to a tail piece suitably threaded for insertion into the rear of the hollow aluminum cylinder. A plastic grommet and polymeric coating insulated the trailing wires from all components of the projectile except their disk terminal. The other ends of the wires, which were initially coiled, were taped to the breech end of the grounded gun and were thus in continuous contact with this device while uncoiling during the motion of the projectile until subsequent to target perforation.

Each composite striker was carefully checked prior to every shot to insure the existence of an open circuit between the impact surface and trailing wires (or ground). The target was electrically insulated; a lead from this plate was attached to the input side of a Nicolet digital recording oscilloscope, which was triggered by the interruption of a laser directly in front of the target, while the



PARTS LIST

1. PROJECTILE BODY
2. ASSEMBLING BOLT
3. PLASTIC GROMMET AND EPOXY
4. PIEZOELECTRIC QUARTZ DISC
5. INERTIAL MASS
6. NYLON DISC - PRELOADED SPRING
7. PROJECTILE TAIL PIECE
8. WIRE - CONTACT SPRING
9. TEFLON TAPE

FIGURE 2. Design Sketch of Instrumented Projectile.

ground side was connected to the gun. The arrangement is shown in Figure 3. The force transducer was calibrated by firing the projectile into a thin aluminum target in such a manner as to perforate, but without exiting (See Reference 8). The impulse recorded by the crystal was equated to the measured initial momentum of the striker to provide a force calibration. As previously, the observed potential difference was found to be linearly proportional to the peak applied force, but substantially different from the value of 3400 N/V, measured and utilized there (Reference 5). Results using the force transducer were obtained for experiments involving normal impact on 3.175-mm-thick 2024-0 aluminum targets struck at and just above the ballistic limit by the 30.5-g projectile.

The ballistic apparatus employed in the gun laboratory of the Naval Weapons Center (NWC), China Lake, is shown in Figure 4. The propulsion unit consisted of a powder gun with a 12.7-mm (1/2-inch)-diameter barrel capable of being evacuated; shots with this device encompassed the initial velocity range from 300-920 m/s (1,000-3,000 ft/s) for projectiles with a mass up to 37 g. The initial projectile velocity was measured from the recorded time elapsed between the interruption of two light beams traversing the barrel a distance of 265.5 mm apart, each centered on a photosensitive unit. This measurement occasionally gave spurious results since products of combustion sometimes maneuvered ahead of the striker in spite of the presence at its rear of a plastic gas check. These particles also prevented the use of a fine copper-wire grid conducting a current whose breakage triggered the photographic recording device. Instead, a break circuit was utilized with the conducting unit consisting of a broad copper grid painted on a paper backing held in a clamp. The individual strips had widths of 1.59 mm (1/16 inch) so that even a shower of burnt particles would not totally sever the circuit, but only a complete tearing of the grid upon bullet arrival. In addition, the gun was fired without evacuation to allow the air within the barrel to decelerate any combustion products that moved ahead of the projectile.

The photographic system consisted of a Beckman Whitley KFC-600 six-cell Kerr camera illuminated by a set of individual PEK Xenon arc lights that could be delayed relative to each other by a maximum interval of 50 μ s with essentially unlimited delay achievable from circuit interruption to the first cell with a Rutherford Model A12 digital time delay generator. The controls were adjusted to provide a minimum of two photographs of the projectile both prior and subsequent to contact with the target. Initial and final velocities measured from these pictures were accurate to within 2-3 percent. The determination of the projectile position in the data reduction from the film was facilitated by a calibration distance of 39.1 mm

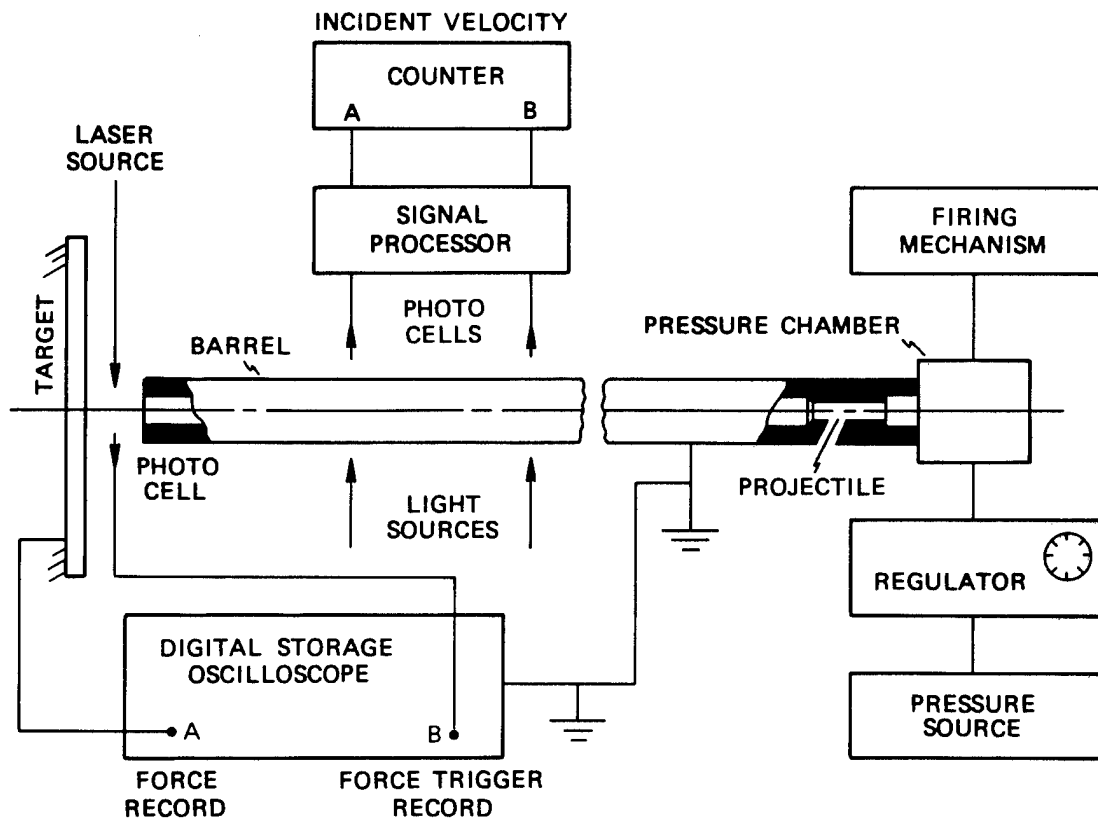


FIGURE 3. Schematic of the Experimental Setup for Force Measurement.

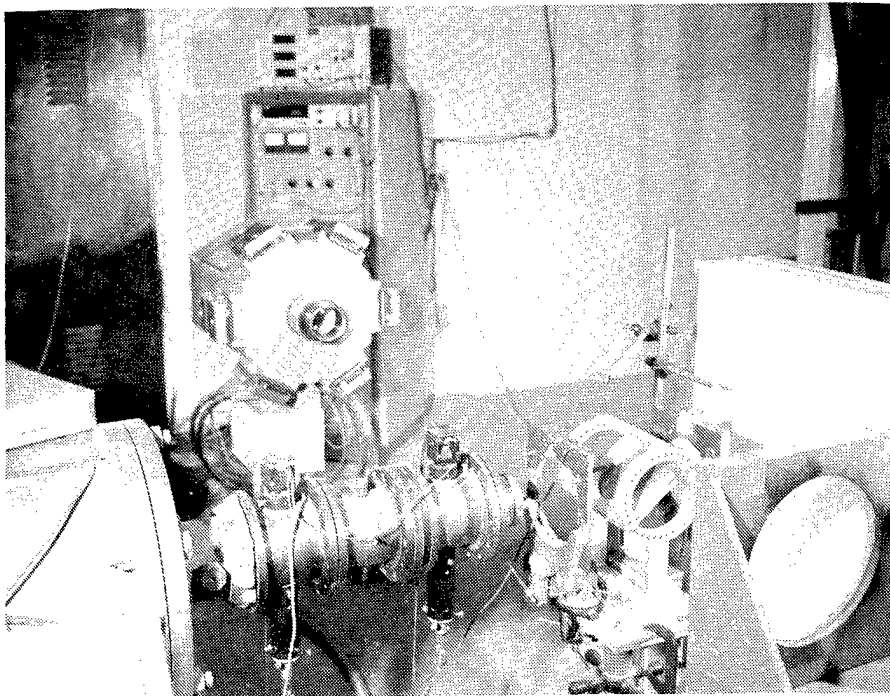
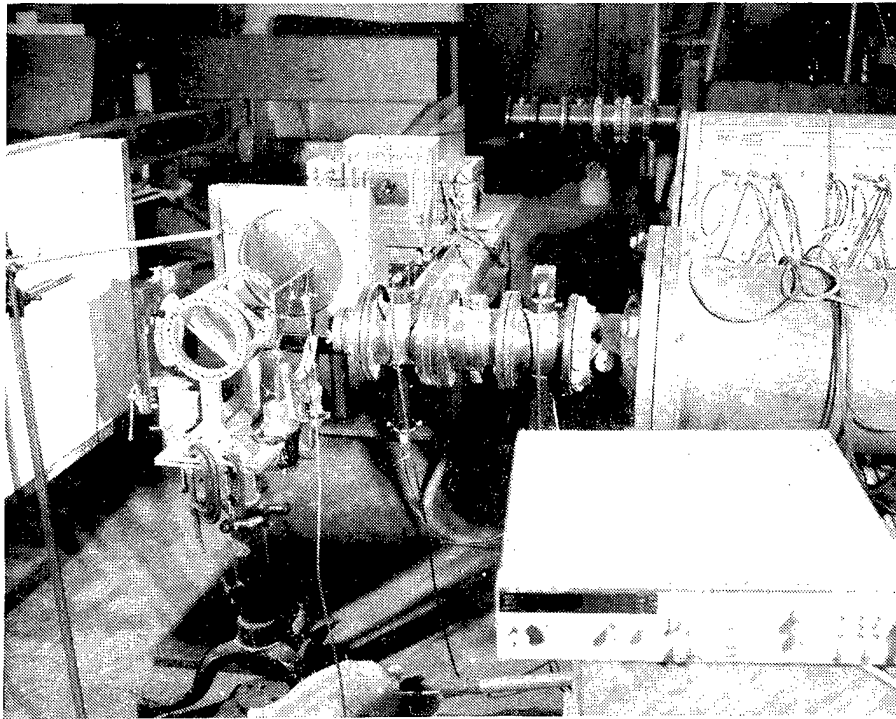


FIGURE 4. Photographs of High-Velocity Ballistic Arrangement.

representing the separation of the tips of a caliper which was suspended near the target center and photographed in each frame.

A witness paper was employed to permit the determination of the deviation of the projectile path after passage through the target. The position of the barrel center was scribed on this paper at the center of the diffracted light pattern generated by a pin source at the muzzle end. A long catcher tank filled with Celotex permitted the recovery of the strikers and of those detached portions of the plate, plug, or petals embedded in this unit. The tank required continuous vertical adjustment and some tilting to conform to the deviation of the projectile path due to plate obliquity. Initial projectile velocity was controlled by the amount of Dupont IMR 4198 powder placed in a standard 50-caliber cartridge that was positioned behind the projectile in the breech. Firing from a remote location was executed after automatic cycling of the electrical system.

The majority of the strikers consisted of drill rod with a surface hardness of 53-60 Rc and a nominal diameter of 12.3 mm, a 60-degree total tip cone angle, and an overall length of 38.1 mm; their average mass was 29.1 g. In addition, some blunt hard-steel and 2024-0 aluminum cylinders of the same diameter were utilized. When any striker was fired by the powder gun, it was either coated with a solid film lubricant (Electrofilm, Inc., MIL-L-23398B) or else coated with copper to reduce gun wear. The copper-coated projectiles were significantly heavier than their bare counterparts, with average masses of 30.8 ± 0.5 g, 36.7 ± 0.5 g, and 14.5 ± 0.7 g for the cylindro-conical and blunt hard steel and the blunt aluminum strikers, respectively.

All test sequences were limited to a maximum obliquity of 50 degrees due to the presence of the 60-degree conical nose shape and the protrusion of the target frame. Larger angles of incidence were certain to produce ricochet, a dangerous condition for both operators and equipment. In spite of substantial precautions taken to avoid such a condition, an occasional ricochet did occur, either from the frontal plate surface or from contact with a support structure after penetration.

Experiments at obliquity were carried out with 3.175- and 6.35-mm-thick 2024-0 aluminum plates annealed to a Brinell hardness of 48 from an initial heat-treated condition corresponding to a Brinell hardness of 130 and on two types of mild steel targets designated as S* and S with a Brinell hardness of 220 and 130, respectively, at initial velocities ranging from about 90 to 900 m/s. Impacts at normal incidence were further executed on 2024-0 aluminum plates of 0.80-, 1.59-, 12.7-, and 15.88-, 19.05-, and 25.4- mm thickness and on 12.7- or 19.05-mm thick mild steel targets. A special series of

runs were also conducted on aluminum plates to ascertain the ballistic limit and the velocity corresponding to the first appearance of miniscule cracks on the distal target side. Runs involving the instrumented projectile were executed at an initial velocity of 146.3 m/s on 3.175-mm-thick 2024-0 aluminum targets with angles of incidence ranging from 0 to 50 degrees. The target plates were fabricated with a 139.7-mm diameter outer ring clamped on a 114.3-mm-diameter ring. The aluminum specimens were cut from a sheet which had been hardened to a T351 condition. The plates were now placed in an oven for 3 hours at 800°F, then exposed to successive reductions in temperature of 50°F for 1 hour each until the level of 500°F was attained beyond which they were oven-cooled to room temperature. The annealing process took approximately 16 hours.

In the vast majority of instances, even at high initial velocities, it was possible to recover both the projectile, sometimes fragmented into several large parts, and cohesive plugs sheared from the targets, and to ascertain their terminal configuration and mass. However, individual petals sheared from the plate could usually not be located.

Contours of numerous targets were measured by means of a profilometer whose sensing element, consisting of a cantilever leaf with a strain gage mounted on it, passed at a constant speed over the deformed surface of the struck targets. Vertical deflection was calibrated by gage blocks. A number of the targets were also sectioned and subjected to metallurgical examination.

METALLURGICAL ANALYSIS

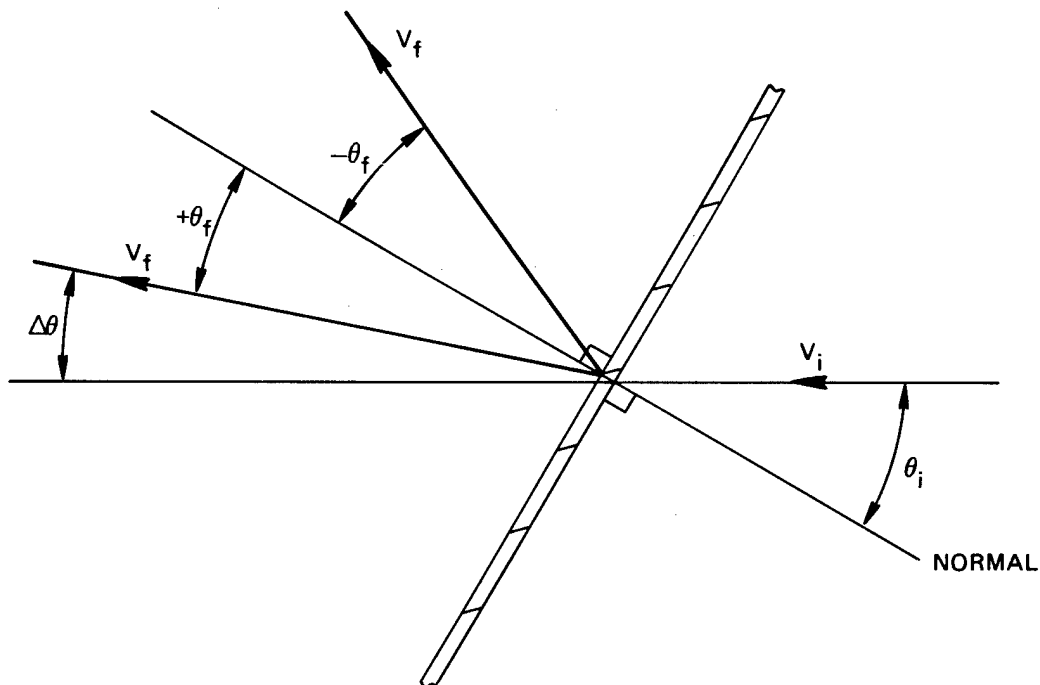
A metallurgical analysis of virgin and post-impacted target plates was also undertaken to characterize the materials as completely as possible prior to testing and to study the penetration and failure processes more intimately. The inspection of virgin materials consisted of a visual scan of the surfaces to identify forming (primarily rolling) patterns, hardness tests, a microstructural examination of small wedges of material taken from the outer edges, and, for one material, a spectrographic analysis to identify the alloy. Post-impact studies consisted of a visual inspection of fracture surfaces using a microscope with a magnification less than 50 and a microstructural analysis of target sections taken from the impact areas. Specimens for microstructural examination were cut from the targets using a high-speed, water-cooled, cut-off wheel to minimize damage. They were then mounted in Bakelite, ground flat, and finally polished and etched for viewing with an optical microscope.

METALLURGY OF VIRGIN MATERIALS

In all cases, the visual inspection of target surfaces revealed a distinctive rolling pattern characteristic of plate or sheet material. All aluminum targets exhibited approximately the same hardness levels of 87-95 Rockwell H, consistent with values for a fully annealed 2024-0 alloy. The hardness of the 3.175-mm-thick steel measured approximately 60 Rockwell B (107 Brinell), a value representative of a hot-rolled or annealed low-carbon steel. This was verified by an inspection of the microstructure, which consisted almost entirely of fine, equiaxed ferrite grains indicative of a very low (less than 0.1%) amount of carbon. However, two hardness values, 74 or 96 Rockwell B (135 or 216 Brinell), were measured on different 6.35-mm-thick steel plates, which were also differentiated by the coloring of the oxide coating on the surfaces (bluish-black for the steel with the lower hardness and reddish-brown for the other). The microstructure of the former consisted of fine, equiaxed ferrite grains plus lamellar pearlite colonies consistent with about 0.2% carbon level, while the microstructure of the second consisted almost entirely of lamellar pearlite colonies with small amounts of ferrite along the prior austenite grain boundaries. A spectrographic analysis of the second material identified it as either SAE 1053, 1060, 1064, or 1065 composition carbon steel.

RESULTS AND DISCUSSION

The nomenclature adopted in defining the geometric and kinematic parameters involved in the oblique impact tests is indicated in Figure 5. The results for the low-velocity shots utilizing uninstrumented projectiles are presented in Table 1, while the data from the powder gun experiments, which for the current series of tests involved only solid strikers, are summarized in Table 2. Runs C-1 to C-49 were executed with bullets sprayed with the solid film lubricant, while the strikers employed in Runs C-50 to C-121 were coated with copper. Whenever feasible, both initial and terminal velocities in the powder gun experiments were determined from the camera data. A representative series of photographs featuring the 60-degree cylindro-conical hard-steel projectile is shown in Figures 6-12. A sequence of impacts with the blunt striker of the same material is portrayed in Figures 13-20, and a set of pictures showing the results of collisions with a blunt 2024-0 aluminum cylinder are exhibited in Figures 21-25. The photographs presented are limited to impacts at normal incidence and 40-degree obliquity for reasons of space; both mild steel and soft aluminum targets were involved with initial velocities ranging from 300 to 920 m/s.



V_i = INITIAL VELOCITY

V_f = FINAL VELOCITY (AFTER PENETRATION)

θ_i = INITIAL OBLIQUITY ANGLE

θ_f = FINAL OBLIQUITY ANGLE

$\Delta\theta = \theta_i - \theta_f$ = THE RELATIVE ANGLE BETWEEN THE FINAL
AND THE INITIAL OBLIQUITY ANGLE

FIGURE 5. Nomenclature Relating to Oblique Impact of Projectiles on Plates.

TABLE 1. Test Results, Low-Velocity Impact of 60-Degree Cylindro-Conical Hard-Steel Projectiles Striking 2024-0 Aluminum Plates. Projectiles 12.5-mm diameter, 29.8-g mass; plates 3.175-mm-thick; clamped on 114.3 mm-diameter rings.

Run No.	V_i , m/s	V_f , m/s	$\frac{\Delta V}{V_i}$, %	θ_i , deg	θ_f , deg	$\Delta\theta$, deg	Remarks
B-1†	155.7	152.4	2.1	0	0	0	
B-2‡	150.0	141.3	5.7	10	---	---	
B-3	157.7	127.4	19.2	0	0	0	
B-4	154.1	123.8	19.7	0	0	0	
B-5	150.6	120.7	19.8	10	+3	7	
B-6	151.0	120.2	20.4	20	+6.7	13.3	
B-7	151.2	105.2	30.4	30	+8.0	22	
B-8	133.1	99.2	34.4	30	+9.3	20.7	
B-9	151.0	115.6	23.4	20	+7.3	12.7	
B-10	151.2	387.7	21.8	10	+2.2	7.8	
B-11	122.0	77.5	36.5	10	-4.7	14.7	
B-12	91.6	0	100.0	10	---	---	At or below ballistic limit
B-13	107.5	49.5	54.0	10	-7.4	17.4	
B-14	98.9	48.3	51.2	10	+3.7	6.3	
B-15	122.3	53.9	55.9	20	-6.9	26.9	
B-16	121.8	53.9	55.8	20	-8.0	28.0	
B-17	99.5	0	100.0	20	---	---	At or below ballistic limit
B-18	103.7	~0	~100.0	30	---	---	Slightly above the ballistic limit
B-19	102.8	---	---	30	---	---	Ricochet
B-20	156.6	128.3	18.1	0	0	0	
B-21	157.2	127.2	19.1	0	0	0	
B-22	126.1	83.6	33.7	0	0	0	
B-23	96.5	0	100.0	0	---	---	Ballistic limit
B-24	102.9	36.2	64.8	0	0	0	
B-25	121.4	---	---	30	-21.5	51.5	
B-26	155.3	69.1	55.5	40	~0	40.0	
B-27	159.0	128.0	19.5	0	0	0	
B-28	159.8	---	---	20	13.6	6.4	The zigzag laser beam did not trigger the Biomation unit
B-29	156.4	79.0	49.5	10	2.9	7.1	
B-30	160.1	121.3	24.2	10	11.3	-1.3	
B-31	161.3	117.7	27.0	30	15.0	15.0	
B-32	159.8	103.0	35.5	40	17.8	22.2	
B-33	160.0	105.8	33.9	40	16.1	23.9	
B-34	160.4	82.6	48.5	50	37.0	13.0	
B-35	~122.0	---	---	40	2.9	37.1	Projectile missed the multibeam array
B-36	~122.0	52.7	56.8	30	2.1	27.9	
B-37	122.6	---	---	30	-5.0	35.0	Projectile missed the multibeam array
B-38	123.2	67.4	45.3	20	13.0	7.0	
B-39	162.8	120.7	25.8	20	9.9	10.1	
B-40	160.1	118.0	26.2	20	9.1	10.9	
B-41	160.1	100.6	37.1	30	7.0	23.0	
B-42	123.2	50.3	59.1	30	2.3	27.7	Movie film taken
B-43*	160.7	---	---	0	---	---	Hole started but projectile did not go through
B-44*	170.7	---	---	0	---	---	Hole started but projectile did not go through
B-45*	182.9	---	---	0	---	---	Projectile embedded in target with a hole \approx projectile diameter

*3.175 mm thick mild steel targets for Runs B-43, B-44, and B-45.
 †1.58 mm thick 2024-0 aluminum plate.

TABLE 2. High-Velocity Test Results for Impact of Hard Steel and
2024-0 Aluminum Cylindrical Strikers with Blunt or 60-Degree Conical
Tips on Metal Plates Clamped on 114.3-mm-Diameter Rings.

Run No.	Target		Projectile			Velocities					Remarks	
	Material	Thickness, mm	Material	Nose	Mass, g	V _i , m/s	V _f , m/s	$\frac{\Delta V}{V_i}$, %	θ_i , deg	θ_f , deg		$\Delta\theta$, deg
C-1	A	3.175	HS	C	29.0	293.9	245.1	16.6	0	0	0	$\Delta V/V_i$ determined from photo only. Actual impact velocity less than indicated.
C-2	A	3.175	HS	C	29.0	382.6	247.9	35.2	0	0	0	
C-3	A	3.175	HS	C	29.1	229.5	161.9#	~29.4	0	0	0	
C-4	A	3.175	HS	C	29.1	960.4	718.1#	~25.2	0	0	0	
C-5	A	6.35	HS	C	---	~915.0	839.0	8.2	0	0	0	
C-6	S	3.175	HS	C	29.0	337.2	191.8	43.1	0	0	0	Impact velocity assumed from powder-load.
C-7	A	3.175	HS	C	29.0	333.8	282.3	15.5	10	8.5	1.5	
C-8	S	3.175	HS	C	29.2	362.8	248.1	31.6	10	8	2	
C-9	A	6.35	HS	C	29.2	326.2	235.5#	27.8	10	8	2	
C-10	S*	6.35	HS	C	29.0	334.5	60.4#	81.9	10	---	---	
C-11	A	3.175	HS	C	29.3	337.8	286.7#	15.1	20	19	1	Ricochet.
C-12	S	3.175	HS	C	29.2	332.3	252.5#	~24	20	16	4	
C-13	A	6.35	HS	C	29.3	332.0	256.1#	22.8	20	18	2	
C-14	S*	6.35	HS	C	29.1	332.3	81.3#	75.5	20	-1.5	21.5	
C-15	A	3.175	HS	C	29.1	356.4	255.7#	28.2	30	26	4	
C-16	S	3.175	HS	C	29.3	336.9	254.9#	24.3	30	24	6	Ricochet.
C-17	A	6.35	HS	C	29.3	326.2	267.0	18.1	30	26	4	
C-18	S*	6.35	HS	C	29.2	~325.0	---	---	30	---	---	
C-19	A	3.175	HS	C	29.2	332.3	313.1	5.8	40	36	4	
C-20	S	3.175	HS	C	29.2	334.5	232.0	30.6	40	29	11	
C-21	A	6.35	HS	C	29.2	328.4	217.1	33.9	40	47	-7	
C-22	A	3.175	HS	C	29.1	301.8	176.8#	41.4	50	48	2	
C-23	S	3.175	HS	C	29.1	332.3	209.5#	36.9	50	48.5	1.5	
C-24	A	6.35	HS	C	29.2	332.3	244.2	26.5	50	42.5	7.5	
C-25	A	3.175	HS	B	34.9	360.4	300.3	16.6	50	46.0	4.0	
C-26	S	3.175	HS	B	34.7	342.4	218.3	36.2	50	42.0	8.0	
C-27	A	6.35	HS	B	~34.8	330.8	240.9	27.2	50	44.0	6.0	
C-28	A	3.175	HS	B	~34.8	331.7	327.7	1.2	30	26.5	3.5	
C-29	A	6.35	HS	B	~34.8	328.4	284.6	13.3	0	0	0	
C-30	S	3.175	HS	B	~34.8	341.2	278.8	18.3	0	0	0	
C-31	S*	6.35	HS	B	34.8	326.2	196.1	39.9	0	0	0	Very close to ballistic limit. At $\theta_i = 30$ deg ricochet occurred.
C-32	S*	6.35	HS	C	29.2	339.0	65.8	80.6	26	24.0	2.0	
C-33	A	3.175	HS	C	28.9	604.9	576.8	4.6	0	0	0	
C-34	S	3.175	HS	C	29.3	607.0	503.4	18.1	0	0	0	
C-35	A	6.35	HS	C	29.1	605.2	523.5	13.5	0	0	0	

See footnote at end of table.

TABLE 2. (Contd.)

Run No.	Target		Projectile		Velocities						Remarks	
	Material	Thickness, mm	Material	Nose	Mass, g	V _i , m/s	V _f , m/s	$\frac{\Delta V}{V_i}$, %	θ_i , deg	θ_f , deg		$\Delta\theta$, deg
C-36	S*	6.35	HS	C	29.1	597.6	564.9#	5.5	0	0	0	Ricochet.
C-37	A	3.175	HS	C	29.2	596.0	568.9#	4.5	30	32.0	-2.0	
C-38	A	3.175	HS	C	29.0	605.8	591.0#	2.4	50	46.5	3.5	
C-39	S	3.175	HS	C	29.0	593.0	553.9#	6.5	30	31.0	-1.0	
C-40	S	3.175	HS	C	29.0	594.3	521.3#	12.3	50	44.5	5.5	
C-41	A	6.35	HS	C	29.0	605.2	558.6#	7.7	30	31.0	-1.0	
C-42	A	6.35	HS	C	29.0	601.5	537.6#	10.4	50	47.0	3.0	
C-43	S*	6.35	HS	C	29.0	603.7	399.2#	34.0	30	---	---	
C-44	S*	6.35	HS	C	29.3	604.5	511.6	15.4	50	---	---	
C-45	S*	6.35	HS	C	29.4	482.1	---	---	50	---	---	
C-46	S*	6.35	HS	B	34.8	556.4	275.3#	50.2	50	---	---	No camera trigger. $\Delta V/V_i$ determined from photos only. Camera pretriggered. Major diameter of hole 25 mm.
C-47	S*	6.35	HS	B	34.7	328.7	183.2	44.2	26	25.0	1.0	
C-48	S*	6.35	HS	B	34.7	882.6	690.5#	21.8	0	0	0	
C-49	A	6.35	HS	B	34.6	882.6	700.9	20.5	0	0	0	
C-50	A	3.175	HS	C	30.3	334.4	304.9	8.8	30	26.0	4.0	
C-51	A	3.175	HS	C	30.4	323.8	---	---	40	32.9	7.1	$\Delta V/V_i$ determined from photos only. Major diameter of hole 20 mm.
C-52	A	3.175	HS	C	30.8	300.6	281.4	6.4	40	39.0	1.0	
C-53	A	3.175	HS	C	30.6	326.8	---	---	50	45.4	4.6	
C-54	A	3.175	HS	C	30.8	315.5	266.4	15.6	50	43.0	7.0	
C-55	S	3.175	HS	C	30.9	317.7	223.5	30.0	40	27.0	13.0	
C-56	A	6.35	HS	C	30.5	312.3	306.1	2.0	30	25.0	5.0	Embedded. Embedded. No velocity decrease within experimental error.
C-57	A	6.35	HS	C	30.4	304.9	240.8	21.0	40	36.0	4.0	
C-58	S	6.35	HS	C	30.7	325.6	230.5#	29.2	10	15.0	-5.0	
C-59	S	6.35	HS	C	30.7	316.5	0	100.0	10	---	---	
C-60	S	6.35	HS	C	31.2	320.1	0	100.0	0	---	---	
C-61	A	3.175	HS	C	30.7	587.8	567.0	3.5	0	0	0	No velocity decrease within experimental error.
C-62	A	3.175	HS	C	30.7	600.6	600.6	0	10	10.0	0	
C-63	S	3.175	HS	C	30.9	586.9	497.0#	15.5	40	42.0	-2.0	
C-64	S	3.175	HS	C	30.5	612.8	579.3	5.5	20	23.0	-3.0	Major diameter of hole 19.8 mm.
C-65	S	3.175	HS	C	30.6	609.8	557.9#	8.5	10	8.0	2.0	
C-66	S	3.175	HS	C	30.9	608.5	582.3	4.3	0	0	0	
C-67	A	3.175	HS	C	30.4	605.2	530.4	12.3	40	40.0	0	No velocity decrease within experimental error.
C-68	A	3.175	HS	C	31.0	608.2	608.2	0	20	20.0	0	

See footnote at end of table.

TABLE 2. (Contd.)

Run No.	Target		Projectile			Velocities						Remarks
	Material	Thickness, mm	Material	Nose	Mass, g	V_i , m/s	V_f , m/s	$\frac{\Delta V}{V_i}$, %	θ_i , deg	θ_f , deg	$\Delta\theta$, deg	
C-69	S	6.35	HS	C	31.3	607.0	490.9	19.1	0	0	0	No velocity decrease within experimental error. Major diameter of hole 21.3 mm. $\Delta V/V_i = 20\%$ based on V_i and V_f from pictures. Major diameter of hole 24.1 mm. $\Delta V/V_i$ determined from photos only.
C-70	S	6.35	HS	C	30.5	622.0	503.0	19.1	10	8.0	2.0	
C-71	A	6.35	HS	C	30.6	614.3	588.4#	4.2	10	8.0	2.0	
C-72	A	6.35	HS	C	30.5	612.8	<612.8#	~4.0	20	17.0	3.0	
C-73	A	6.35	HS	C	30.9	613.4	<609.8#	0.6	40	39.0	1.0	No velocity decrease within experimental error. Major diameter of hole 21.3 mm. $\Delta V/V_i = 20\%$ based on V_i and V_f from pictures. Major diameter of hole 24.1 mm. $\Delta V/V_i$ determined from photos only.
C-74	S	6.35	HS	C	30.6	640.3	512.2	20.0	20	20.0	0	
C-75	S	6.35	HS	C	30.9	644.0	515.2	20.0	40	36.0	4.0	
C-76	A	6.35	HS	C	30.9	960.4	960.4	0	0	0	0	
C-77	A	6.35	HS	C	30.6	931.4	931.4	0	10	8.0	2.0	No velocity decrease within experimental error. Major diameter of hole 17.8 mm.
C-78	A	6.35	HS	C	30.6	923.8	897.0	2.9	20	21.0	-1.0	
C-79	A	6.35	HS	C	30.5	930.0	930.0	~0	30	35.0	-5.0	
C-80	A	6.35	HS	C	31.1	920.7	749.7	18.6	40	40.0	0	
C-81	A	6.35	HS	C	30.4	936.0	~915.0	~2.3	50	50.0	0	No velocity decrease within experimental error. Major diameter of hole 27.9 mm.
C-82	S	3.175	HS	C	30.5	930.0	875.6	5.8	0	0	0	
C-83	S	3.175	HS	C	30.6	926.8	926.8	0	10	10.0	0	
C-84	S	3.175	HS	C	31.0	965.9	879.0	9.0	20	21.0	-1.0	
C-85	S	3.175	HS	C	30.9	923.8	922.6	0.13	30	30.0	0	No velocity decrease within experimental error. $\Delta V/V_i$ determined from photos only.
C-86	S	3.175	HS	C	30.3	904.0	875.3	3.2	40	41.5	-1.5	
C-87	S	3.175	HS	C	30.9	~918.3	918.3	0	50	53.0	-3.0	
C-88	S	6.35	HS	C	30.6	933.9	812.5	13.0	0	0	0	
C-89	S*	6.35	HS	C	30.6	1025.6	873.8	14.8	10	9.5	0.5	$\Delta V/V_i$ determined from photos only. $\Delta V/V_i$ determined from photos only. $\Delta V/V_i$ determined from photos only. $\Delta V/V_i$ determined from photos only.
C-90	S*	6.35	HS	C	30.4	940.0	902.4	4.0	20	18.0	2.0	
C-91	S*	6.35	HS	C	30.8	932.5	857.9	8.0	30	28.0	2.0	
C-92	S*	6.35	HS	C	30.9	932.9	784.4	16.0	40	----	---	

See footnote at end of table.

TABLE 2. (Contd.)

Run No.	Target		Projectile		Velocities							Remarks
	Material	Thickness, mm	Material	Nose	Mass, g	V_i , m/s	V_f , m/s	$\frac{\Delta V}{V_i}$, %	θ_i , deg	θ_f , deg	$\Delta\theta$, deg	
C-93	S*	6.35	HS	C	30.6	999.2	749.4	25.0	50	---	---	Major diameter of hole 29 mm. Striker broke during penetration. Fastest particle beyond plate travels in initial direction of striker. $\Delta V/V_i$ determined from photos only.
C-94	A	6.35	HS	B	36.6	690.5	566.2	18.0	0	0	0	$\Delta V/V_i$ determined from photos only.
C-95	A	6.35	HS	B	37.1	610.5	~380.0	5.0	0	0	0	$\Delta V/V_i$ determined from photos only.
C-96	S*	6.35	HS	B	36.2	606.7	481.1	20.7	0	0	0	$\Delta V/V_i$ determined from photos only.
C-97	A	6.35	HS	B	36.3	707.1	544.5	23.0	40	41.0	-1.0	$\Delta V/V_i$ determined from photos only.
C-98	S*	6.35	HS	B	36.2	514.5	334.4	35.0	40	31.5	8.5	$\Delta V/V_i$ determined from photos only.
C-99	A	6.35	A	B	14.7	661.6	442.7	33.0	0	0	0	$\Delta V/V_i$ determined from photos only.
C-100	S	3.175	A	B	14.0	652.4	411.0	37.0	0	0	0	$\Delta V/V_i$ determined from photos only.
C-101	S*	6.35	A	B	14.0	801.8	146.6	81.7	0	0	0	Projectile collapsed and mushroomed. Target and projectile fragments widely scattered. $\Delta V/V_i$ determined from photos only.
C-102	A	12.7	A	B	14.3	678.0	372.9	45.0	0	0	0	$\Delta V/V_i$ determined from photos only.
C-103	A	12.7	A	B	13.8	1013.7	691.1	31.8	0	0	0	
C-104	S*	6.35	A	B	14.6	923.8	288.4	68.7	0	0	0	
C-105	A	6.35	A	B	14.2	917.7	658.2	28.3	0	0	0	
C-106	A	12.7	HS	B	36.3	324.2	291.8	10.0	0	0	0	Adjoining 12.7 and 3.175 mm aluminum plates.
C-107	A	15.88	HS	B	36.6	325.9	221.6	32.0	0	0	0	
C-108	A	19.05	HS	B	36.3	338.1	127.1	62.4	0	0	0	No penetration. Projectile embedded.
C-109	A	25.4	HS	B	36.5	332.9	0	100.0	0	---	---	No penetration.
C-110	A	25.4	A	B	14.2	920.7	0	100.0	0	---	---	No penetration.
C-111	A	19.05	A	B	14.1	929.0	0	100.0	0	---	---	Projectile embedded. Plug separated and petals were formed.
C-112	S	19.05	HS	B	36.3	~884.1	314.3	64.4	0	0	0	Final velocity that of cloud.
C-113	A	19.05	HS	B	36.5	670.6	449.3	33.0	0	0	0	Curved plug.
C-114	A	19.05	HS	B	36.2	887.2	738.4	17.0	0	0	0	Projectile broke into 3 pieces.
C-115	S	12.7	HS	B	36.5	884.1	554.9	37.0	0	0	0	Projectile shattered.

See footnote at end of table.

TABLE 2. (Contd.)

Run No.	Target		Projectile			Velocities						Remarks
	Material	Thickness, mm	Material	Nose	Mass, g	V _i , m/s	V _f , m/s	$\frac{\Delta V}{V_i}$, %	θ_i , deg	θ_f , deg	$\Delta\theta$, deg	
C-116	A	12.7	HS	B	36.4	880.1	814.6	7.6	0	0	0	Projectile broke into many pieces.
C-117	A	6.35	HS	B	36.3	985.2	~807.9	18.0	0	0	0	
C-118	S*	6.35	HS	B	36.3	861.3	689.0	20.0	0	0	0	
C-119	A	12.7	A	B	15.2	813.2	300.9	63.0	0	0	0	Major diameter of hole 33 mm. Embedded. Initial velocity from gun data.
C-120	A	12.7	HS	B	36.2	600.0	445.4	25.8	40	38.0	2.0	
C-121	S	12.7	HS	B	36.5	750.0	75.0	90.0	40	24.0	16.0	
C-122	A	6.35	A	B	14.2	275.0	0	100.0	0	---	---	Initial velocity from gun data. Initial velocity from gun data. Initial velocity from gun data.
C-123	A	6.35	A	B	14.2	368.0	226.8	38.4	0	0	0	
C-124	A	12.7	HS	B	36.5	594.0	547.0	7.9	0	0	0	
C-125	A	12.7	HS	B	36.6	593.3	559.0	5.8	0	0	0	

A = 2024-O Aluminum

S = Mild Steel

S* = Medium carbon steel

HS = Hardened drill rod

C = 60 degree conical tip

B = Blunt tip

= Final velocity determined from photographs before complete exit of projectile from target.

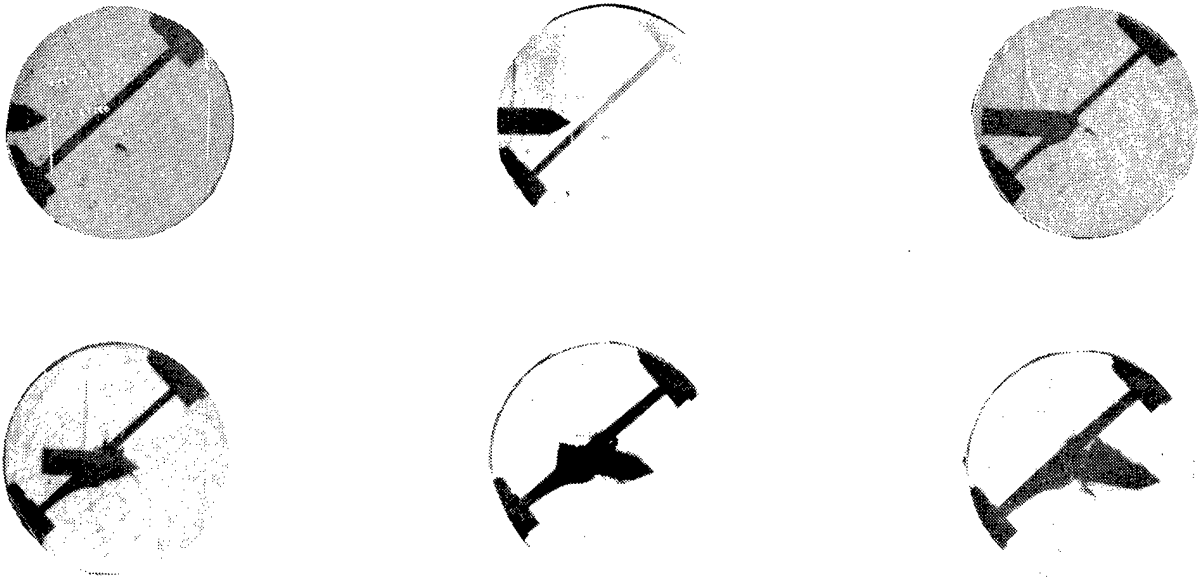


FIGURE 6. Photographic Sequence for Run No. C-52.
Total time interval: 243.4 μ s.

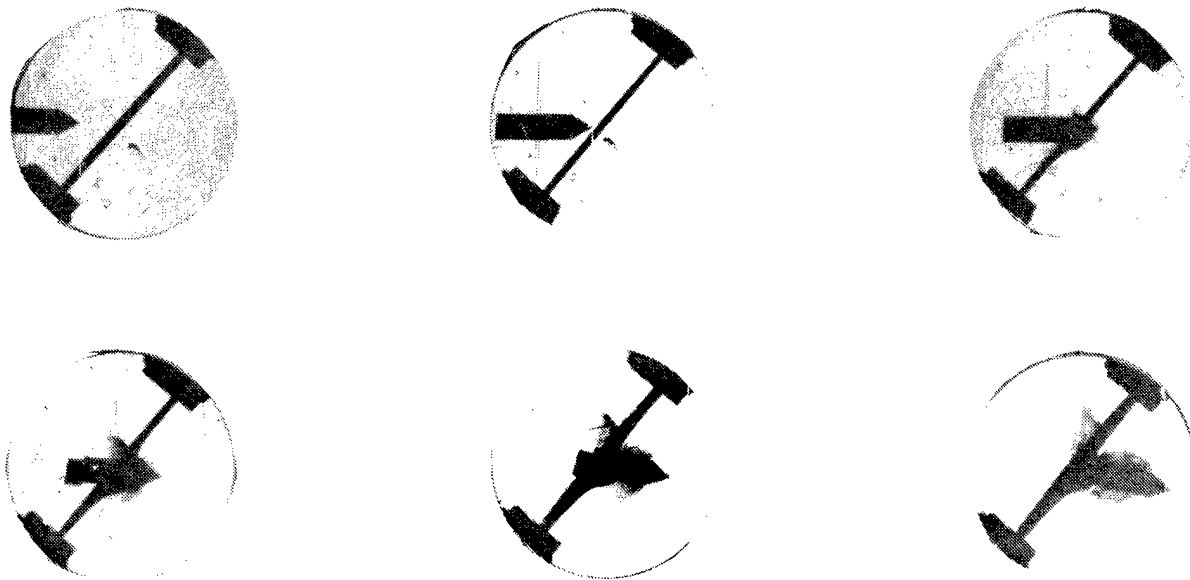


FIGURE 7. Photographic Sequence for Run No. C-55.
Total time interval: 248.9 μ s.

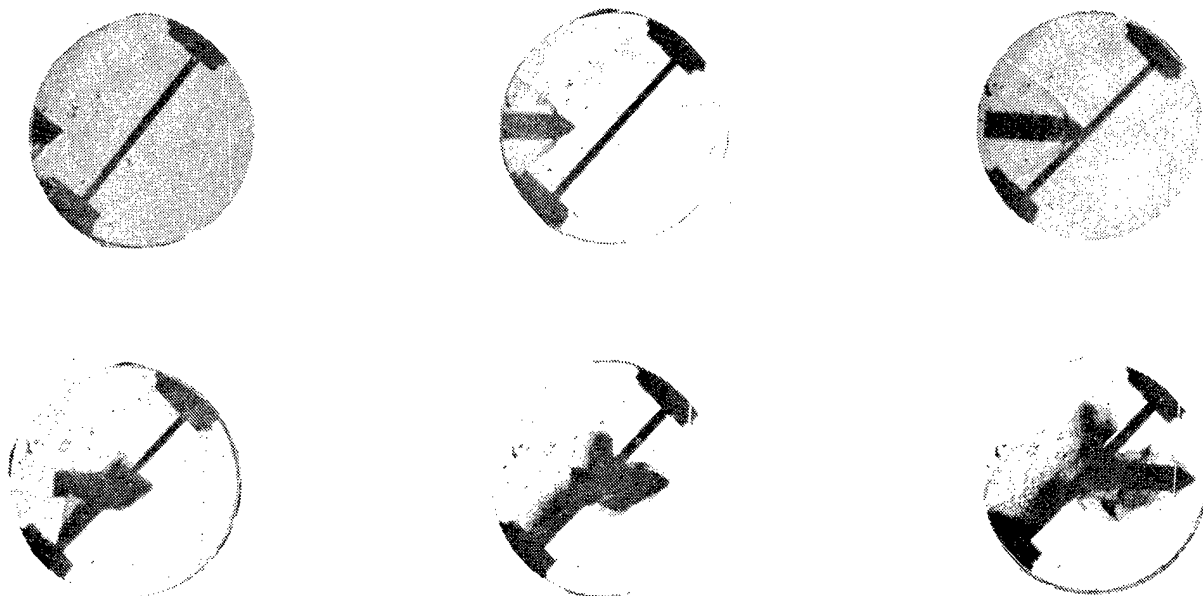


FIGURE 8. Photographic Sequence for Run No. C-86.
Total time interval: 99.9 μ s.

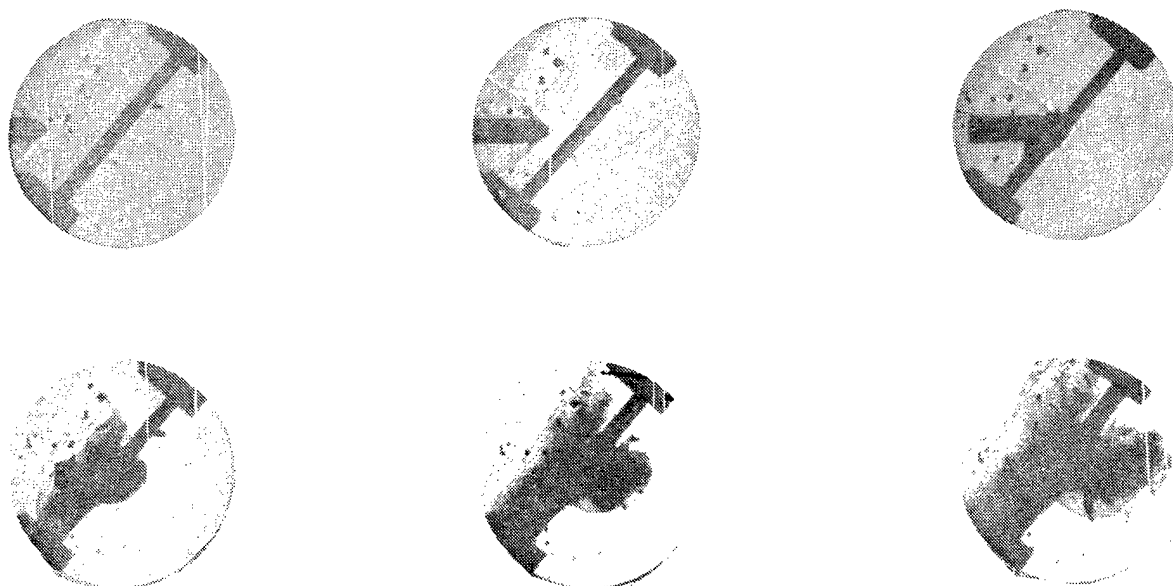


FIGURE 9. Photographic Sequence for Run No. C-92.
Total time interval: 98.2 μ s.

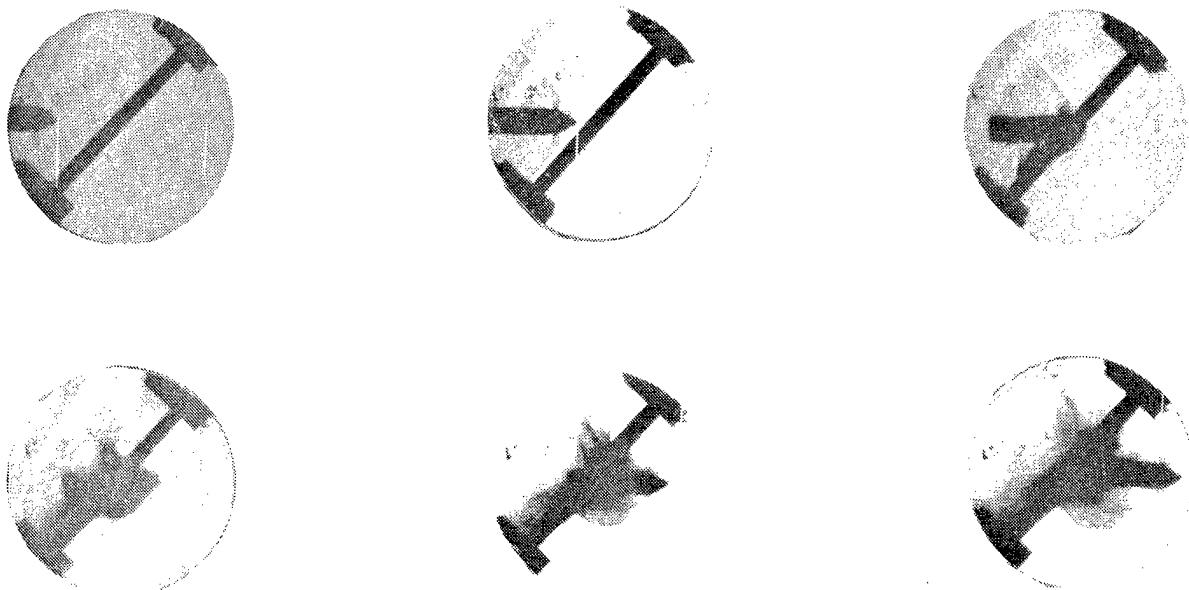


FIGURE 10. Photographic Sequence for Run No. C-75.
Total time interval: 150.0 μ s.

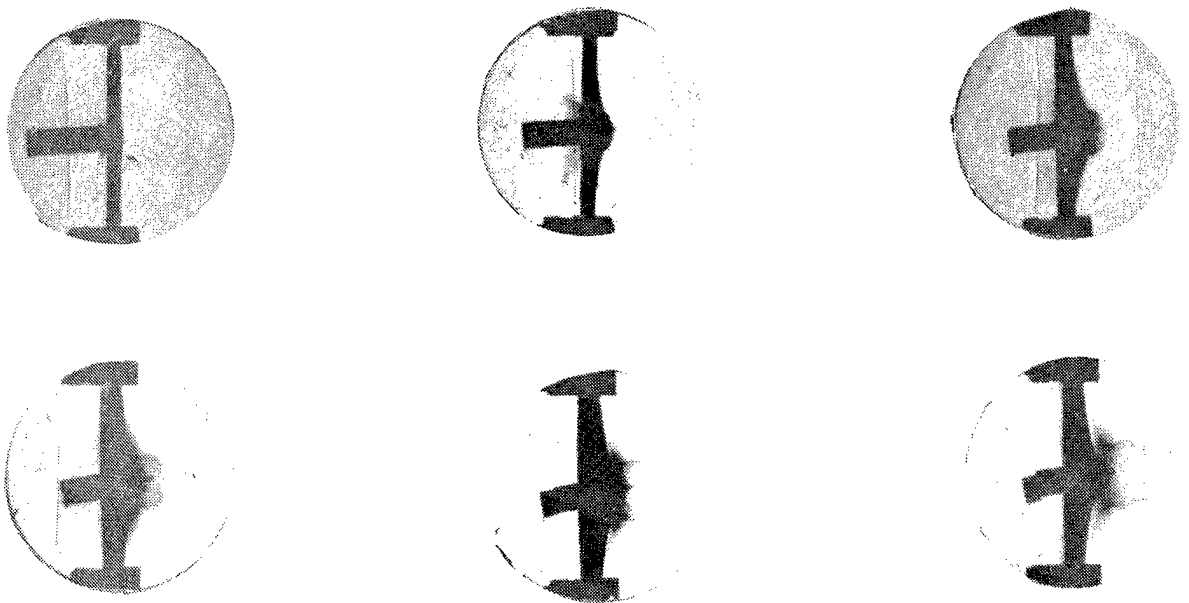


FIGURE 11. Photographic Sequence for Run No. C-60.
Projectile embedded; total time interval:
244.8 μ s. Gas check detaches from striker
back.

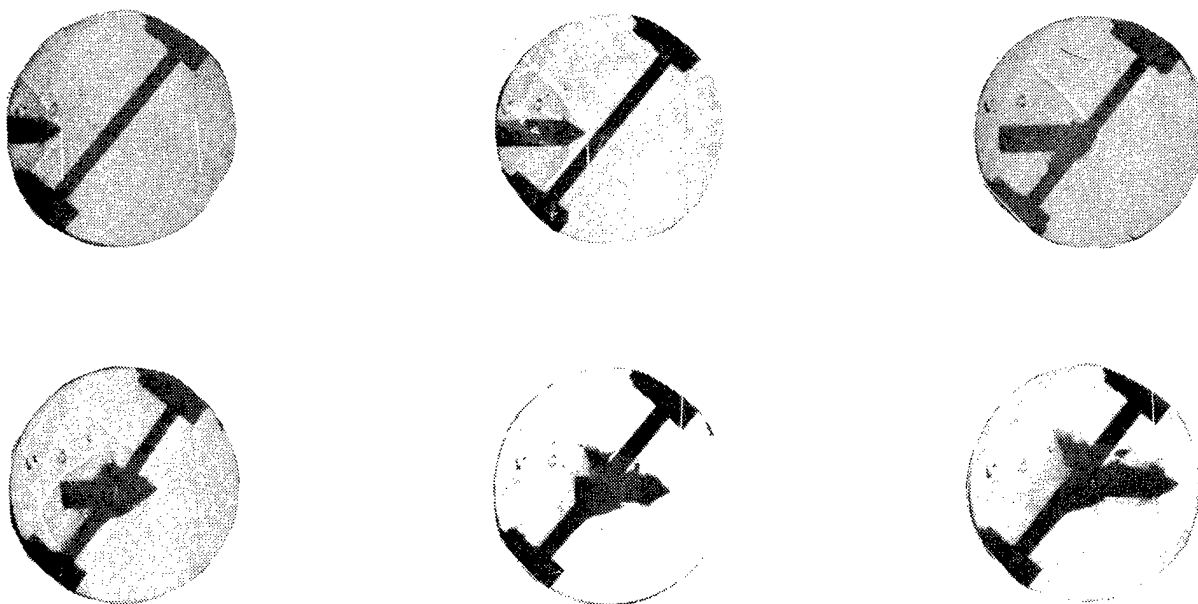


FIGURE 12. Photographic Sequence for Run No. C-73.
Total time interval: 125.0 μ s.

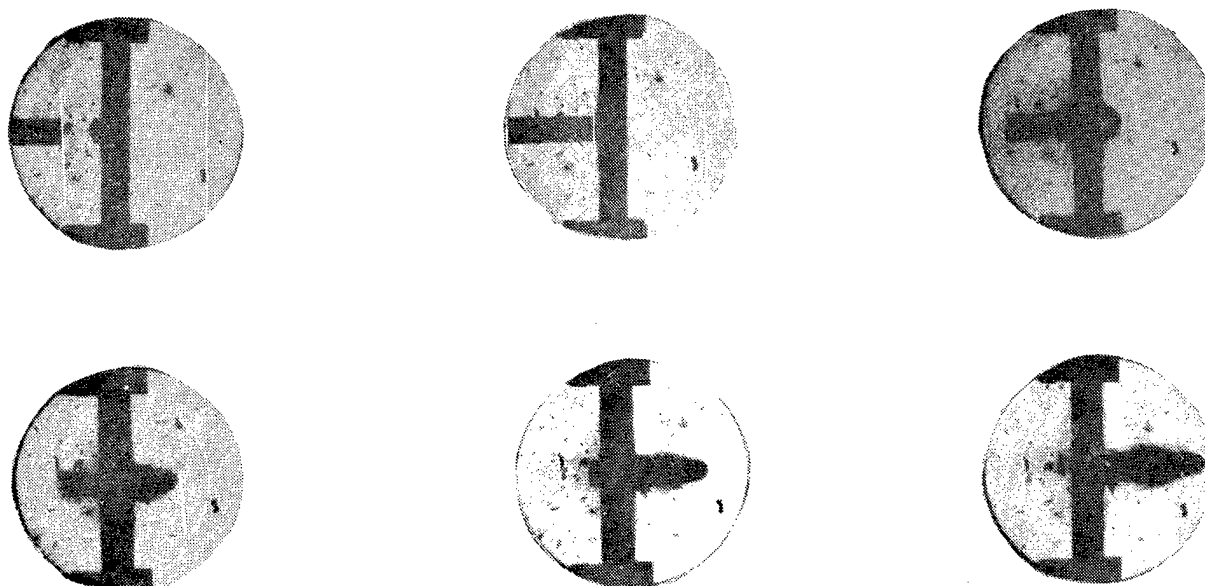


FIGURE 13. Photographic Sequence for Run No. C-106.
Total time interval: 245.9 μ s.

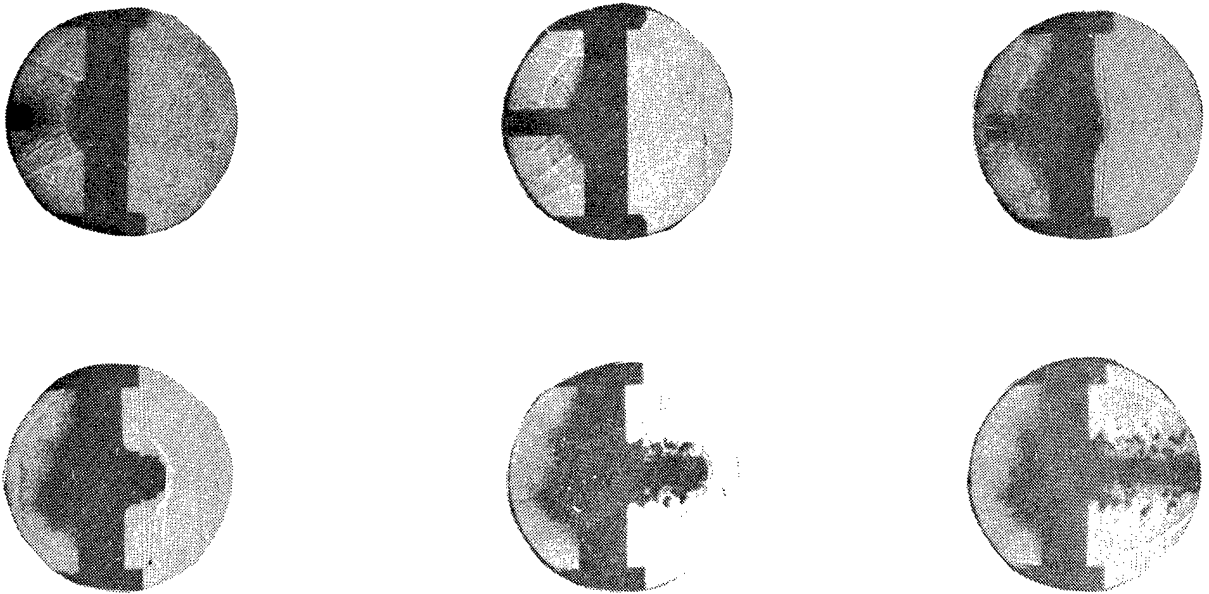


FIGURE 14. Photographic Sequence for Run No. C-114.
Total time interval: 125.0 μ s.

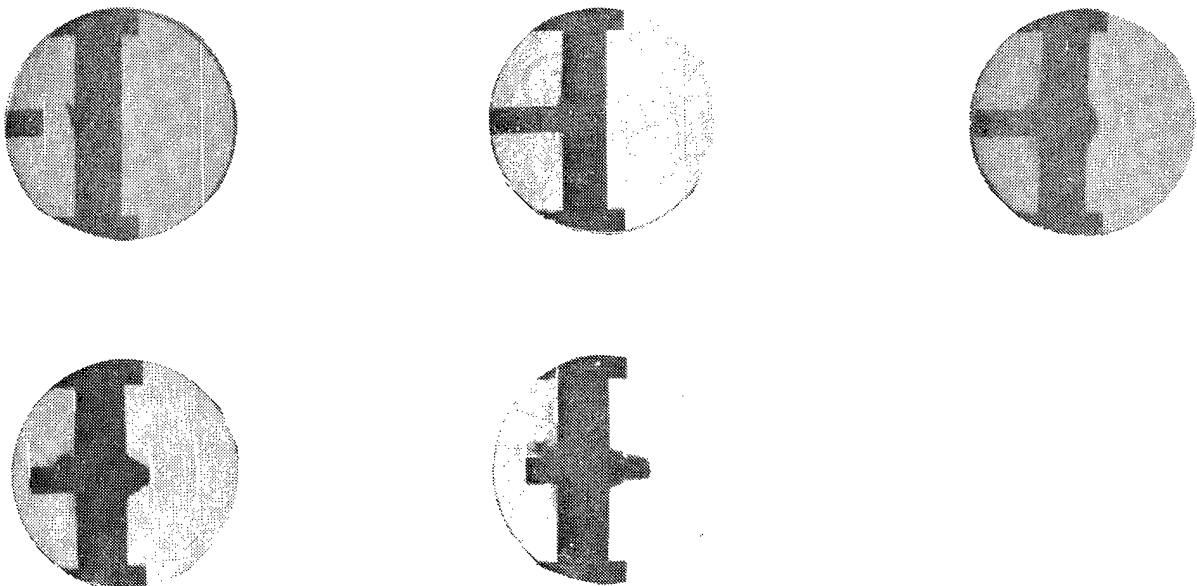


FIGURE 15. Photographic Sequence for Run No. C-108.
Total time interval: 245.0 μ s.

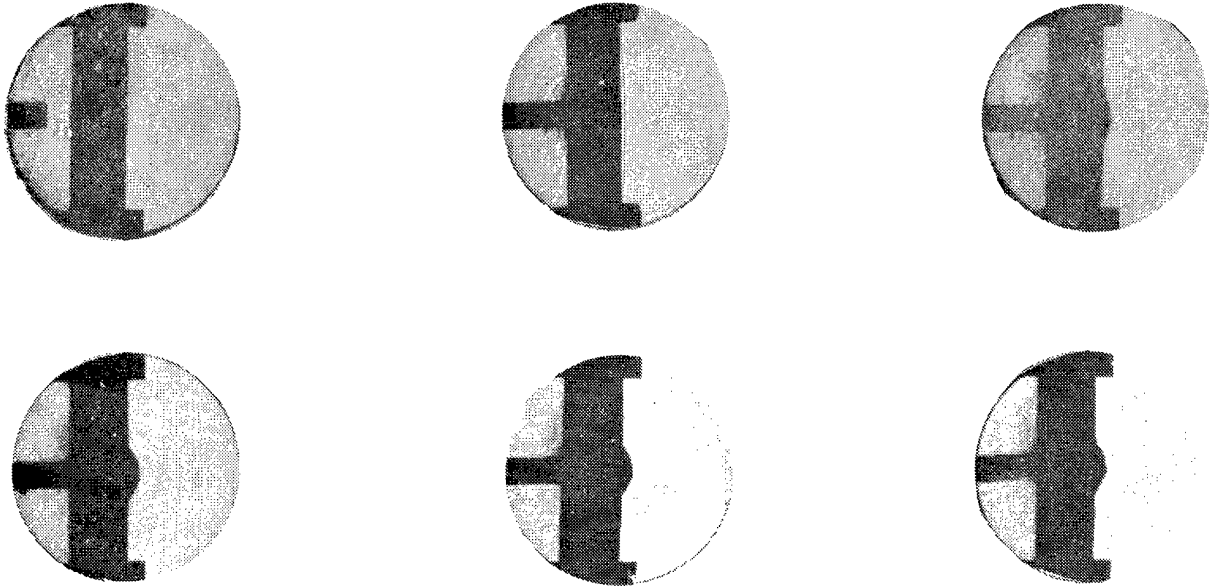


FIGURE 16. Photographic Sequence for Run No. C-109.
Total time interval: 244.4 μ s.

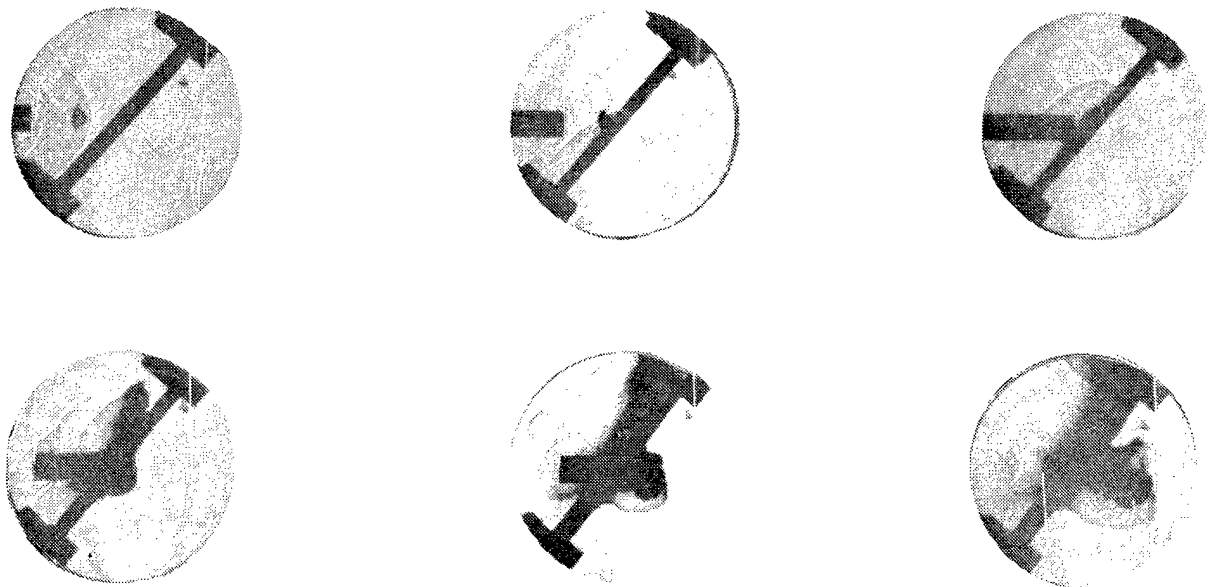


FIGURE 17. Photographic Sequence for Run No. C-98.
Total time interval: 147.2 μ s.

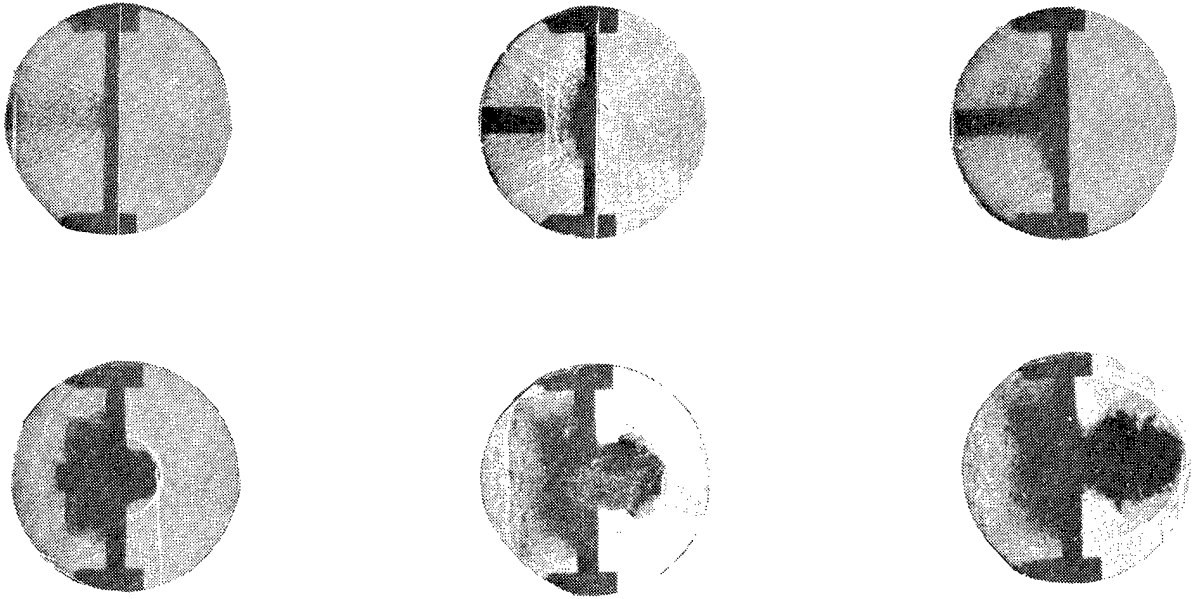


FIGURE 18. Photographic Sequence for Run No. C-118.
Total time interval: 124.7 μ s.

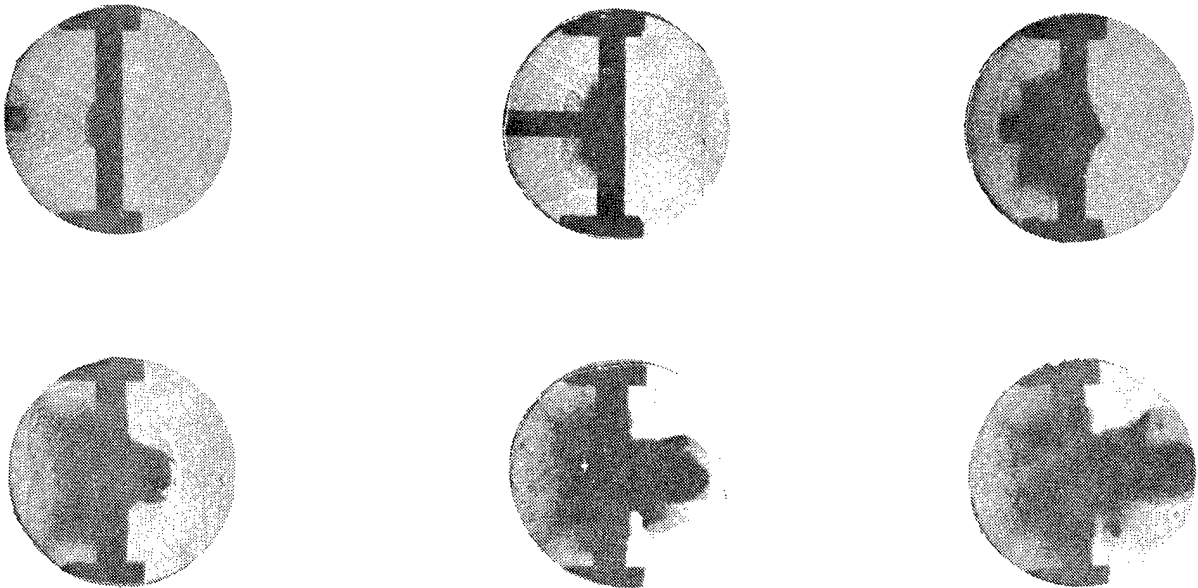


FIGURE 19. Photographic Sequence for Run No. C-115.
Total time interval: 149.9 μ s.

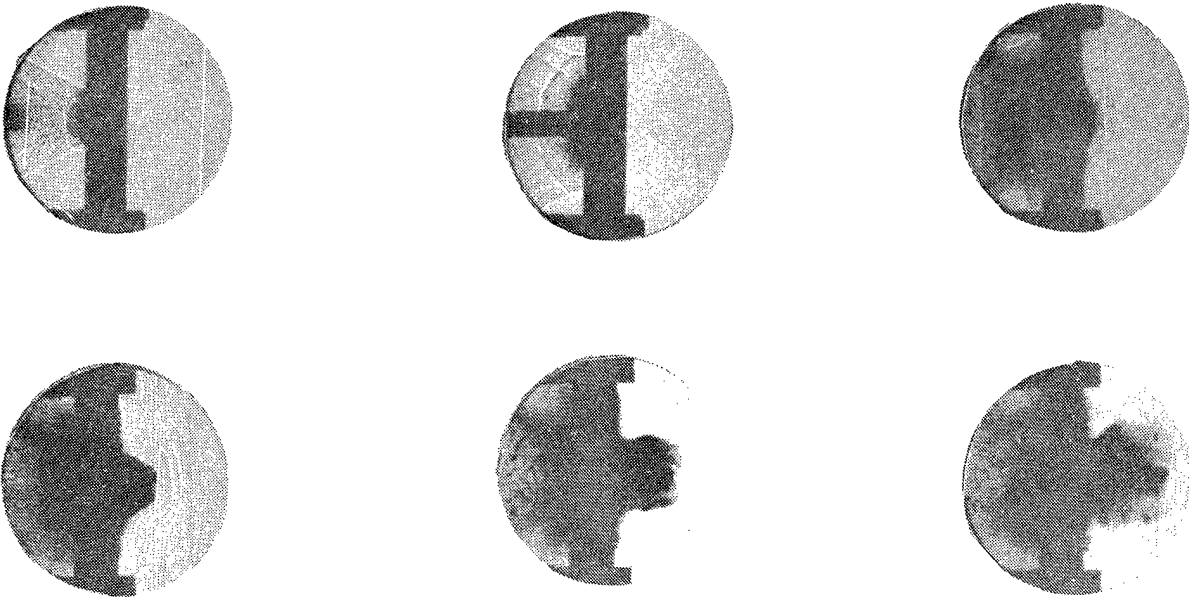


FIGURE 20. Photographic Sequence for Run No. C-112.
Total time interval: 174.6 μ s.

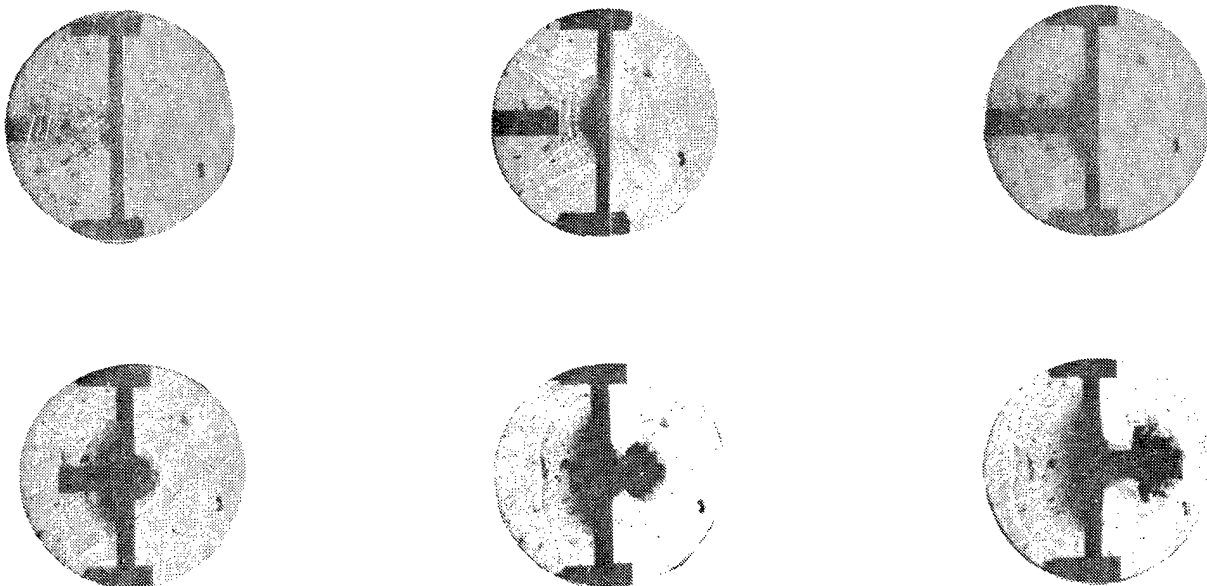


FIGURE 21. Photographic Sequence for Run No. C-105.
Total time interval: 100.0 μ s.

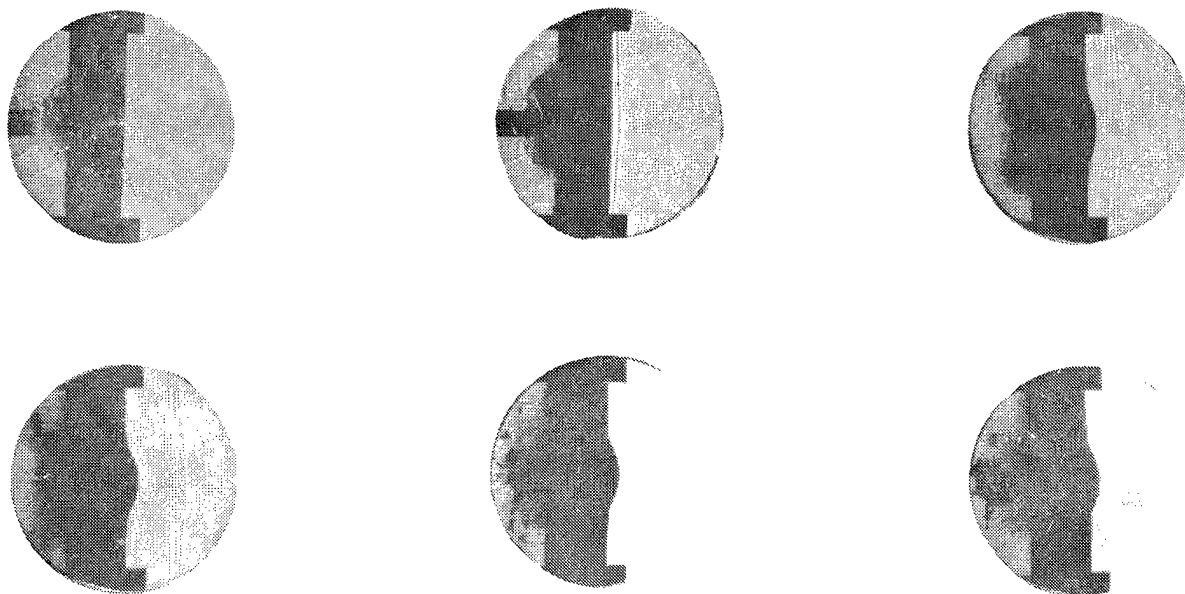


FIGURE 22. Photographic Sequence for Run No. C-110.
Total time interval: 174.9 μ s.

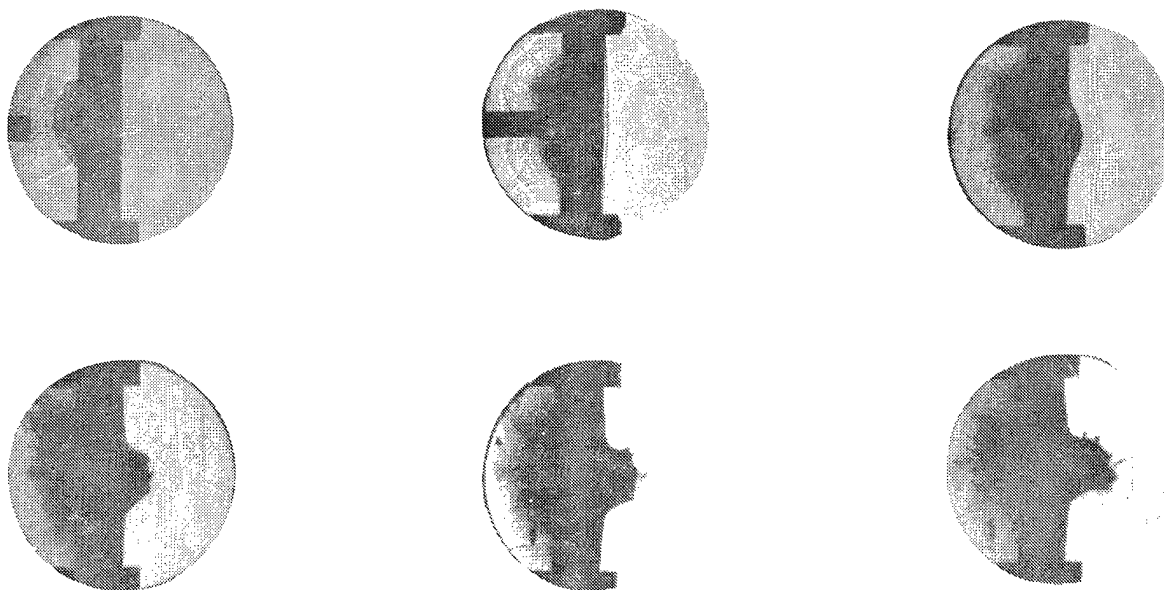


FIGURE 23. Photographic Sequence for Run No. C-111.
Projectile embedded in target, but produced
petals and sheared out a plug; total time
interval: 173.6 μ s.

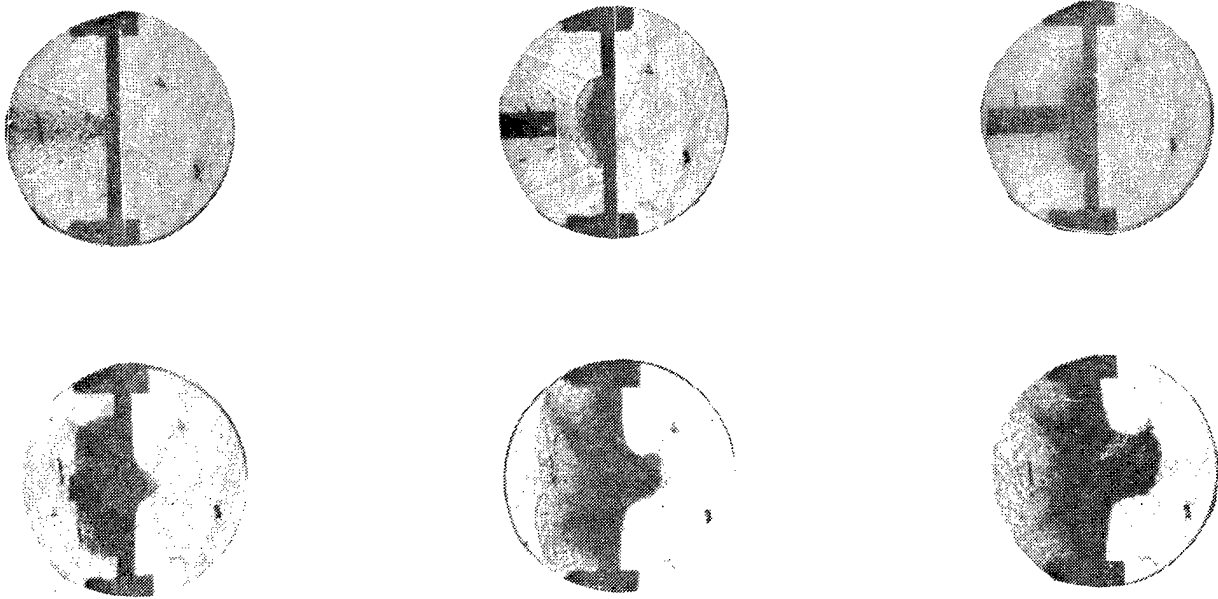


FIGURE 24. Photographic Sequence for Run No. C-104.
Total time interval: 124.7 μ s.

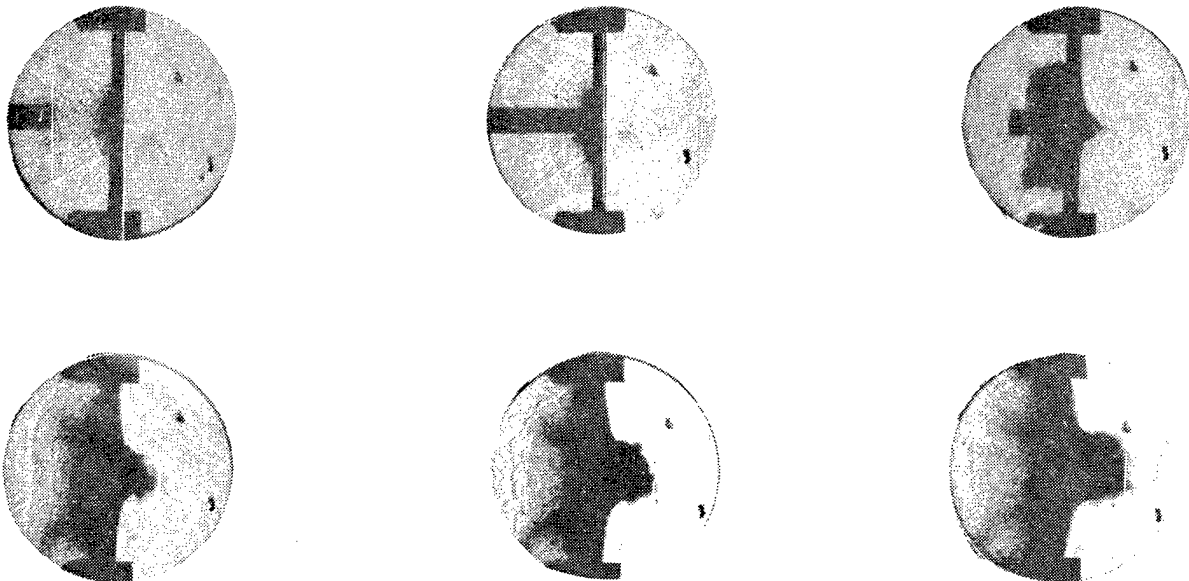


FIGURE 25. Photographic Sequence for Run No. C-101.
Total time interval: 148.9 μ s.

The impact shown in Figure 14 resulted in a dual fracture of the striker, while those presented in Figures 18 and 19 shattered the projectile completely. The normal collision portrayed in Figure 11 resulted in perforation of the plate by the projectile tip with embedment of the body, while that shown in Figure 16 embedded the striker in the plate with no piercing of the distal side, but only the appearance of a bulge in the form of a portion of a sphere with a circular boundary in the original target plane.

All aluminum cylinders were deformed by the targets in varying degrees, depending on impact velocity, plate material, and target thickness. Principal deformation modes included mushrooming and significant shortening, with occasional severe fracturing. Figure 23 portrays the interesting situation where the projectile did not pass through the fairly thick aluminum target, yet produced both a separated plug and petals. Figure 25, on the other hand, depicts the case where the projectile both mushroomed and collapsed, shattering small pieces of target and striker over a wide region beyond the initial plate position.

Figures 6-25 permit a comparison of the effect of target material, target thickness, and initial velocity at the two angles of incidence chosen. In general, more debris is produced at higher velocities on the same target, as evident from the pairing of Figures 7 and 8, 13 and 14, and 17 and 18, respectively. An examination of Figures 6 and 7 shows that more debris is produced in the case of the steel target as compared to aluminum, and that the former exhibits a cloud only on the distal side. In general, this situation also prevails with increase in thickness of a given material at a specified impact velocity, as documented by the pairing of Figures 8 and 9, and 13, 15, and 18, respectively, unless the projectile was embedded (Figure 16). These conclusions apply regardless of the angle of obliquity. As expected, the nose shape produced significant differences in the penetration phenomenon only near the ballistic limit. Figures 11 and 23 are considered to represent conditions just below the ballistic limit, while the events portrayed in Figures 24 and 25 are believed to correspond to initial velocities barely above this limit.

Figure 26 presents a sequence of photographs for the impact at 30-degree obliquity of a hard-steel cylindro-conical projectile on a 3.175-mm-thick 2024-0 aluminum target at an initial velocity of 160 m/s taken at a rate of 10^4 frames/s. This set, which clearly shows the change in projectile direction toward the plate normal, is not suitable for analysis beyond initial and terminal velocity measurement, since the nose, whose length is 12.7 mm and which is responsible for the change of projectile direction, passes through the target in less than one frame. In order to provide a

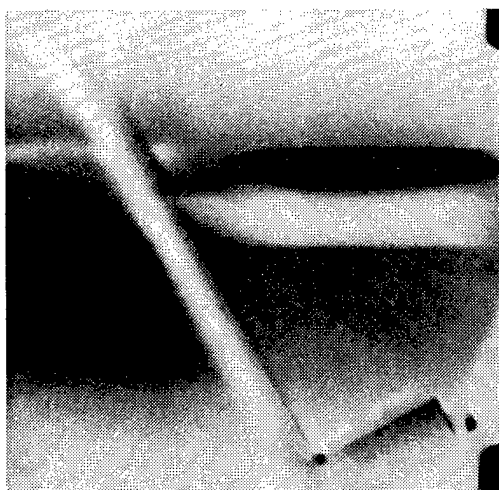
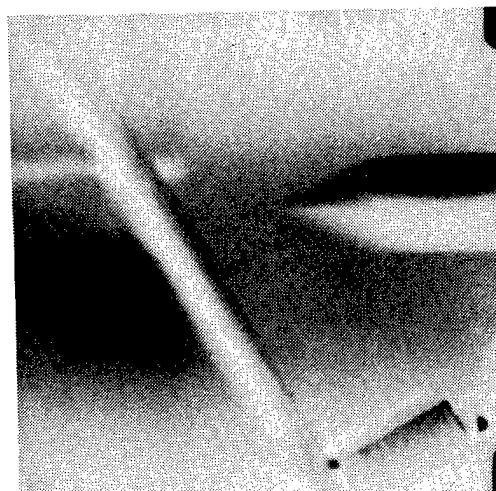
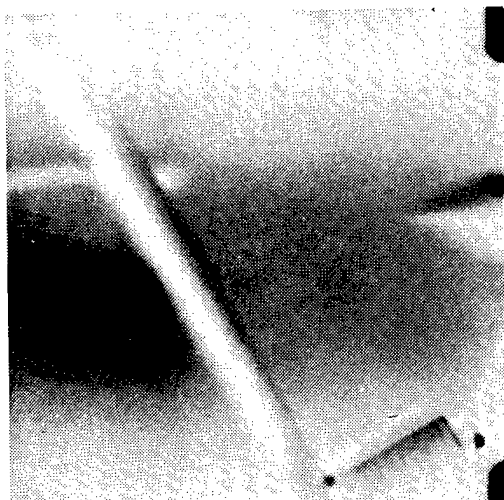


FIGURE 26. Film Sequence at 30-Degree Obliquity for Run No. B-41 from Framing Camera. Rate: 10^4 pictures per second.

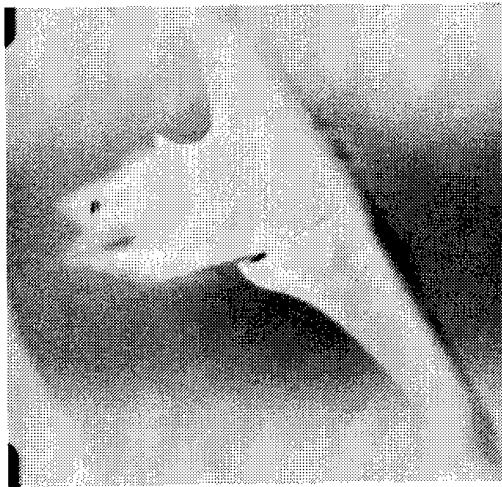
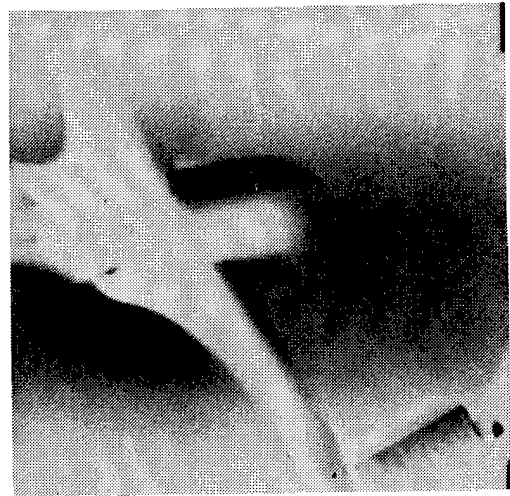
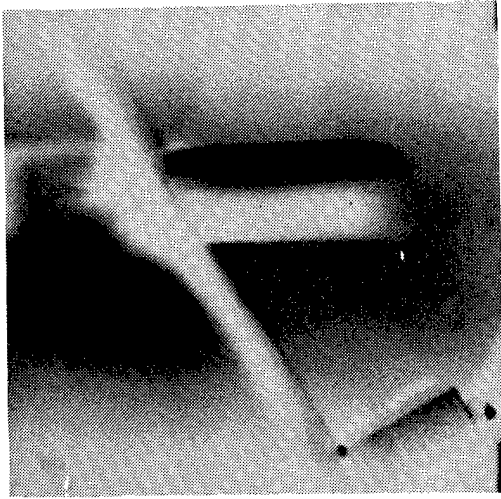


FIGURE 26. (Contd.)

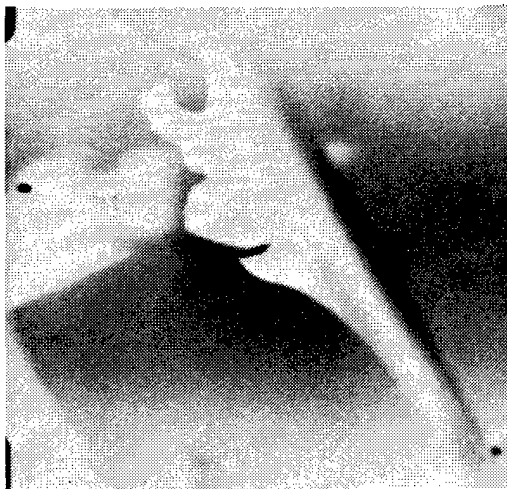
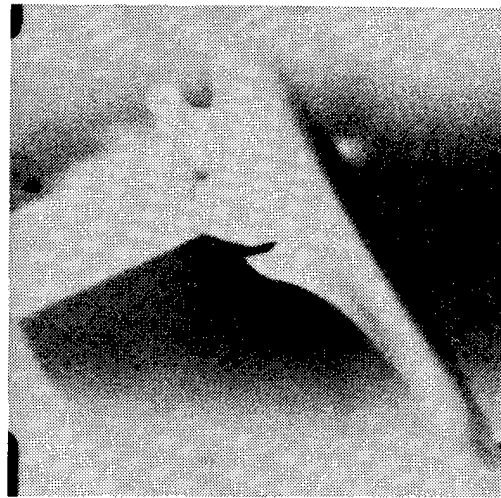
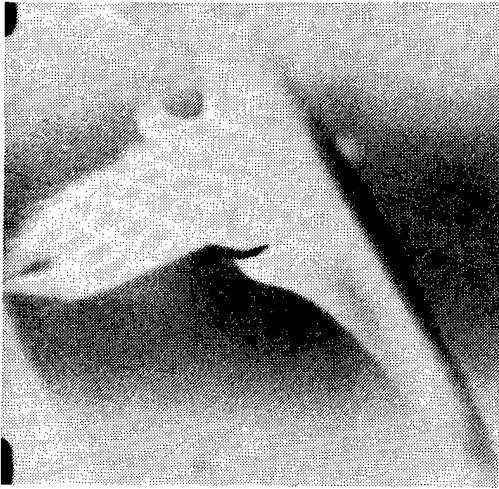


FIGURE 26. (Contd.)

reasonable history of this angular change, say of the order of 12-16 frames, it would be necessary to record the event at a rate of about 150,000 frames/s.

Two special series of tests were conducted to ascertain the ballistic limit of 3.175 mm thick 2024-0 aluminum targets when struck by both blunt and 60-degree conically headed projectiles at normal incidence, and to note the initiation of cracking in 3.175- and 1.78-mm plates of this material. The results are presented in Table 3 for two different masses of each type of striker. The ballistic limit for the 37.7-g blunt and 37.1-g cylindro-conical projectiles was 87.8 m/s and the range was 82.3 to 88.4 m/s, respectively; in the second set of experiments, the projectiles protruded about the same amount over the velocity regime indicated. The ballistic limits for blunt and cylindro-conical strikers with the same mass of 28.9 g were found to be 105.2 m/s and 94.8 m/s. Other ballistic limits are shown in Figure 27. Some of these (and succeeding) data points represent merely non-perforation (i.e., velocities at or below the ballistic limit).

The variation of the non-dimensional velocity drop $(v_i - v_f)/v_i$ as a function of angle of incidence is portrayed in Figures 28 through 31 for the impact of the cylindro-conical projectile on 3.175- and 6.35-mm-thick aluminum and mild steel targets for various initial velocities. In spite of substantial scatter, particularly near the two extreme limits of the ordinate, the general trend of these curves is concave upward, with a minimum value exhibited in the range from 20 to 30 degrees at the higher velocities. The scatter of the data is due to deviations in position determination of the projectile occasioned both by further velocity reductions beyond the last Kerr cell photograph if recorded while the projectile was still passing through the plate, and by inherent scaling and measurement errors as well as yaw. The non-dimensional velocity drop occurring in blunt steel projectiles impacting aluminum and in blunt aluminum projectiles striking both types of targets at various velocities and normal incidence is depicted in Figures 32 and 33 as a function of target thickness, while that for blunt steel strikers impacting both at normal incidence and at 40 degrees obliquity on steel targets is shown in Figure 34 in similar fashion. Obviously, greater target depths generate substantial increases in the velocity difference, with greater effects at lower velocities, but the angle of incidence within the range covered here appears to play a secondary role in the diminution of the projectile speed. Considerable uncertainty exists concerning the exact values of the ballistic limits, in view of substantial scatter of the data as may be noted by inspection of Figures 28 and 31. This parameter is significantly affected by even the slightest yaw; both the blunt and cylindro-conical projectiles exhibit different geometries at impact as the

TABLE 3. Results of Ballistic Limit Tests on 2024-0 Aluminum at Normal Incidence.

Run No.	Projectile		Initial velocity, m/s	Target thickness, mm	Ballistic end result	Plug mass, g
	Head	Mass, g				
D-1	C	28.9	99.7	3.175	Petal perforation	---
D-2	C	28.9	94.8	3.175	No perforation	---
D-3	C	28.9	96.0	3.175	Petal perforation	---
D-4	C	28.9	96.0	3.175	Petal perforation	---
D-5	C	28.9	90.2	3.175	Bulge, long cracks, central hole	---
D-6*	C	28.9	87.8	3.175	Half cone length perforated, petals	---
D-7	C	28.9	60.7	3.175	Spherical bulge, 4 cracks, small hole	---
D-8	C	28.9	57.0	3.175	Cracked distal surface	---
D-9	C	28.9	45.7	3.175	Bulge, incipient crack formation	---
D-10	C	28.9	42.0	3.175	Slight bulge, no cracking discernible	---
D-11	B**	28.9	91.2	3.175	No perforation	---
D-12	B	28.9	96.6	3.175	No perforation	---
D-13	B	28.9	101.2	3.175	No perforation	---
D-14	B	28.9	106.7	3.175	Perforated	0.9
D-15	B	28.9	103.7	3.175	No perforation	---
D-16	B	28.9	104.9	3.175	No perforation	---
D-17	B	28.9	105.5	3.175	Perforated	Plug lost
D-18	C	37.1	85.7	3.175	Lodged in target	Petals only
D-19	C	37.1	87.2	3.175	Lodged in target	Petals only
D-20	C	37.1	88.4	3.175	Lodged in target	Petals only
D-21	C	37.1	88.4	3.175	Perforated	Petals only
D-22	C	37.1	83.8	3.175	Lodged in target	Petals only
D-23	C	37.1	80.8	3.175	Did not perforate	---
D-24	B	37.7	112.5	3.175	Perforated	0.9
D-25	B	37.7	98.8	3.175	Perforated	0.9
D-26	B	37.7	90.2	3.175	Perforated	0.97
D-27	B	37.7	80.5	3.175	No perforation	---
D-28	B	37.7	87.2	3.175	No perforation	---
D-29	B	37.7	87.8	3.175	Perforated and embedded	1.0
D-30	H	28.7	106.7	3.175	Hemispherical bulge with shear zone for plug	---
D-31	C	28.9	19.4	1.78	Bulge with incipient cracks	---
D-32	C	28.9	27.2	1.78	Bulge, 4 short cracks, central hole	---

* Target effects anomalous, expected at higher speed.

** Tests D-11 to D-17 used the striker of Runs D-1 to D-9 turned 180 degrees.

C = 60-degree cylindro-conical hard steel projectile, 12.7 mm diameter.

B = Blunt hard-steel projectile, 12.7 mm diameter.

H = Hemispherically-tipped projectile, 12.7 mm diameter.

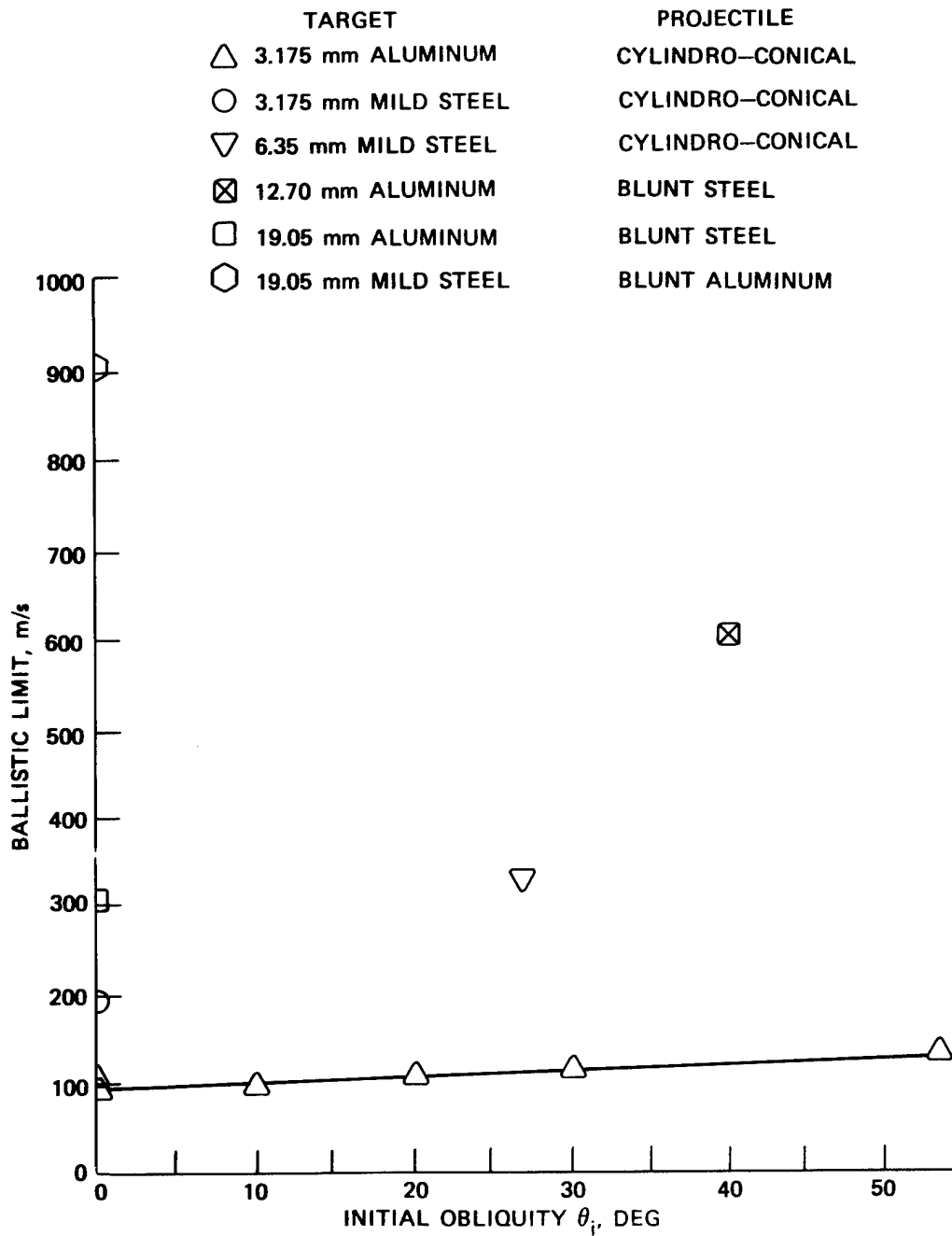


FIGURE 27. Ballistic Limit as a Function of Initial Obliquity for Various Projectile-Target Combinations.

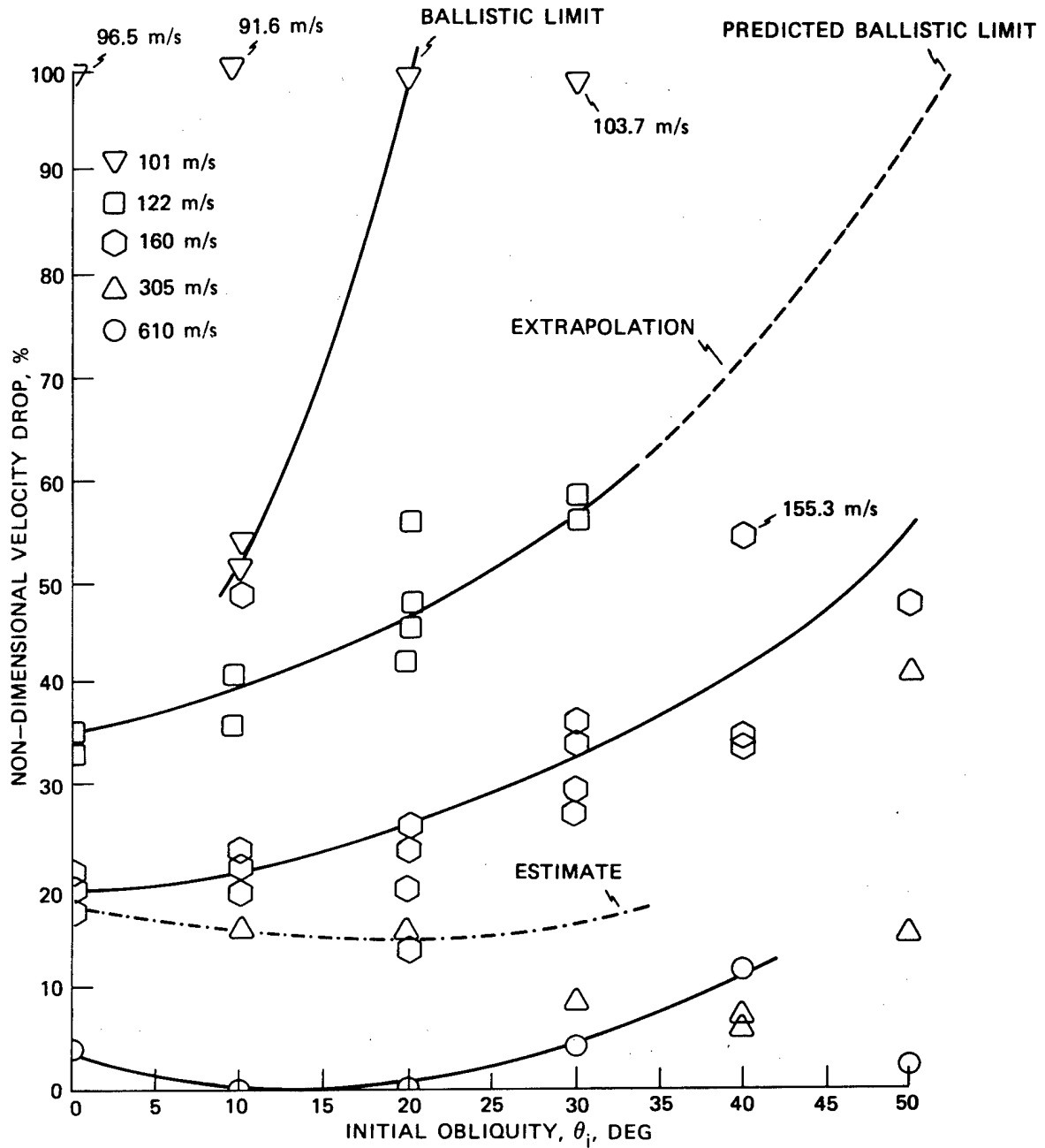


FIGURE 28. Non-Dimensional Velocity Drop as a Function of Initial Obliquity for 3.175-mm-Thick 2024-O Aluminum Targets Struck by Cylindro-Conical Projectiles.

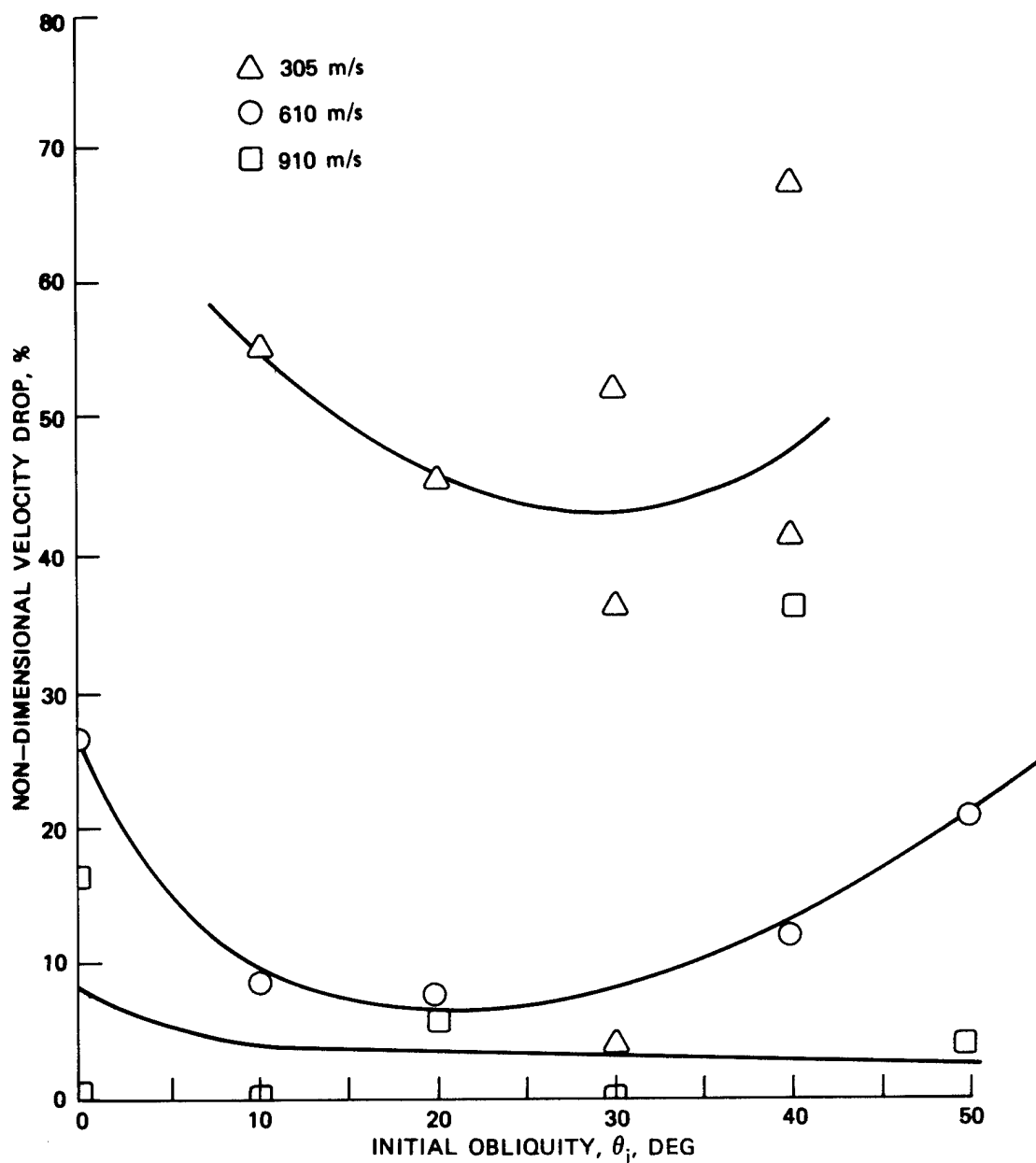


FIGURE 29. Non-Dimensional Velocity Drop as a Function of Initial Obliquity for 6.35-mm-Thick 2024-O Aluminum Targets Struck by Cylindro-Conical Projectiles.

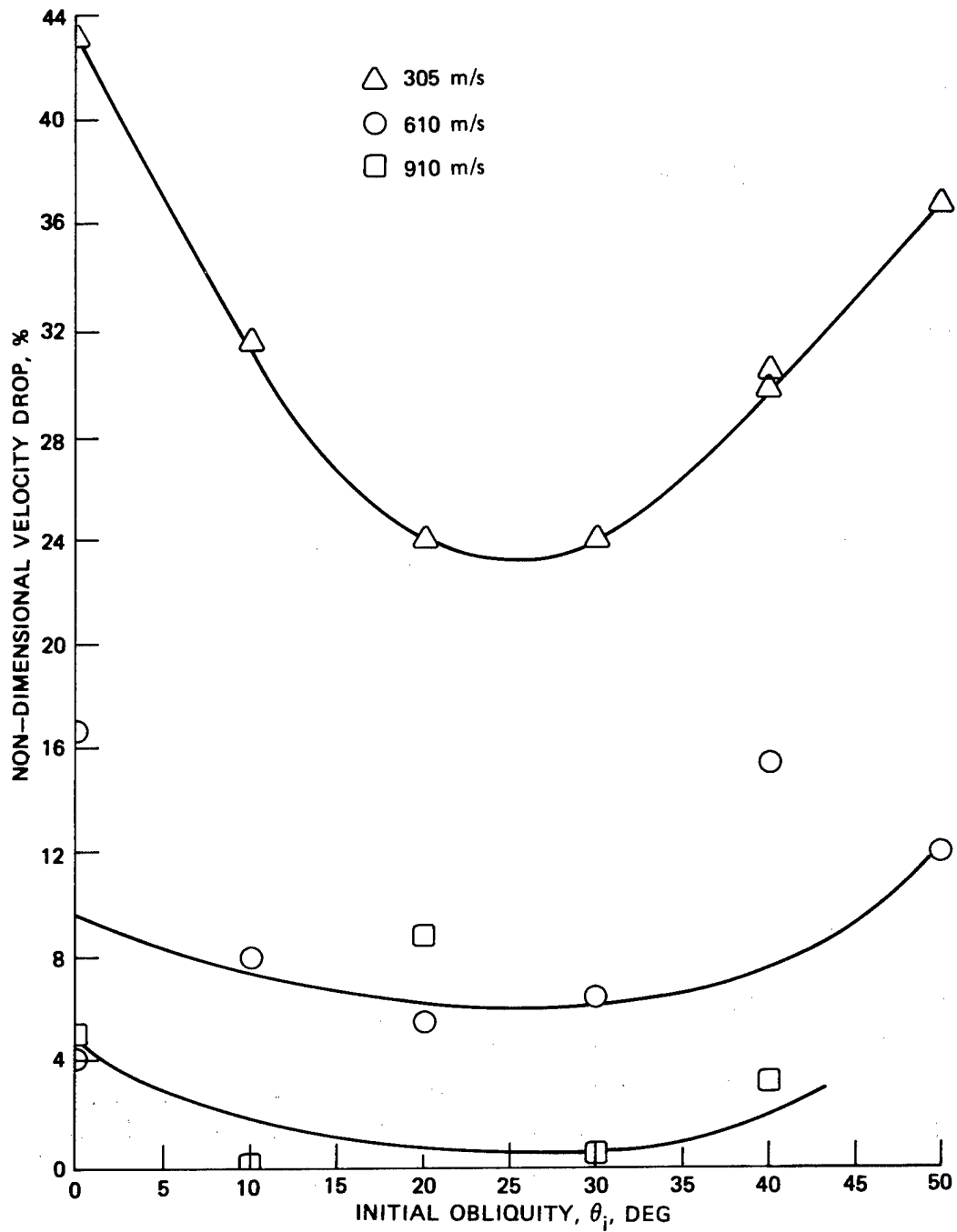


FIGURE 30. Non-Dimensional Velocity Drop as a Function of Initial Obliquity for 3.175-mm-Thick Mild Steel Targets Struck by Cylindro-Conical Projectiles.

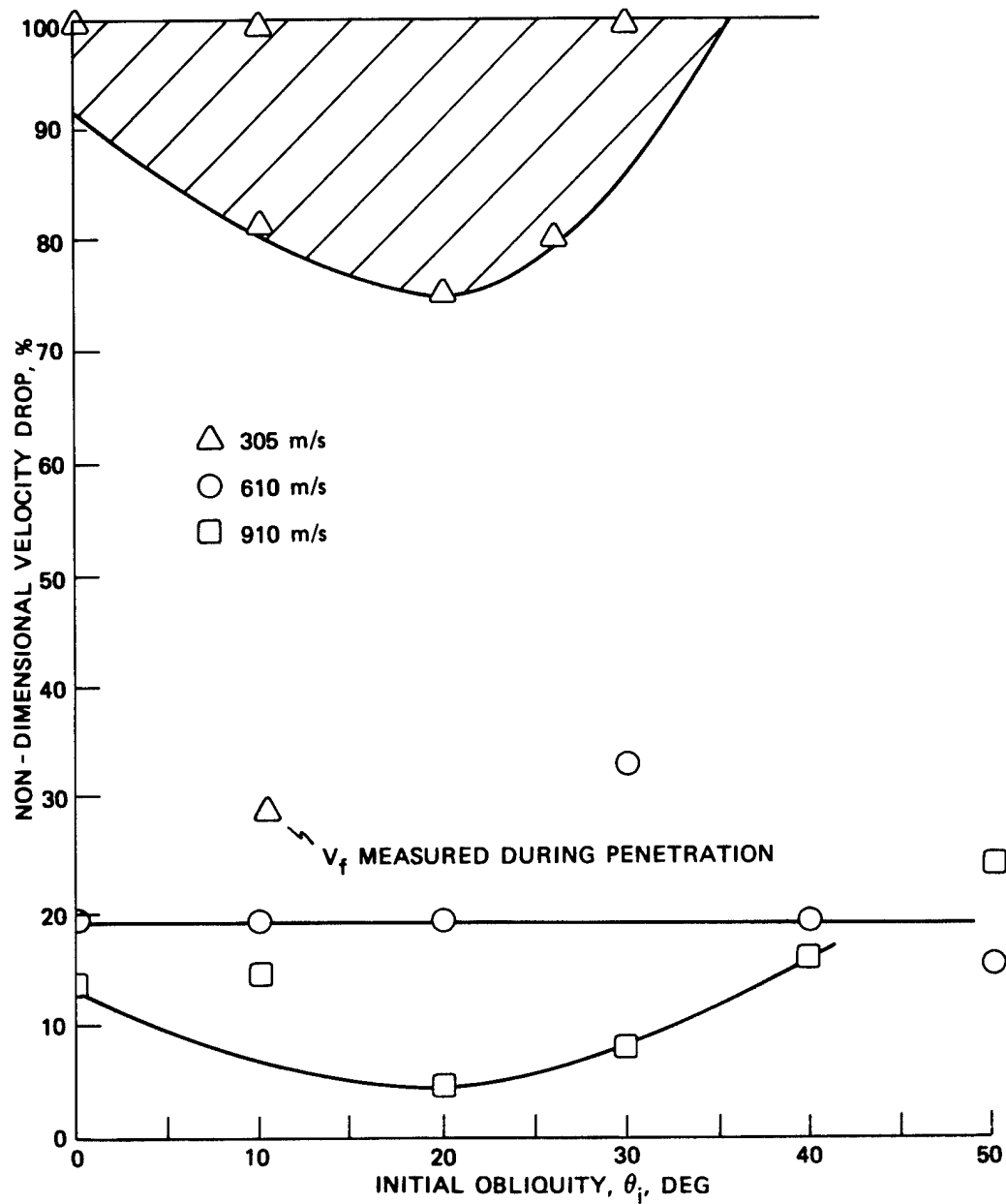


FIGURE 31. Non-Dimensional Velocity Drop as a Function of Initial Obliquity for 6.35-mm-Thick Mild Steel Targets Struck by Cylindro-Conical Projectiles.

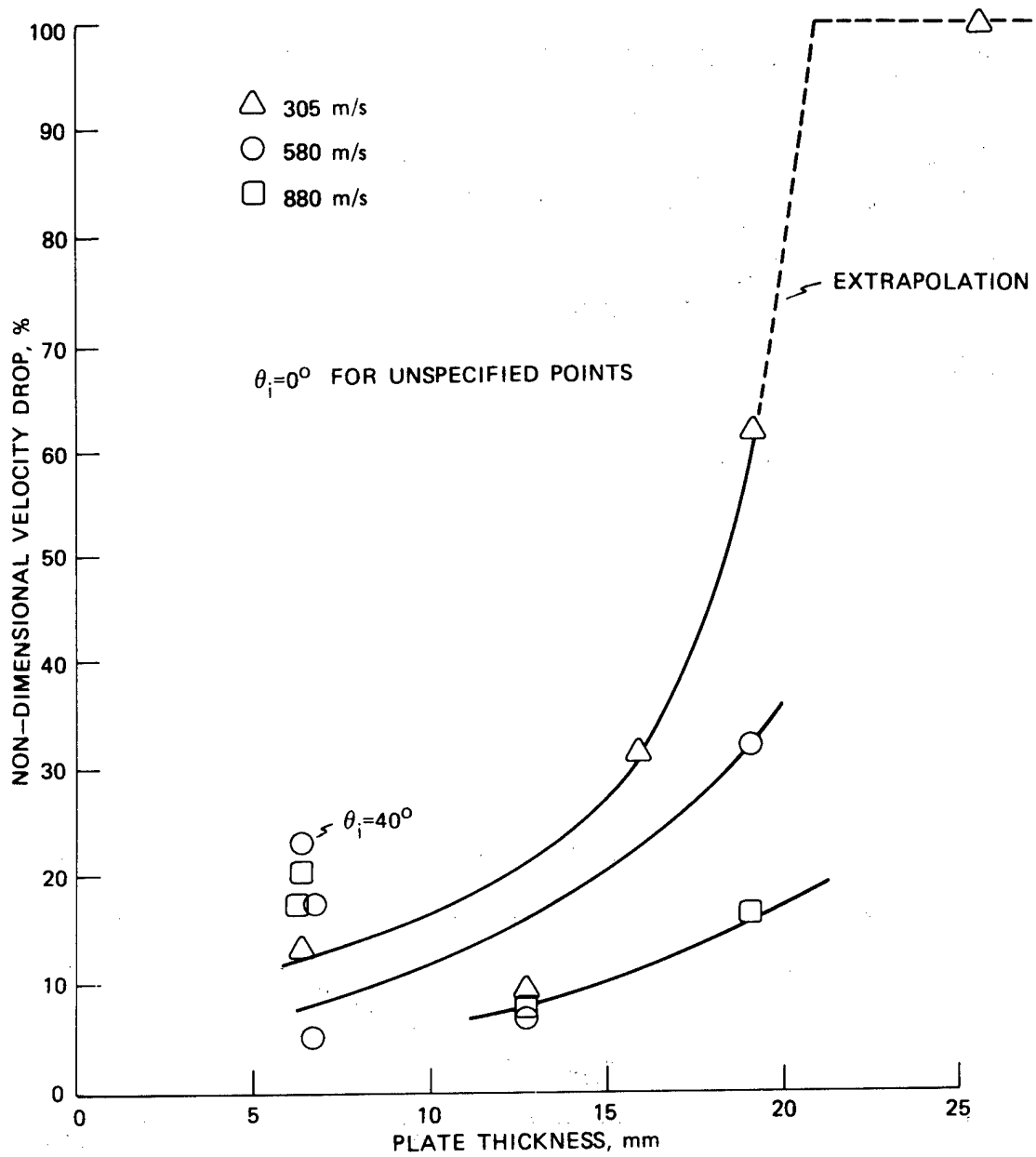


FIGURE 32. Non-Dimensional Velocity Drop as a Function of Plate Thickness for 2024-O Aluminum Targets Struck by Blunt Hard-Steel Projectiles.

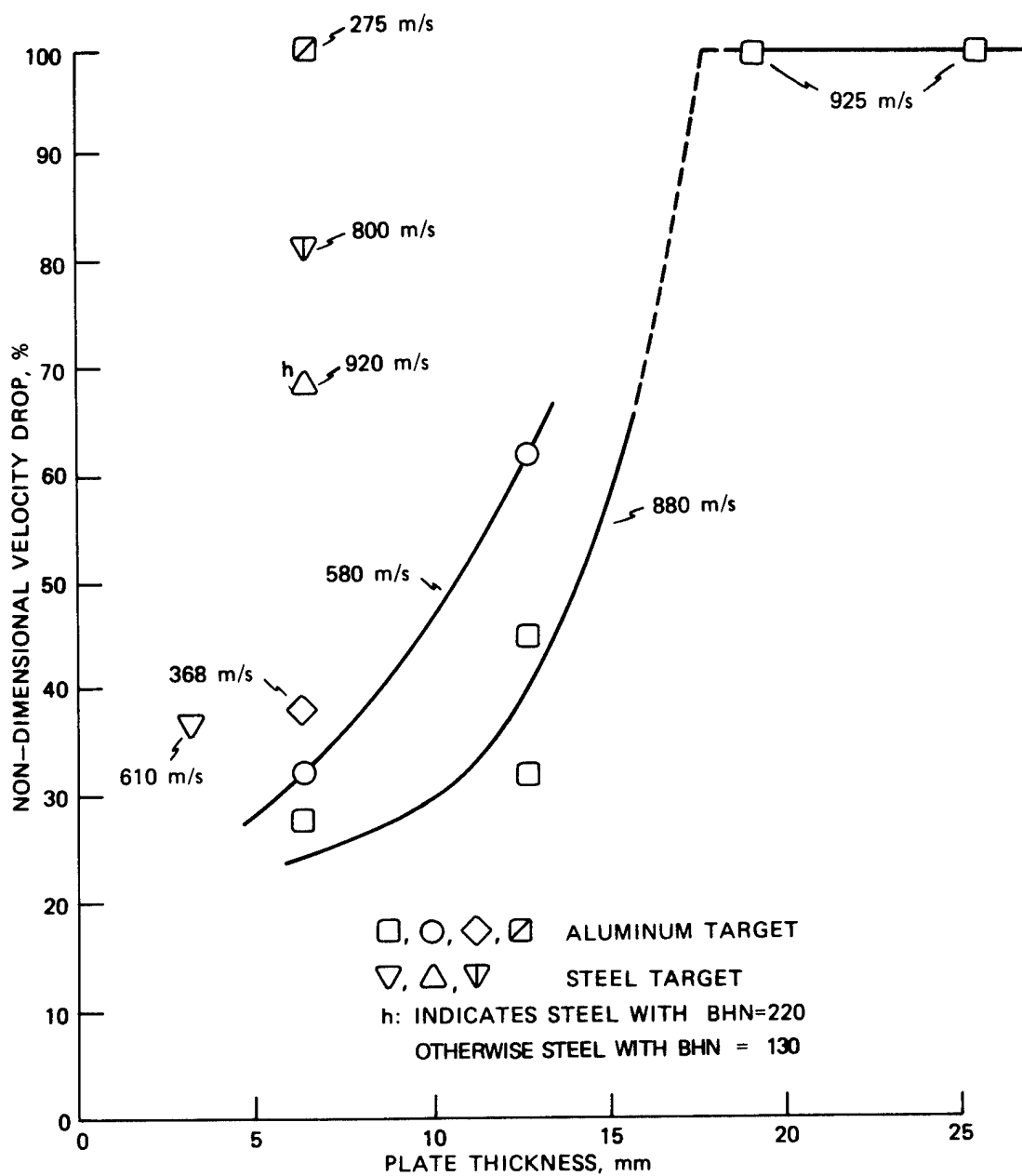


FIGURE 33. Non-Dimensional Velocity Drop as a Function of Plate Thickness for Various Targets Struck at Normal Incidence by Blunt Soft Aluminum Projectiles.

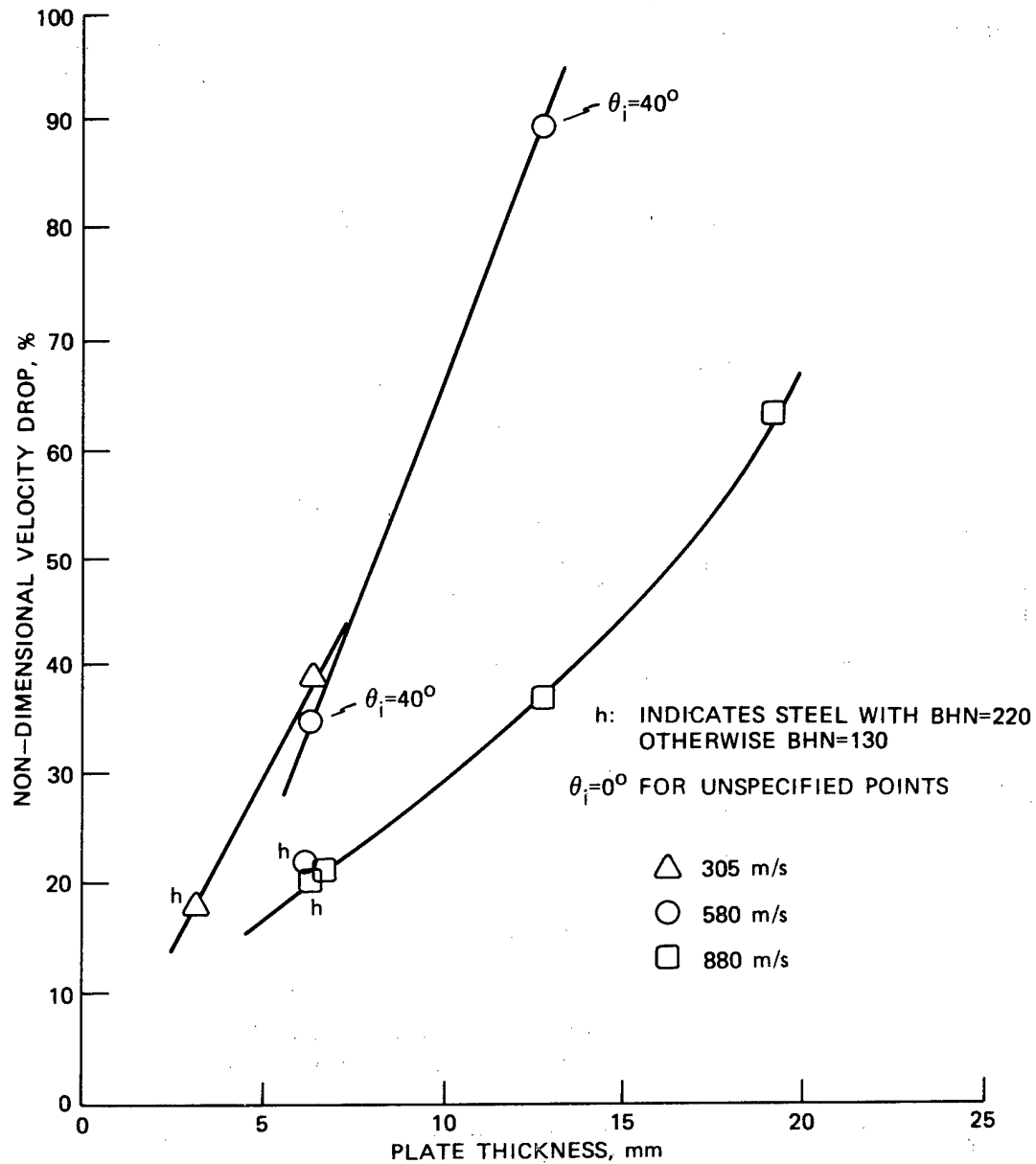


FIGURE 34. Non-Dimensional Velocity Drop as a Function of Plate Thickness for Mild and Medium Carbon Steel Targets Struck by Blunt Hard-Steel Projectiles.

result of such motion. However, as shown in Figure 27, an increase in obliquity for the same target-projectile combination results in only a slight increase in this limit, which can be linearly related to obliquity for thin, soft targets. Furthermore, the ballistic limit of a mild steel target for a cylindro-conical steel projectile impact was about double that for a 2024-0 aluminum plate.

The final projectile direction, θ_f , has been plotted in Figures 35-38 as a function of initial obliquity, θ_i , for the perforation of 60-degree cylindro-conical projectiles fired at various velocities against 3.175 and 6.35-mm-thick 2024-0 aluminum and mild steel targets, respectively. The first of these shows a significant concave upward trend at the lower velocities, indicating the larger changes in direction with increase in initial obliquity. The plots exhibit a nearly linear relationship for the higher initial velocities encompassed there; a threefold decrease in velocity for the thicker aluminum target reduces the final obliquity by about 8 degrees for an initial angle of incidence of 50 degrees. The data in Figure 38, encompassing velocities differing by 3:1, are the only information obtained that can be well represented by a single linear relation. This set of results applies to targets affording the greatest resistance to penetration at obliquity employed in the current investigation. A crossplot of this information for these targets in terms of the deflected angle, $\Delta\theta$, is shown in Figures 39-42. The results plotted for the change in obliquity, $\Delta\theta$, shown in Figures 39-42, are expected to exhibit a substantial amount of scatter in view of the sensitivity of the dependent variable on slight errors in measurement. In particular, the data presented in Figure 41 illustrate the degree of this scatter to the point where the experimental information can not even be depicted by a pattern.

Representative terminal target configurations are shown in Figures 43-60. In general, the conically headed projectile produced petalling of the target, while the blunt aluminum and steel strikers generated plugs. Plugs produced by the soft, blunt projectile were generally hemispherical in shape, with a curved rear surface matching the mushroomed deformed front portion of the projectile. Plug masses increased with target thickness, but the previously noted decrease in the central plug thickness to an asymptote with increasing impact speed for tests involving normal impact of hard-steel spheres (Reference 2) could not be totally verified in the present sequence of tests since efforts were not concentrated on this feature. A special and intensive investigation is required for an evaluation of the plug mass and dimensional variations with striker speed. The sharp-nosed projectiles frequently exhibited a small permanent deformation of the tip in the ricochet direction under oblique impact conditions against the thicker steel targets. The perforation phenomenon for Run C-111 (Figure 61) was highly unusual in that the embedment of the projectile

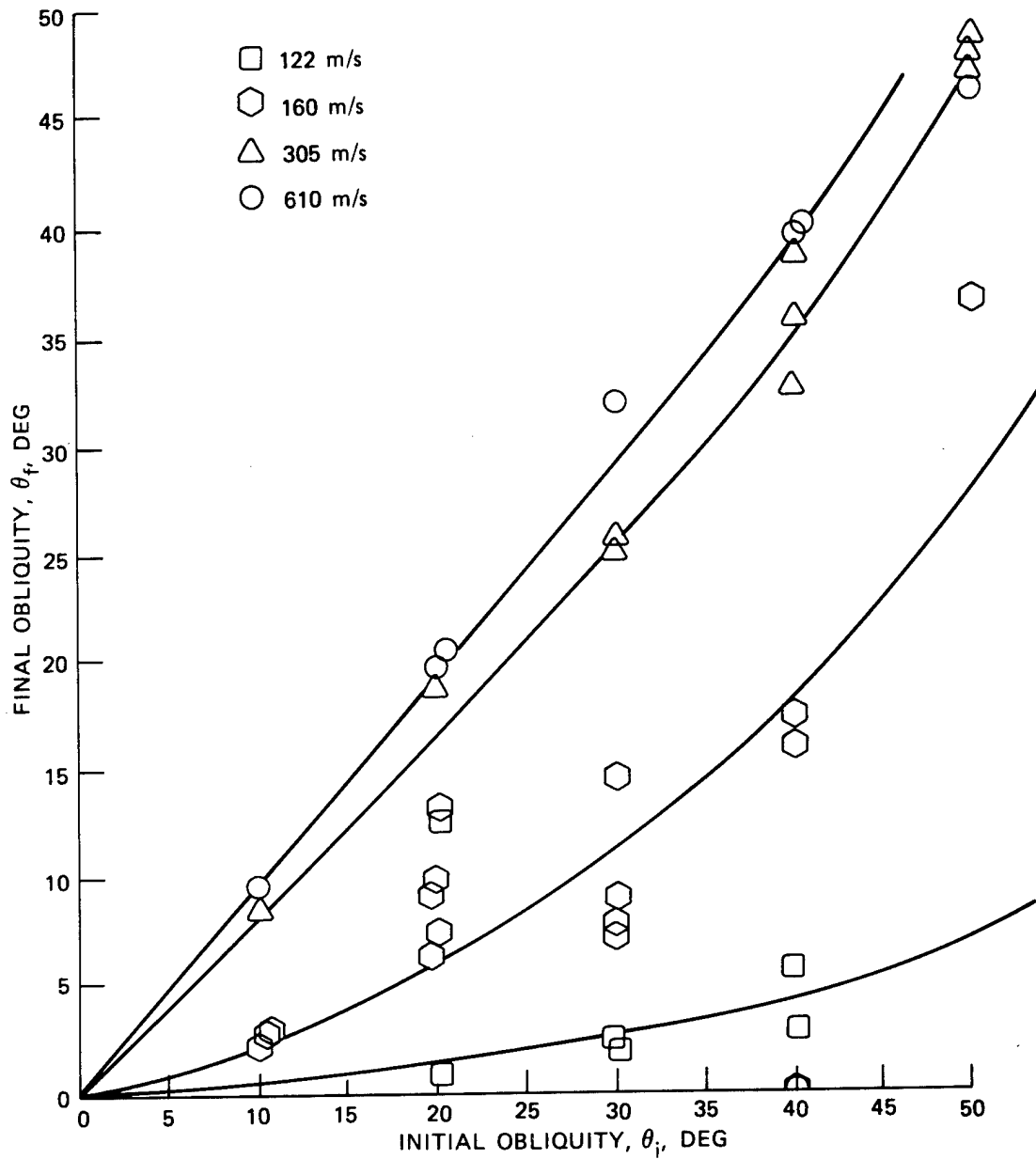


FIGURE 35. Final Obliquity as a Function of Initial Obliquity for 3.175-mm-Thick 2024-O Aluminum Targets Struck by Cylindro-Conical Hard-Steel Projectiles.

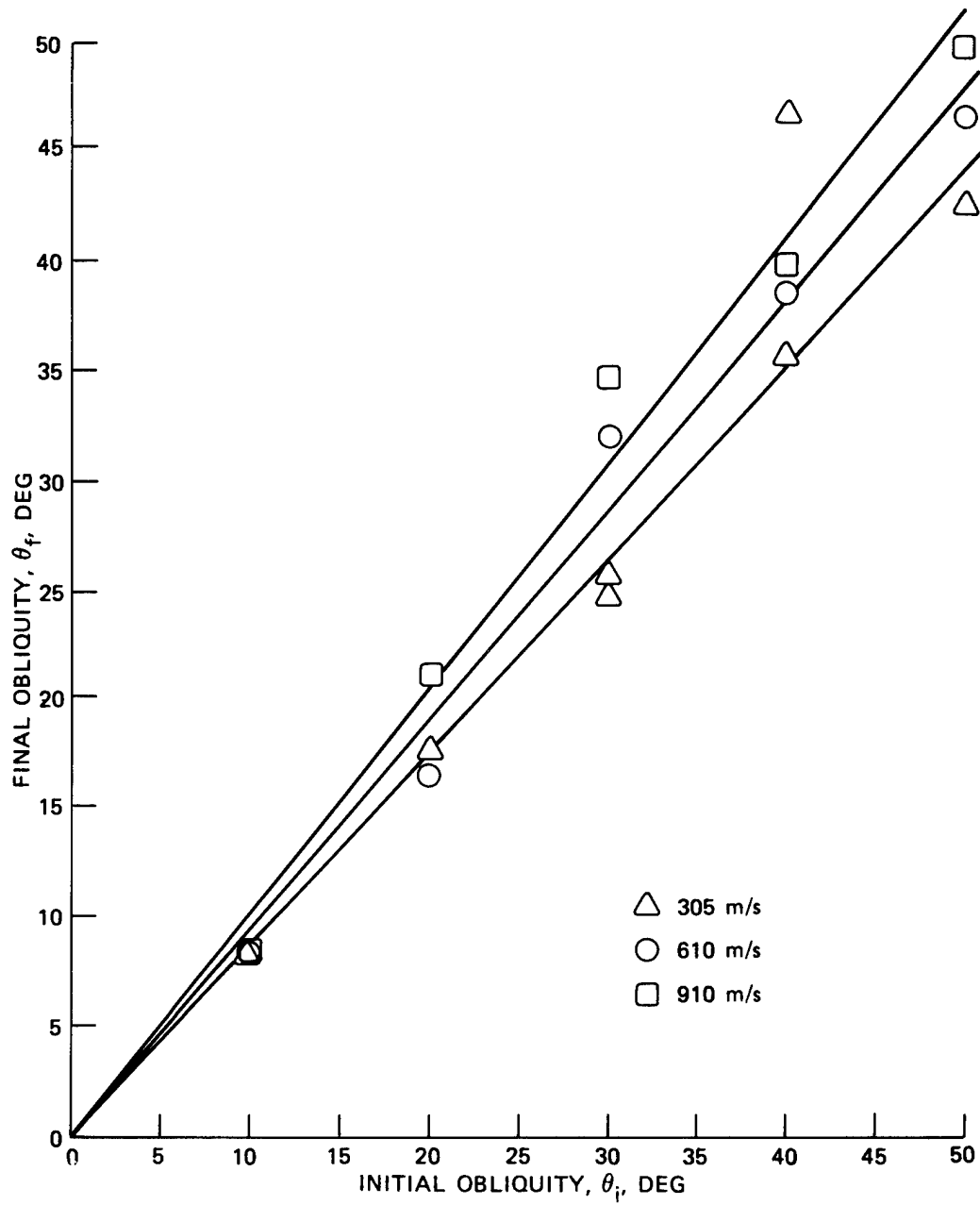


FIGURE 36. Final Obliquity as a Function of Initial Obliquity for 6.35-mm-Thick 2024-O Aluminum Targets Struck by Cylindro-Conical Hard-Steel Projectiles.

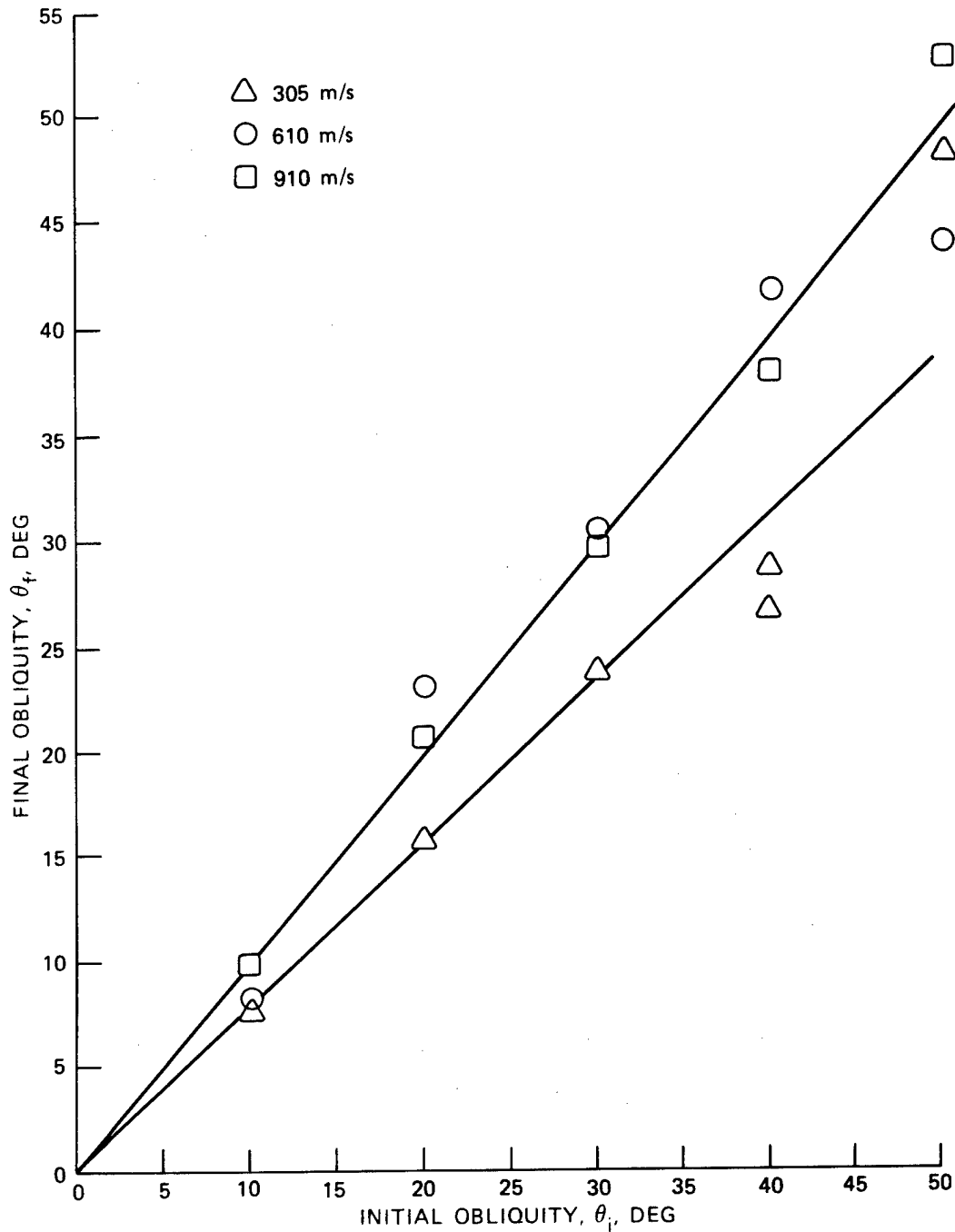


FIGURE 37. Final Obliquity as a Function of Initial Obliquity for 3.175-mm-Thick Mild Steel Targets Struck by Cylindro-Conical Hard-Steel Projectiles.

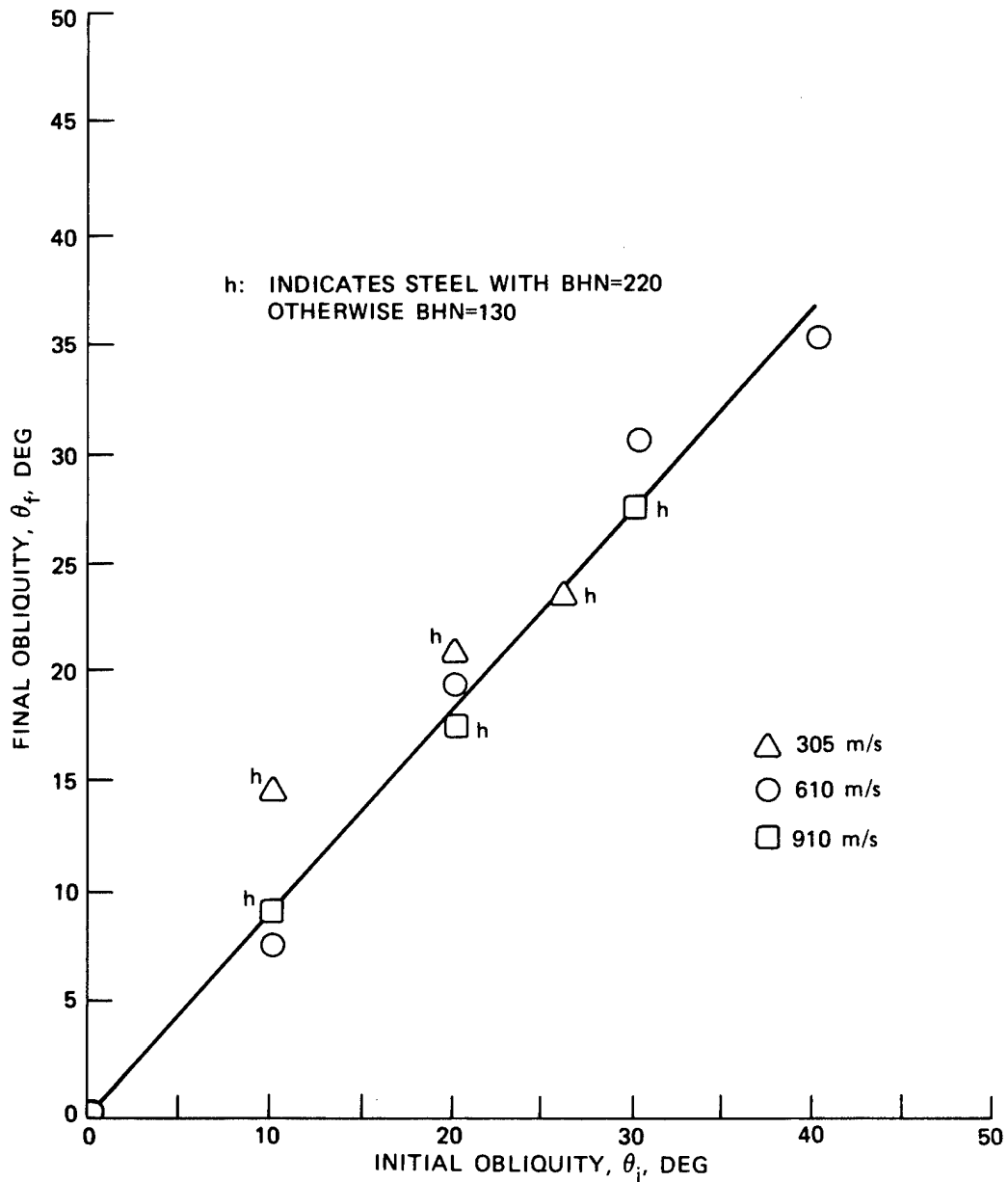


FIGURE 38. Final Obliquity as a Function of Initial Obliquity for 6.35-mm-Thick Mild and Medium Carbon Steel Struck by Cylindro-Conical Hard-Steel Projectiles.

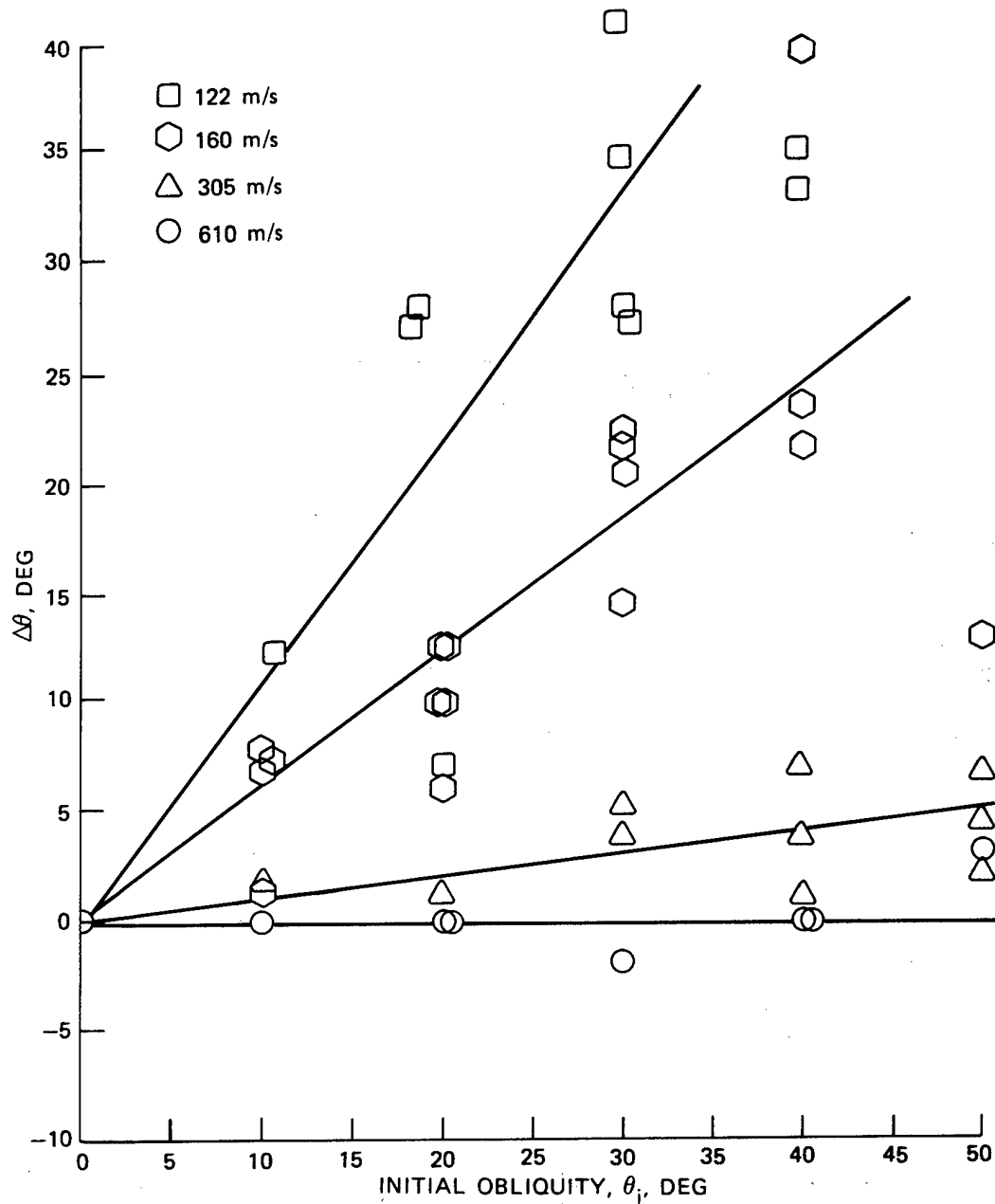


FIGURE 39. Angular Change as a Function of Initial Obliquity for 3.175-mm-Thick 2024-0 Aluminum Targets Struck by Cylindro-Conical Hard-Steel Projectiles.

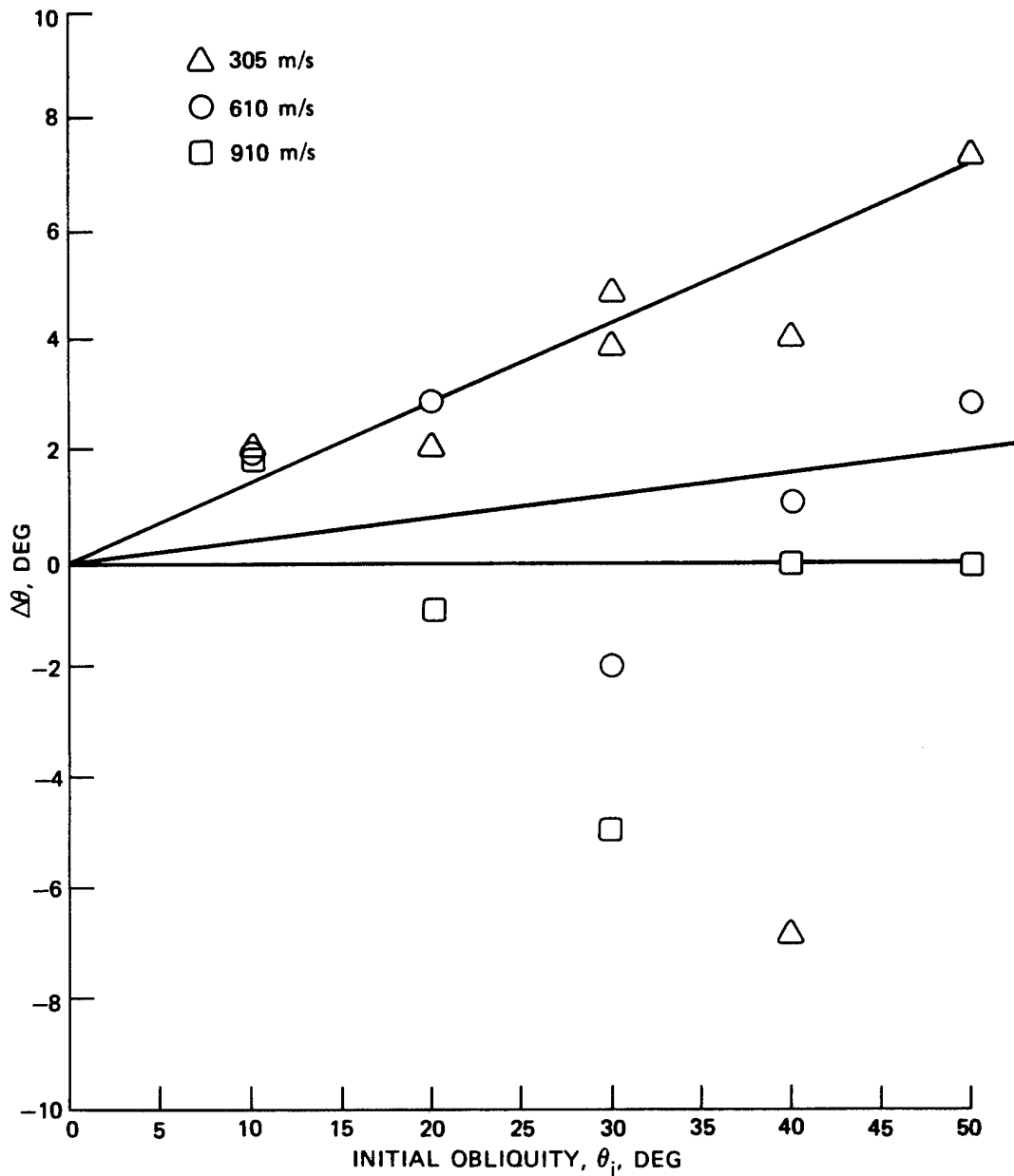


FIGURE 40. Angular Change as a Function of Initial Obliquity for 6.35-mm-Thick 2024-O Aluminum Targets Struck by Cylindro-Conical Hard-Steel Projectiles.

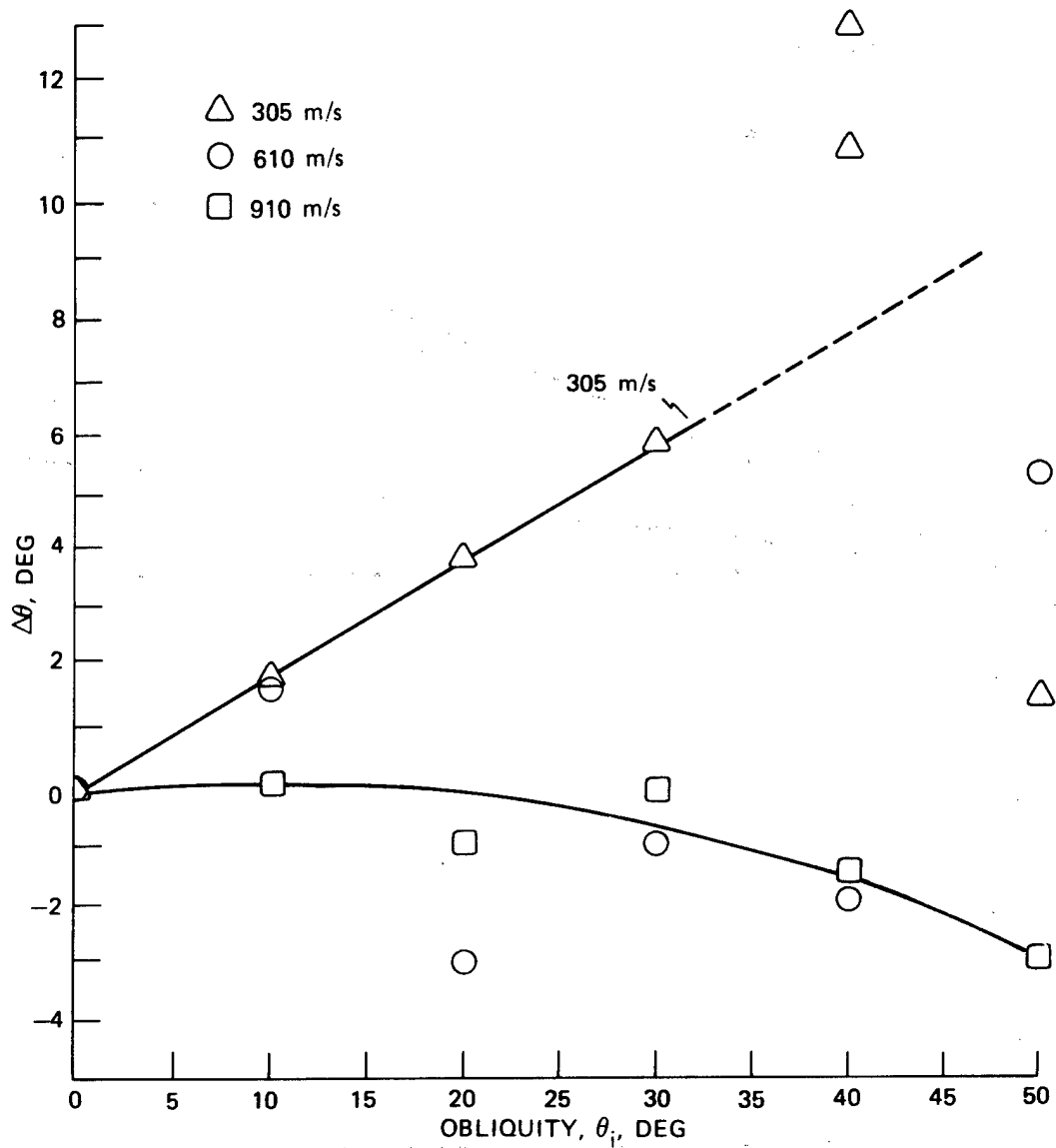


FIGURE 41. Angular Change as a Function of Initial Obliquity for 3.175-mm-Thick Mild Steel Targets Struck by Cylindro-Conical Hard-Steel Projectiles.

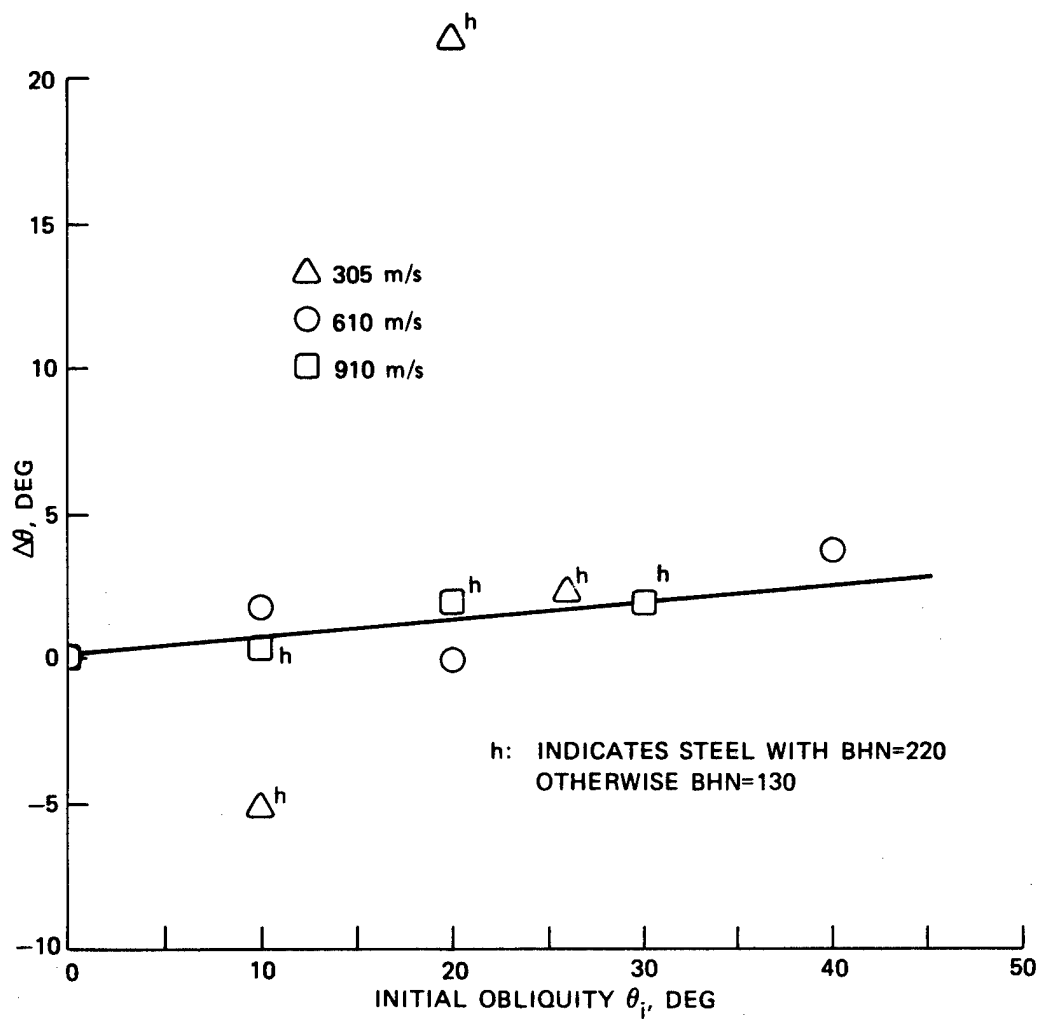


FIGURE 42. Angular Change as a Function of Initial Obliquity for 6.35-mm-Thick Mild and Medium Carbon Steel Targets Struck by Cylindro-Conical Hard-Steel Projectiles.

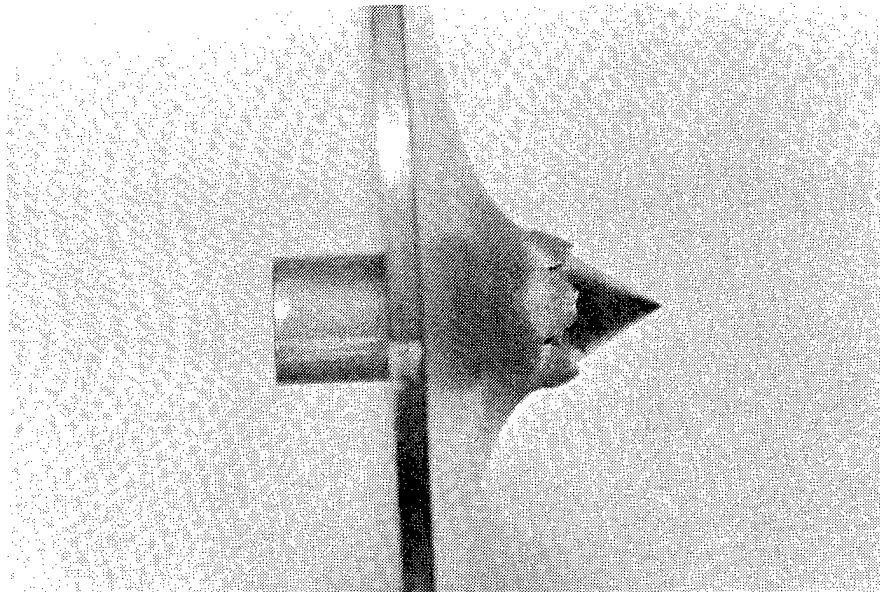
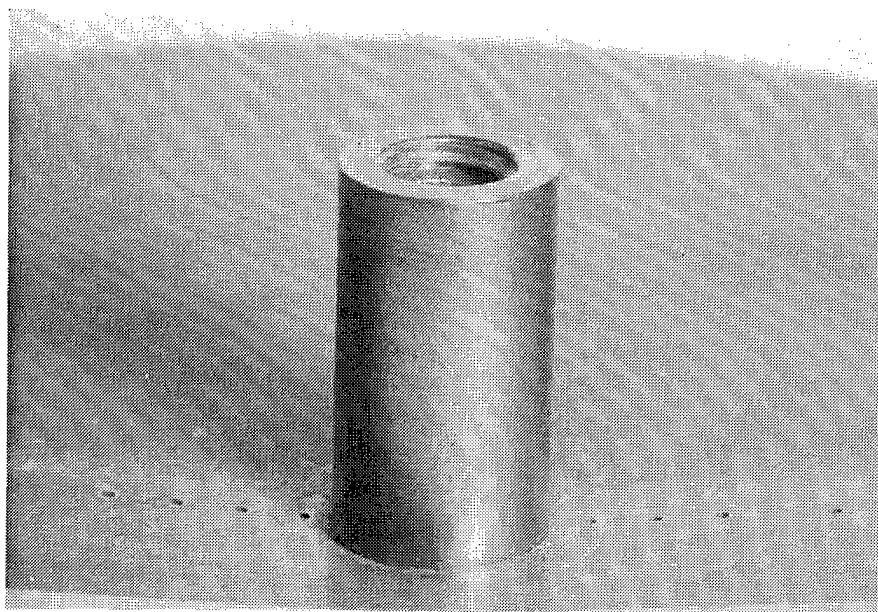


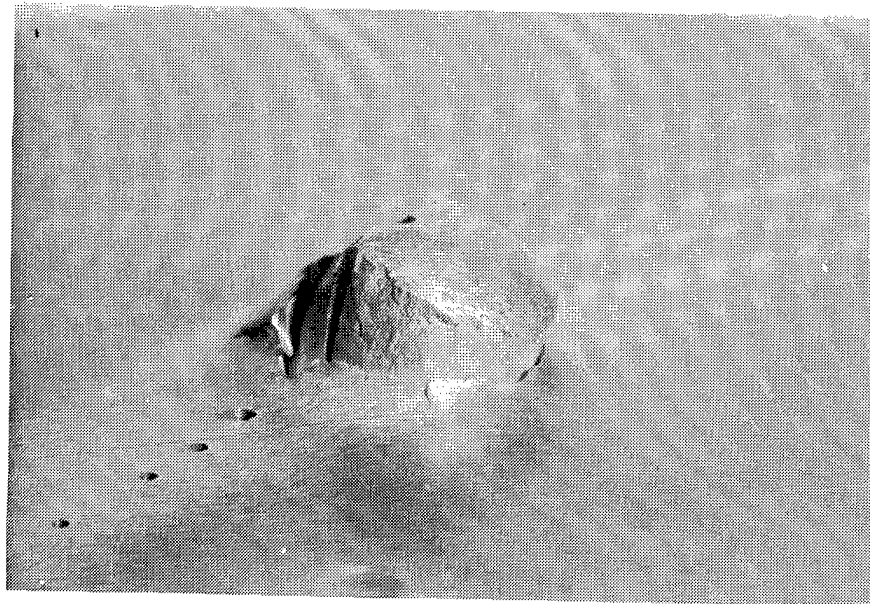
FIGURE 43. Embedment of Cylindro-Conical Steel Projectile in 3.175-mm-Thick Mild Steel Target. (Run B-45)

produced a perforation that resulted in both petalling and plug formation. The general pattern of target damage in numerous instances is comparable to that observed in an earlier investigation involving the perforation of various metallic plates by hard-steel spheres. For blunt projectiles at normal incidence, rings were separated from the target, primarily on the exit side, leaving the perforation diameter generally larger on the distal than on the impact face.

Figure 43 shows the embedment of a cylindro-conical striker in a mild steel target fired at normal incidence, while Figure 44 shows both surfaces of a thicker aluminum plate subjected to normal impact of a blunt steel projectile that produced perforation and embedment. Figures 45 and 46 portray the damage generated at low velocities by a cylindro-conical striker in the same aluminum target at obliquity; significant petalling is produced with the portion of the periphery in the direction of final projectile motion flattened out to form a lip. Damage to a thicker target of this material by the same bullet fired at or near normal incidence at a higher velocity is significantly less, as shown in Figures 47 and 48. In the first photograph the distal side of the crater is characterized by a series of serrations, while embedment is accompanied by a large number of small petals on the impact side flattened against the target to produce a leaf-like appearance. Figures 49-54 show the distal side of the



(a) Impact Side.



(b) Distal Side.

FIGURE 44. Impact of 39.7-g, 12.7-mm Diameter Blunt Hard-Steel Projectile on 12.7-mm-Thick 2024-0 Aluminum Plate at 184.2 m/s and Normal Incidence. Projectile perforated and embedded in the target.

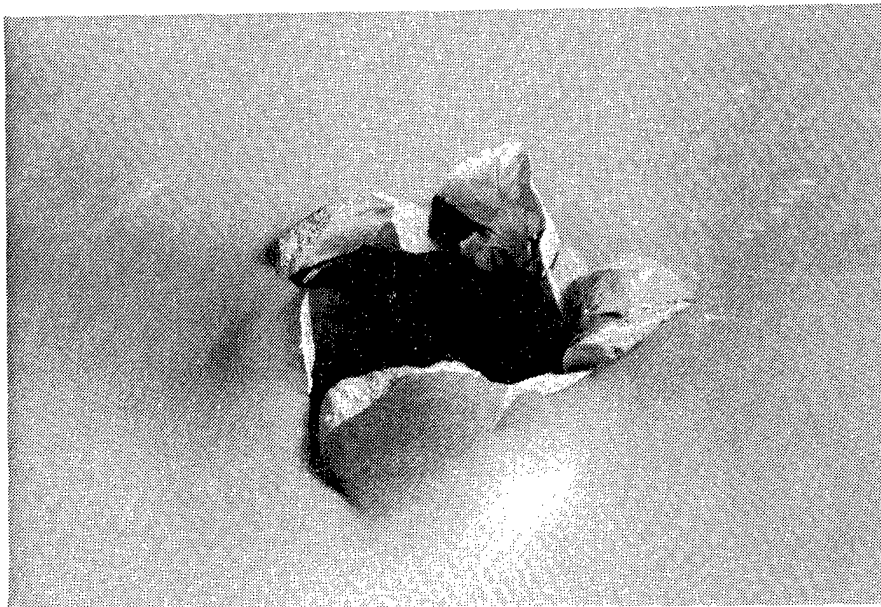


FIGURE 45. Distal Side of a 3.175-mm-Thick Aluminum Target After Perforation by a Cylindro-Conical Steel Projectile. (Run B-35.)

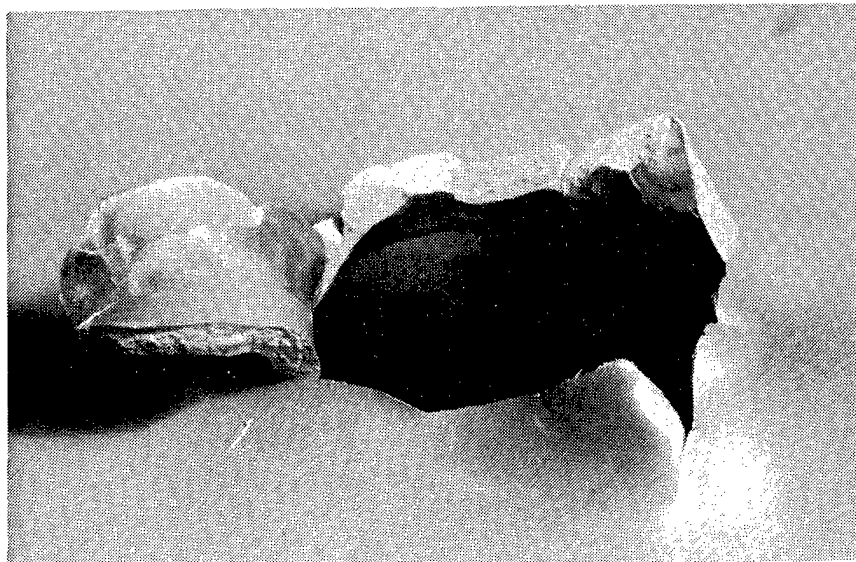
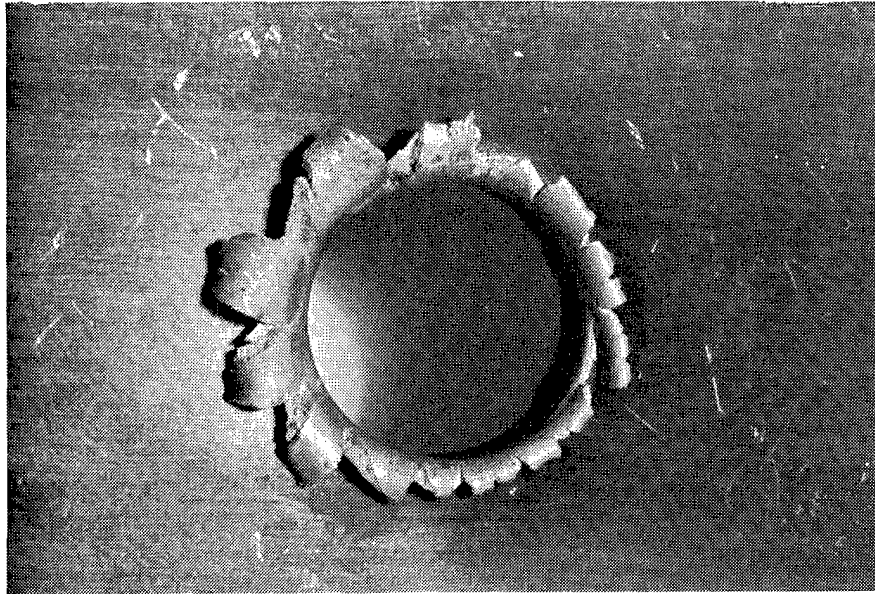
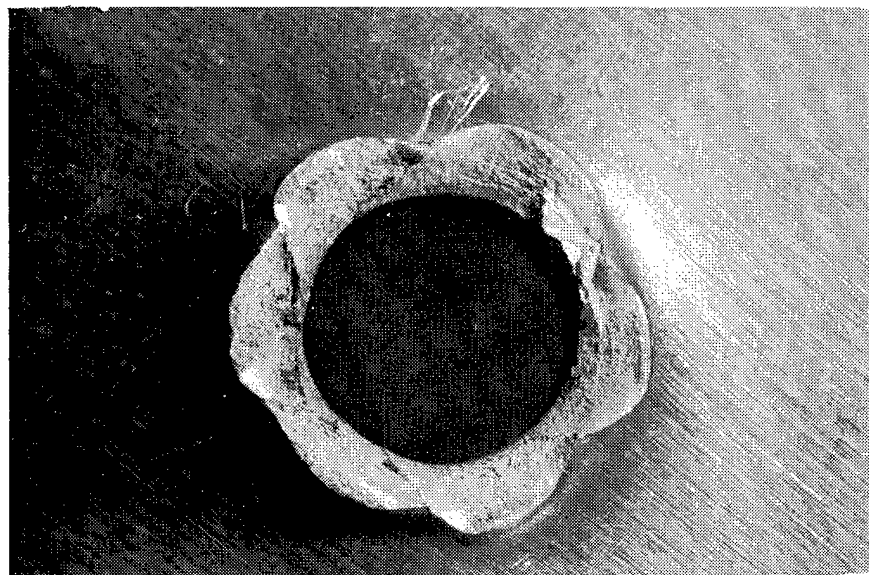


FIGURE 46. Distal Side of a 3.175-mm-Thick Aluminum Target After Oblique Perforation by a Cylindro-Conical Steel Projectile. (Run B-36.)

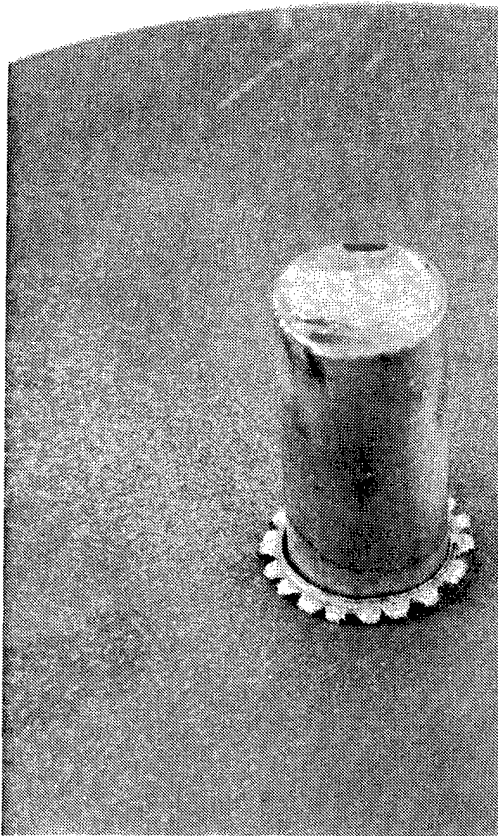


(a) Impact Side.



(b) Distal Side.

FIGURE 47. Impact and Distal Sides of a 6.35-mm-Thick Aluminum Target After Oblique Perforation by a Cylindro-Conical Steel Projectile. (Run C-9.)

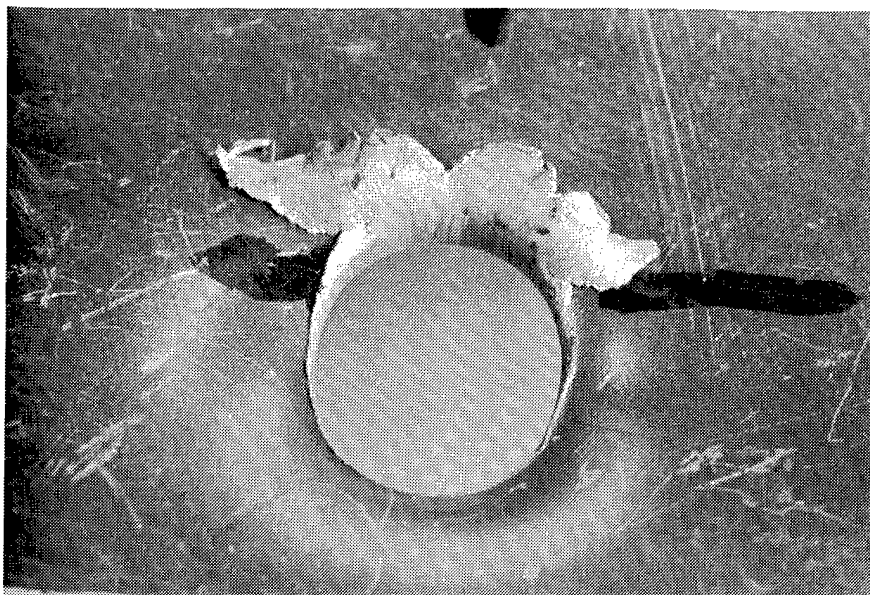


(a) Impact Side.

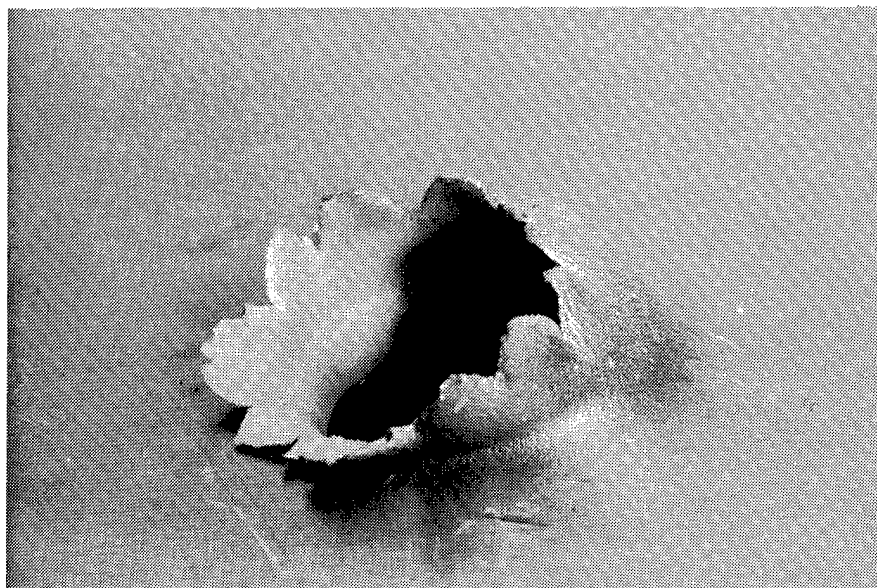


(b) Distal Side.

FIGURE 48. Impact and Distal Sides of a 6.35-mm-Thick Mild Steel Target Struck Obliquely by a Cylindro-Conical Steel Projectile. (Run C-60.)

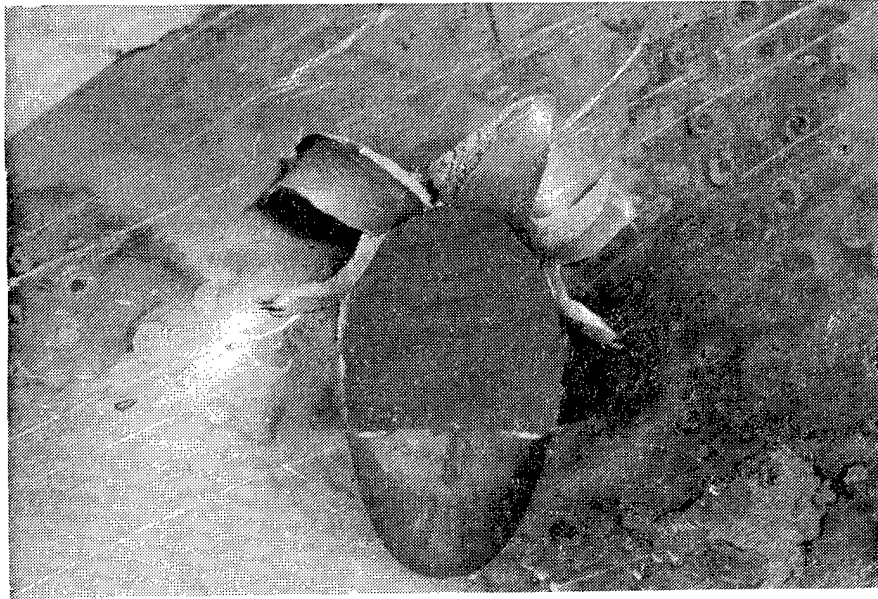


(a) Impact Side.

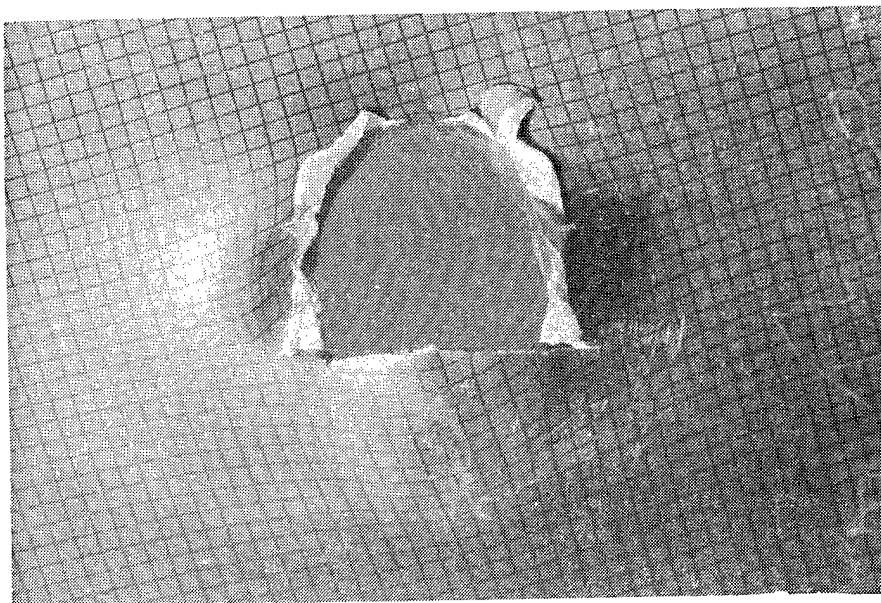


(b) Distal Side.

FIGURE 49. Impact and Distal Sides of a 3.175-mm-Thick Aluminum Target After Oblique Perforation of a Cylindro-Conical Steel Projectile. (Run C-67.)



(a) Impact Side.



(b) Distal Side.

FIGURE 50. Impact and Distal Sides of a 3.175-mm-Thick Aluminum Target After Oblique Perforation by a Cylindro-Conical Steel Projectile. (Run C-22.)

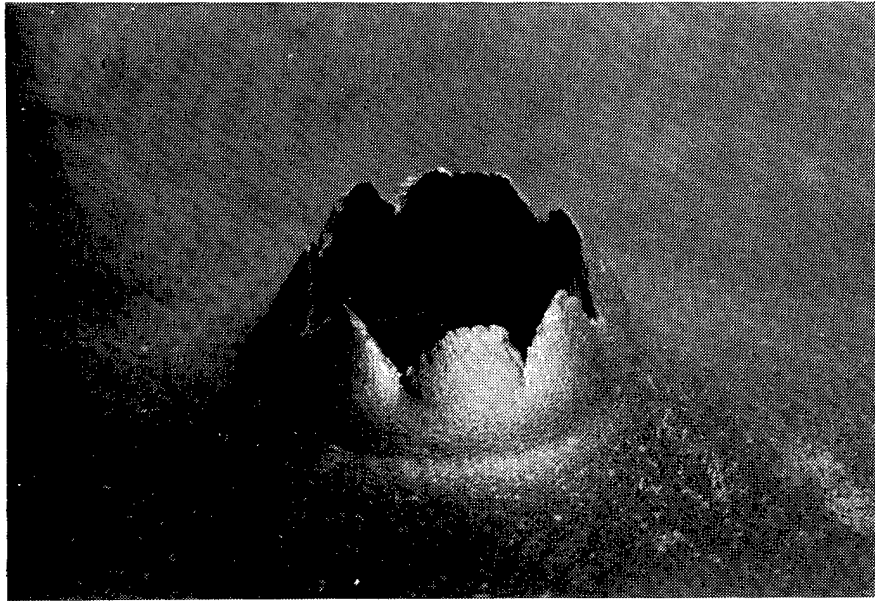


FIGURE 51. Distal Side of a 3.175-mm-Thick Mild Steel Target After Oblique Perforation by a Cylindro-Conical Steel Projectile. (Run C-8.)

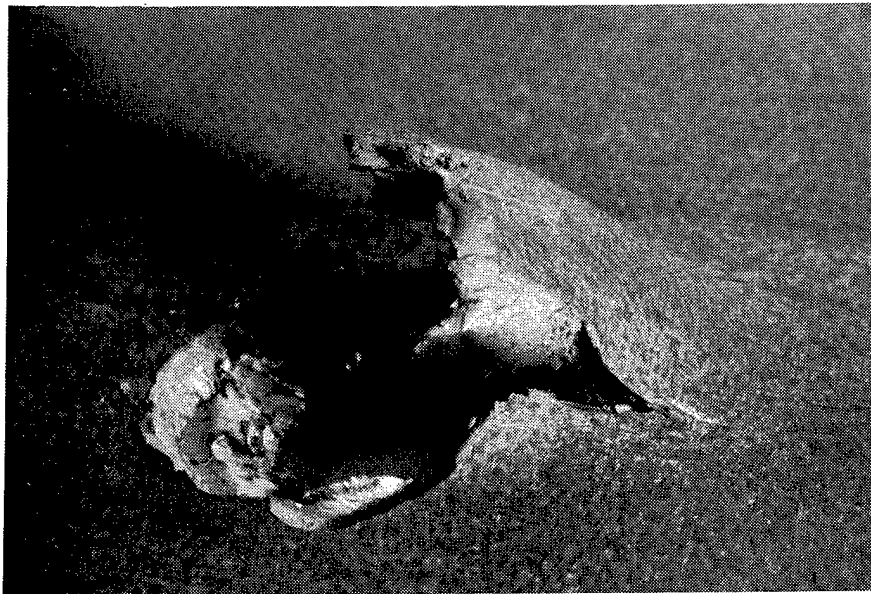
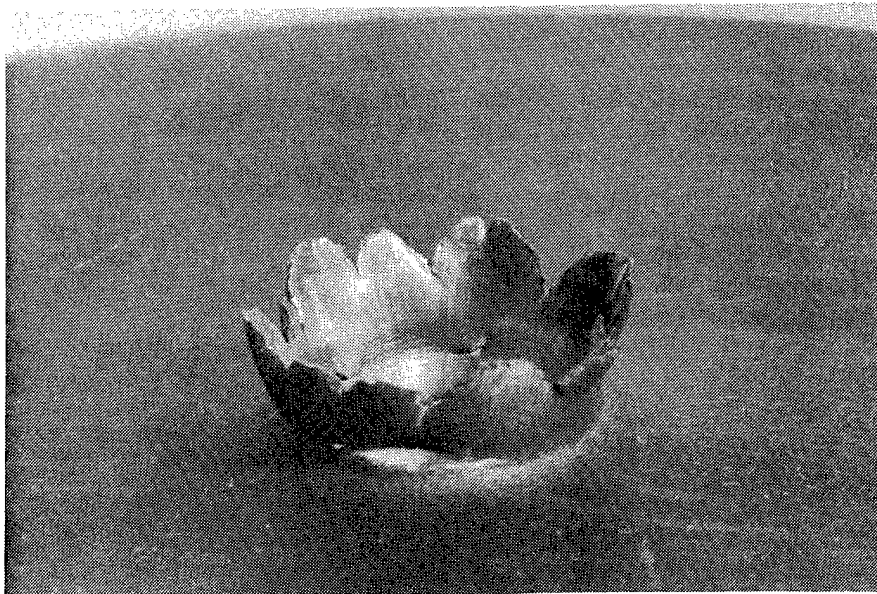


FIGURE 52. Distal Side of a 6.35-mm-Thick Steel Plate After Oblique Perforation by a Cylindro-Conical Steel Projectile. (Run C-44.)



(a) Impact Side.



(b) Distal Side.

FIGURE 53. Impact and Distal Sides of a 3.175-mm-Thick Mild Steel Plate After Oblique Perforation by a Cylindro-Conical Steel Projectile. (Run C-39.)

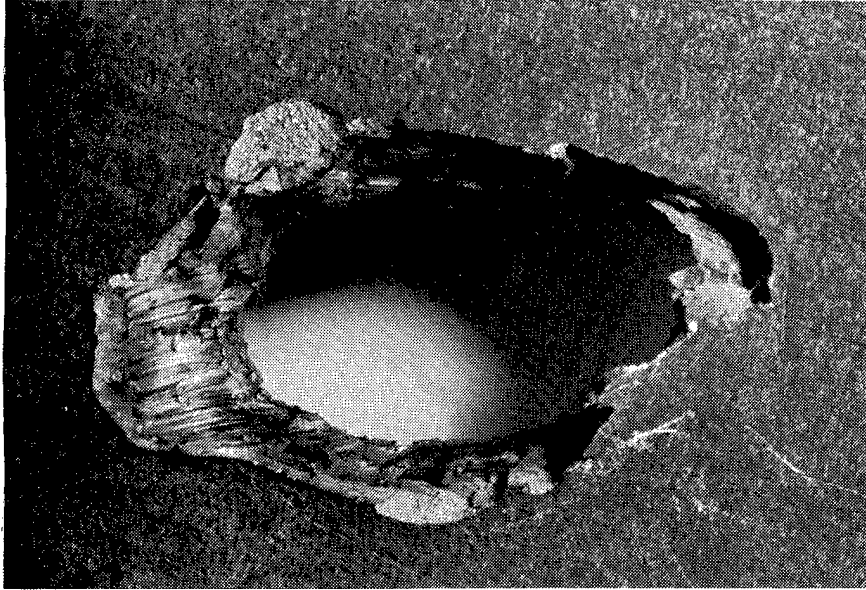


FIGURE 54. Distal Side of a 6.35-mm-Thick Steel Target After Oblique Perforation by a Cylindro-Conical Steel Projectile. (Run C-93.)

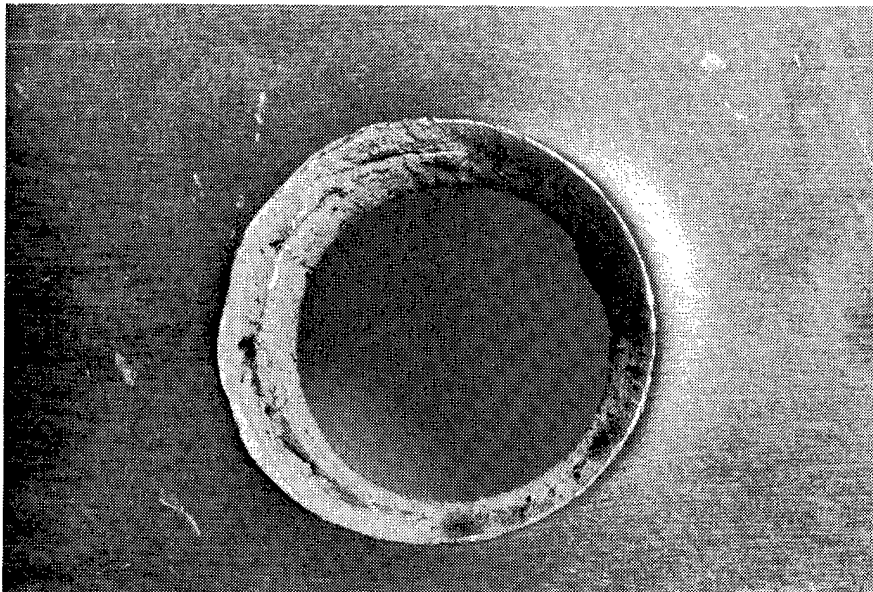


FIGURE 55. Distal Side of a 6.35-mm-Thick Aluminum Target After Normal Perforation by a Blunt Steel Projectile. (Run C-49.)

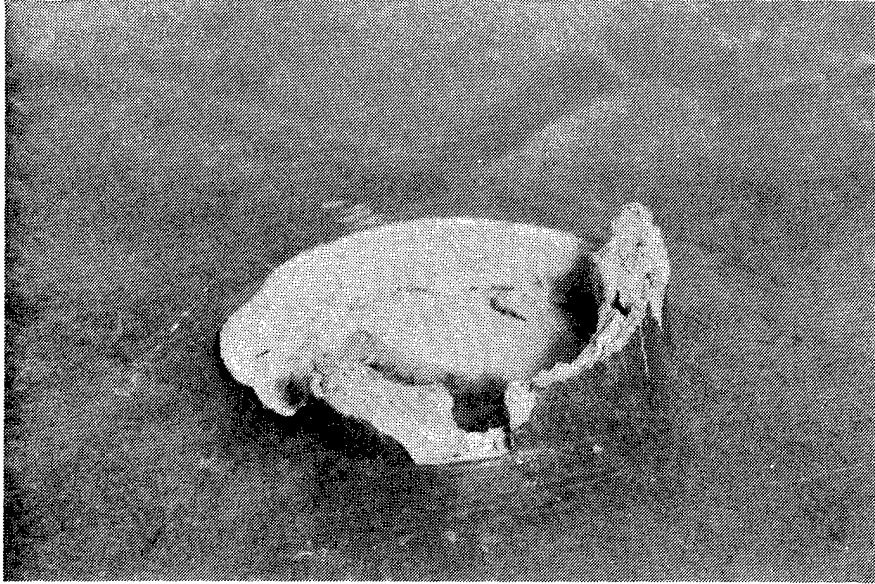


FIGURE 56. Distal Side of a 12.7-mm-Thick Aluminum Target After Normal Perforation by a Blunt Steel Projectile. (Run C-116.)

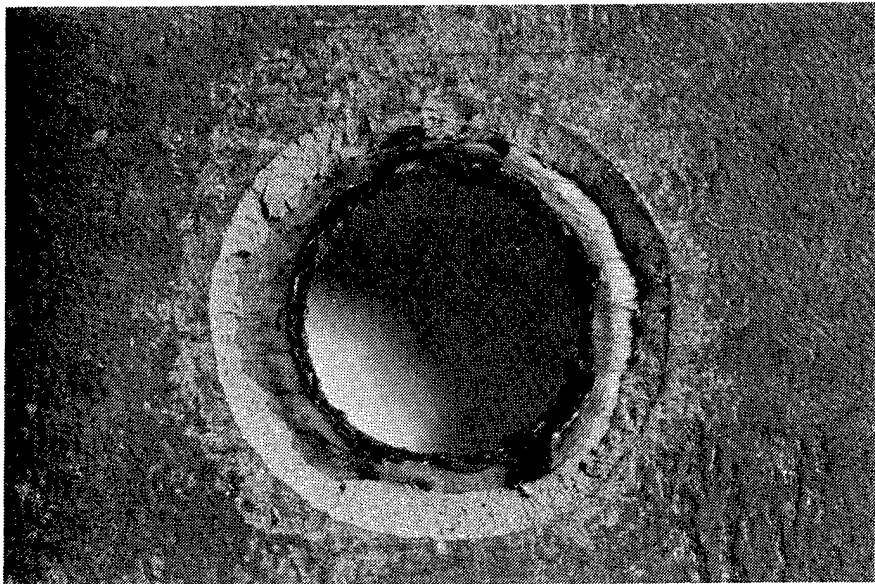


FIGURE 57. Distal Side of a 6.35-mm-Thick Steel Target Struck by a Blunt Steel Projectile. (Run C-118.)

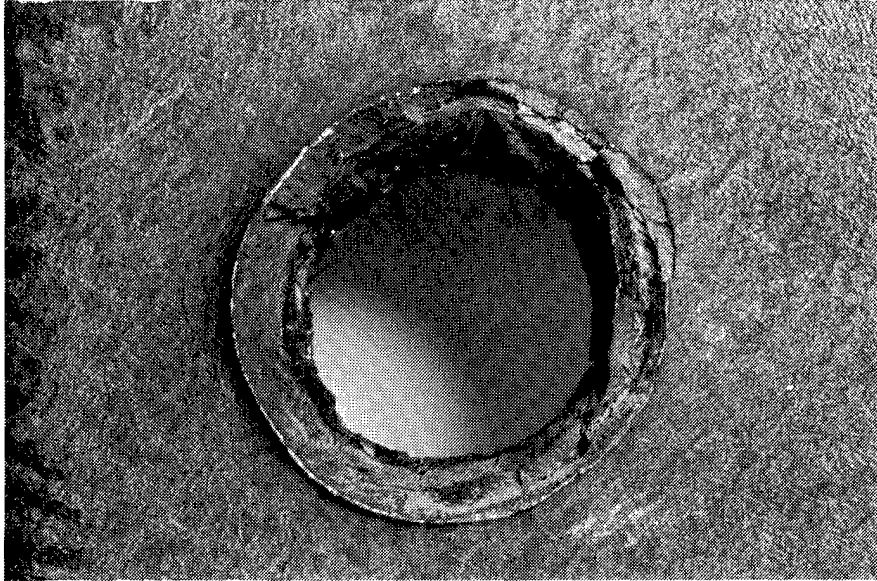


FIGURE 58. Distal Side of a 12.7-mm-Thick Mild Steel Target After Normal Perforation by a Blunt Steel Projectile. (Run C-115.)

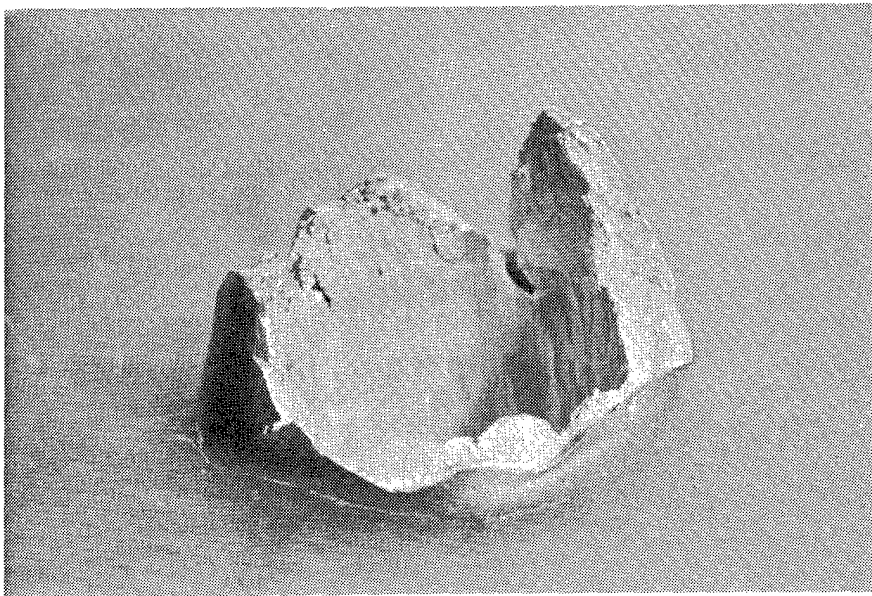
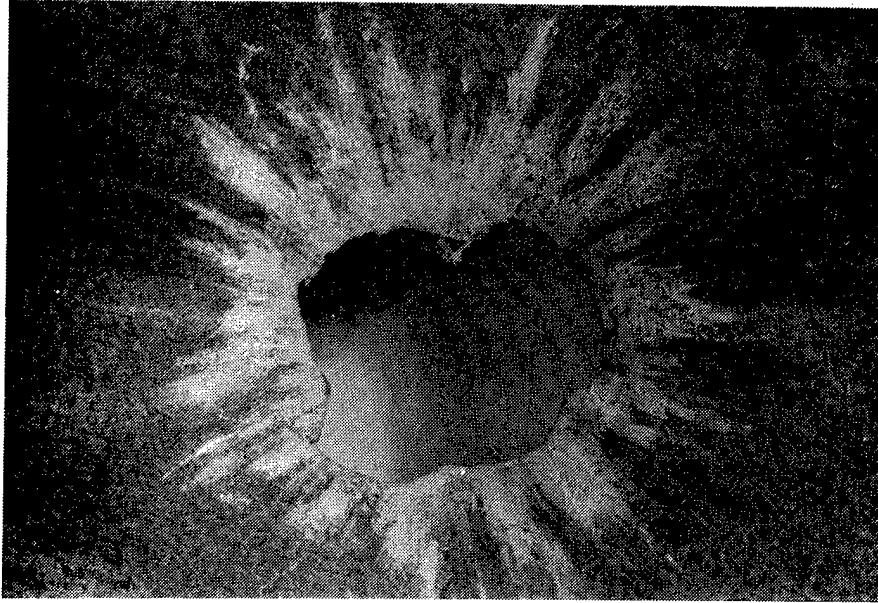
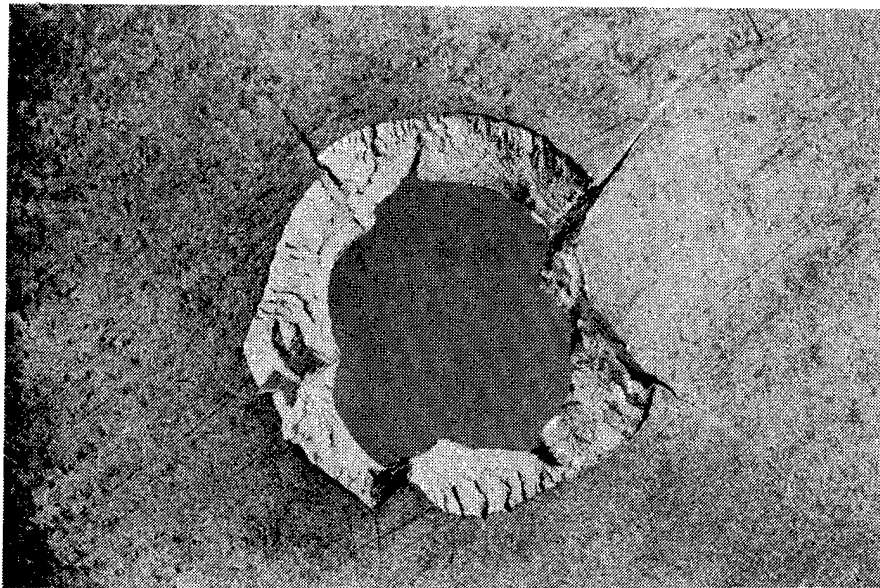


FIGURE 59. Distal Side of a 12.7-mm-Thick Aluminum Target After Normal Perforation by a Blunt Aluminum Projectile. (Run C-119.)



(a) Impact Side.



(b) Distal Side.

FIGURE 60. Impact and Distal Sides of a 6.35-mm-Thick Steel Target After Normal Perforation by a Blunt Aluminum Projectile. (Run C-104.)

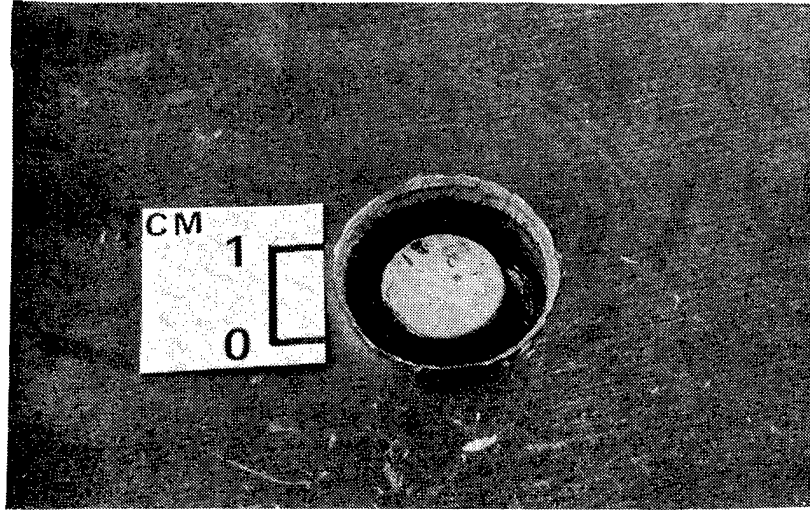
targets perforated by the conical striker with increase in target resistance, initial velocity, and angle of incidence; the same pattern is observed as previously described.

Perforation of two sizes of aluminum targets shown in Figures 55 and 56 was caused by normal impact at high velocity of a blunt steel projectile that remained intact. For the same conditions involving steel targets, the projectile shattered, as shown in Figures 57 and 58. The crater edges of the steel targets on both impact and distal sides are somewhat more regular than for the case of aluminum. Finally the use of an aluminum projectile with a blunt front produced a severe crater distortion, as shown for two of the higher velocities employed in Figures 59 and 60. Concomitantly, the projectile is successively shortened and mushroomed as the velocity increases. This can be seen in Figure 61a which shows severely mushroomed aluminum projectile embedded in a thick aluminum target. A combination of plugging and petalling processes resulted from this particular high-speed impact, as seen in Figure 61b.

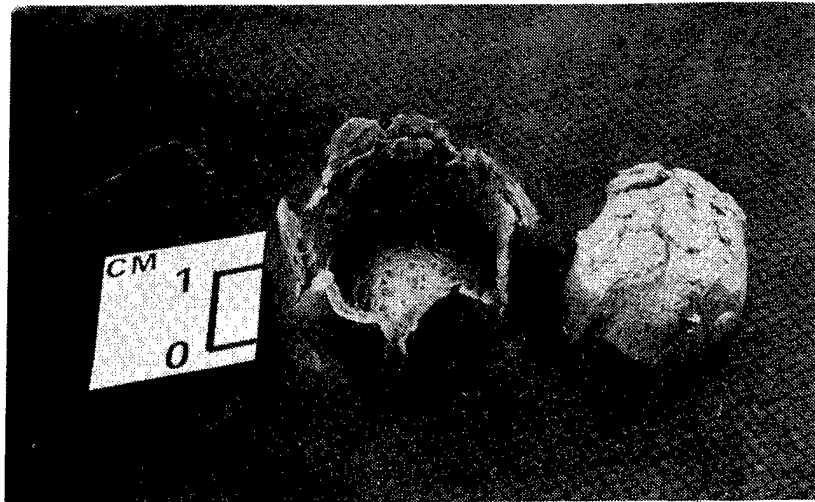
The perforation geometry becomes more oval as the obliquity increases. The major diameter of selected runs, incorporated in Table 2, ranges from 17.8 to 28 mm for angles of incidence upward of 30 degrees. Exceptionally, Run C-121 exhibits a major diameter of 33 mm, resulting in an aspect ratio of 2.6 for the elliptical perforation produced by this 40-degree shot.

Central contours of the distal surface of some representative aluminum targets were obtained by means of the profilometer and are shown in Figure 62a through c. The difference in petal height is graphically illustrated for impact at obliquity in the first two of these diagrams, while the essentially symmetric pattern for normal impact is portrayed in diagram 62c. Figure 62d shows the successively larger deformation of an aluminum plate as the impact velocity of the cylindro-conical striker is increased, with the highest impact speed generating significant cracks detectable even in this crude fashion.

Target damage for some of the special tests is shown in Figures 63 through 66. The first of these photographs depicts the damage on the distal side of 3.175-mm-thick aluminum targets as the velocity of the sharp-pointed striker striking at normal incidence is successively decreased. An anomaly is found in part 63b of this composite, which shows substantially more damage than that created at slightly higher collision speeds. The explanation for this can only be surmised, but may be due to local inhomogeneities (or weaknesses) in the target, experimental errors in initial velocity determination, or slight deviations from normality in the case of part a of Figure 63. Figure 64 shows both sides of the plate for



(a) Impact Side.



(b) Distal Side.

FIGURE 61. Impact and Distal Sides of a 19.05-mm-Thick Aluminum Target After Normal Impact by a Blunt Aluminum Projectile. (Run C-111.)

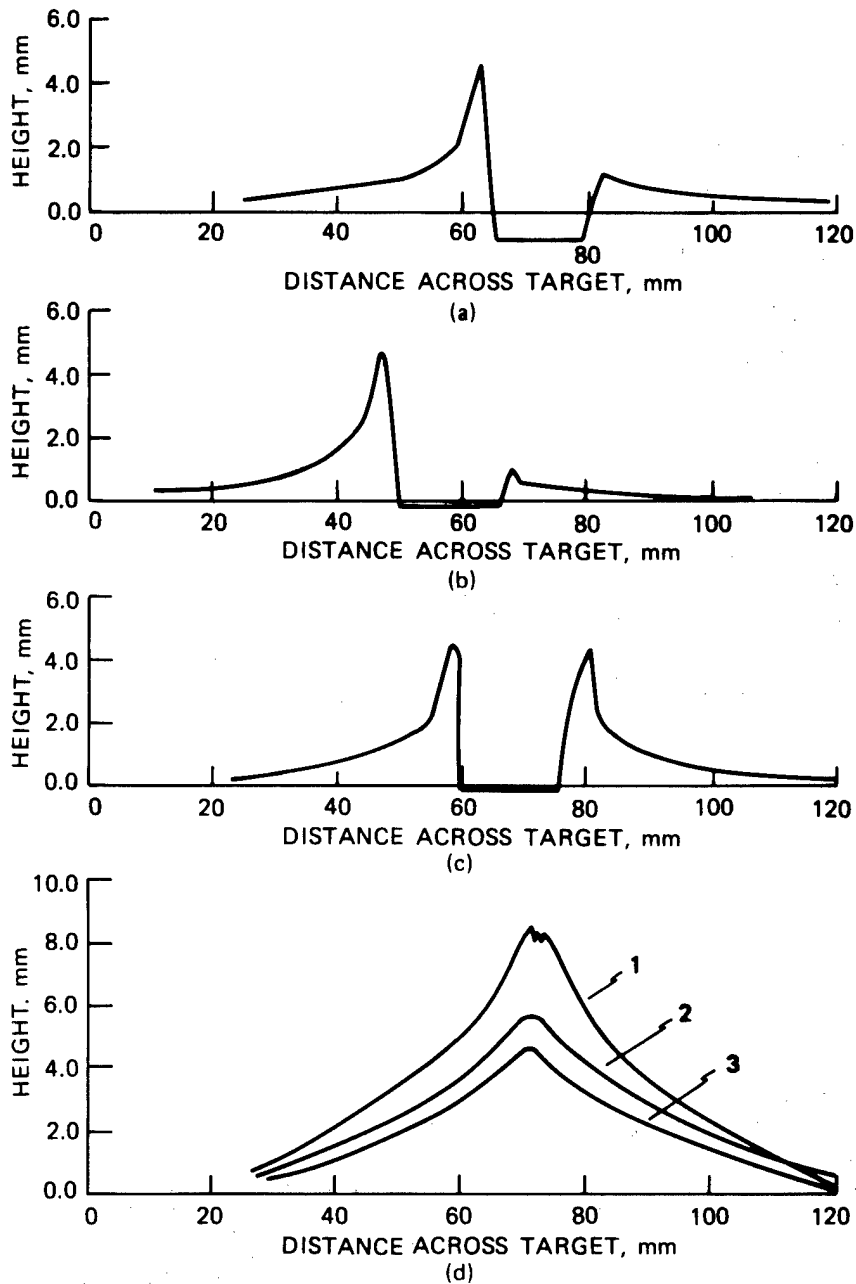
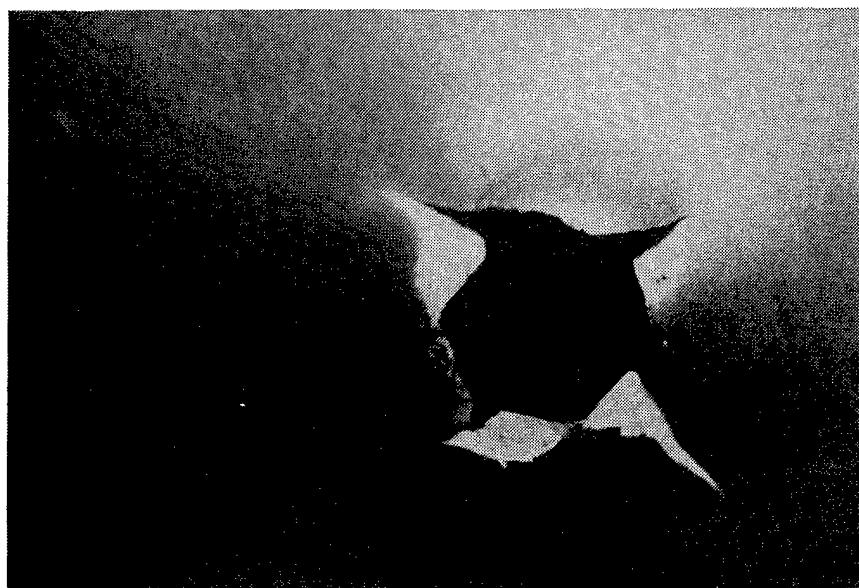


FIGURE 62. Central Contours of Perforated or Deformed Targets.
 (a) 6.35-mm-thick aluminum target struck at 30 degrees by cylindro-conical projectile at 930 m/s (Run C-79).
 (b) 3.175-mm-thick aluminum target struck at 40 Degrees by cylindro-conical projectile at 613 m/s (Run C-73).
 (c) 6.35-mm-thick aluminum target struck normally by blunt aluminum projectile at 918 m/s (Run C-105).
 (d) 3.175-mm-thick aluminum targets struck normally by cylindro-conical projectile: (1) initial velocity 61 m/s (Run D-7); (2) initial velocity 46 m/s (Run D-9); (3) initial velocity 42 m/s (Run D-10).

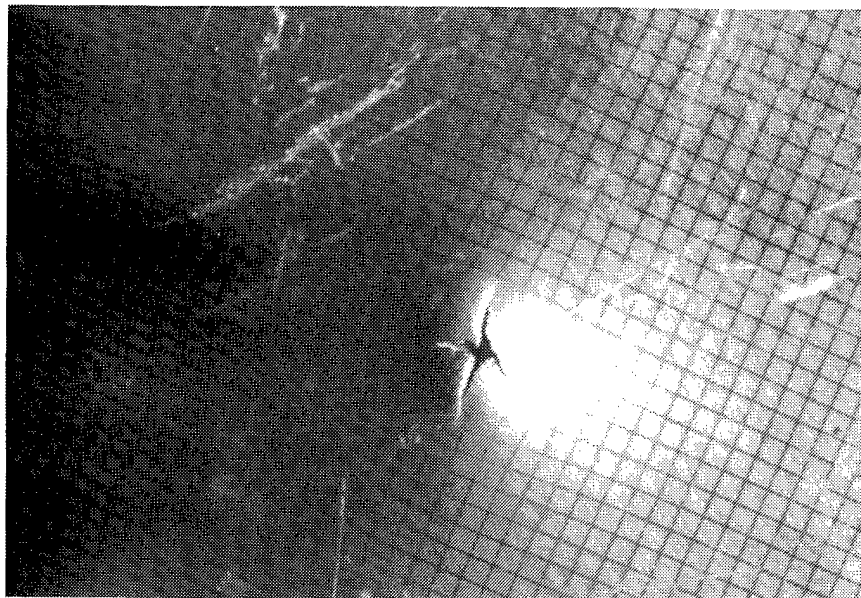


(a) $v_0 = 90.2$ m/s (Run D-5).

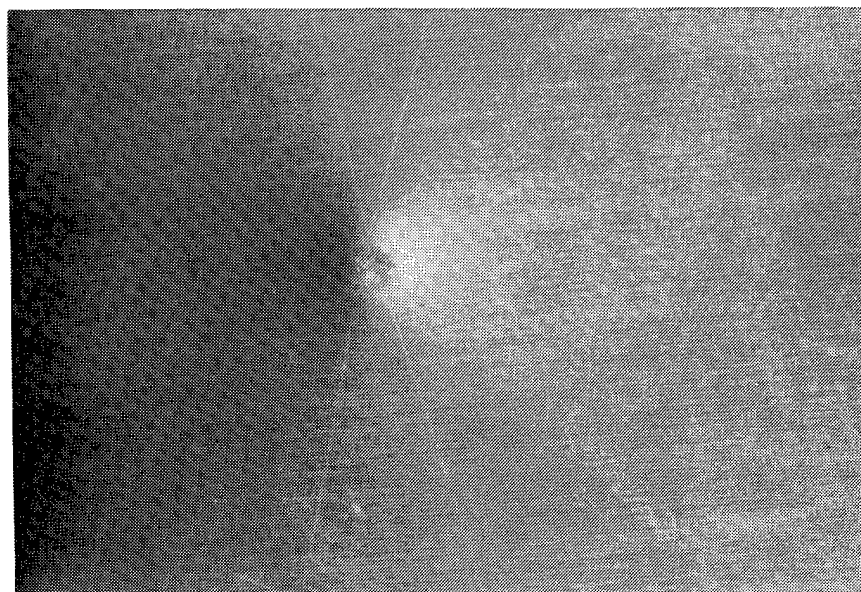


(b) $v_0 = 87.8$ m/s (Run D-6).

FIGURE 63. Distal Side of a 3.175-mm-Thick Aluminum Target for Various Normal Impacts by a Cylindro-Conical Hard Steel Projectile.

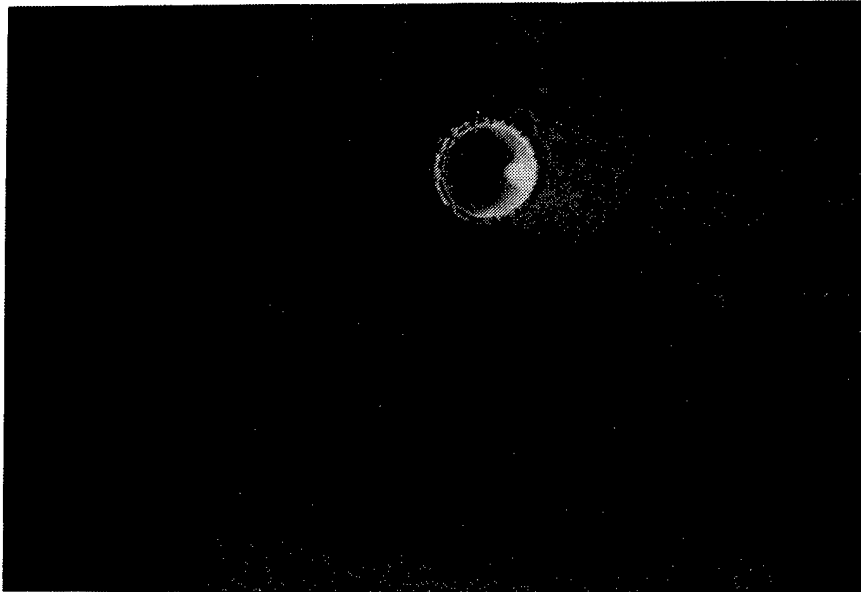


(c) $v_0 = 60.7$ m/s (Run D-7).

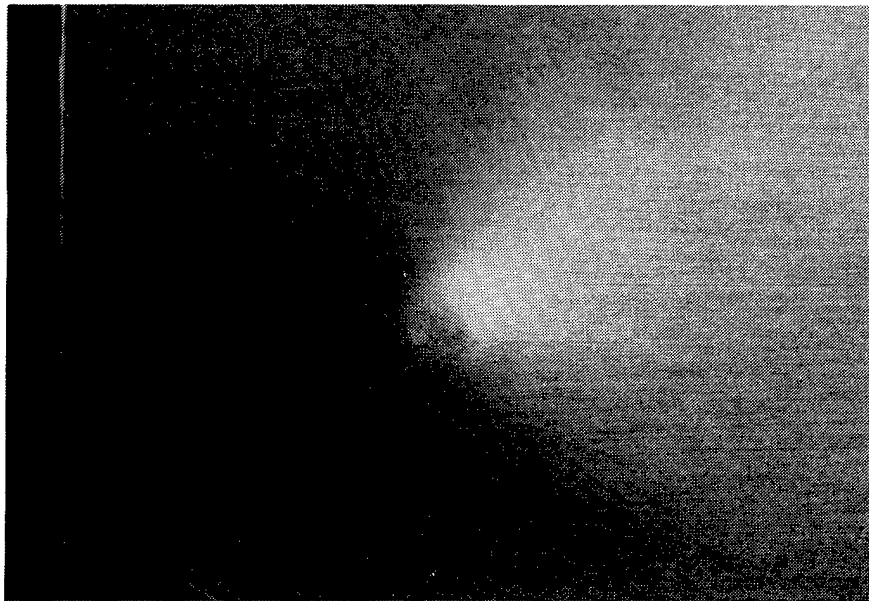


(d) $v_0 = 45.7$ m/s (Run D-9).

FIGURE 63. (Contd.)



(a) Impact Side.

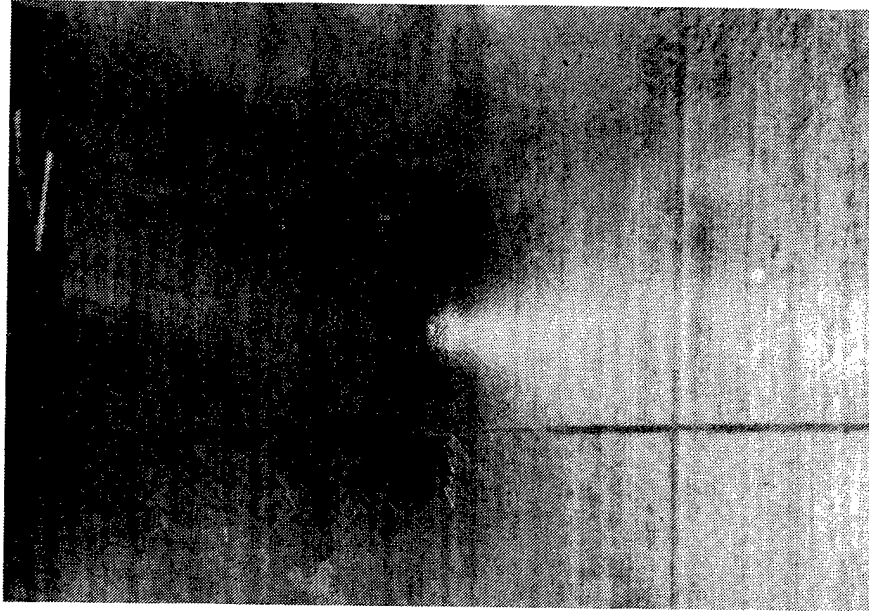


(b) Distal Side.

FIGURE 64. Impact and Distal Sides of a 3.175-mm-Thick Aluminum Target Due to Normal Impact by a Cylindro-Conical Steel Projectile. (Run D-8.)



FIGURE 65. Distal Side of a 3.175-mm-Thick Aluminum Target Due to Normal Impact by a Hemispherically Tipped Projectile. (Run D-30.)



(a) $v_0 = 19.4$ m/s (Run D-31).



(b) $v_0 = 27.2$ m/s (Run D-32).

FIGURE 66. Distal Side of 1.78-mm-Thick Aluminum Targets After Normal Impact by a Cylindro-Conical Projectile.

an impact that just barely produces surface cracks on the distal face; the impact side exhibits the typical series of regular small rectangular petals composed of the metal removed by the indentation also noted in the vast majority of similar collision situations. The hemispherical bulge and circumferential shearing discontinuity of a cap that would be separated at slightly higher velocities, produced by a hemispherically tipped projectile striking normally at substantially higher speeds than in the case of Figures 63 and 64, is clearly shown in Figure 65. This configuration is identical to those cited in Reference 8 and dramatically illustrates the higher perforation efficiency of a sharp-pointed bullet in the vicinity of the ballistic limit. Figure 66 shows incipient and actual cracking in a similar set of impacts on a thinner aluminum plate. A novel feature of this group of figures is the presence of a bulge with a circular circumference in terminal configurations representing incipient petal formation; this hemispherical contour disappears at higher impact speeds for both sharp and blunt projectiles striking at normal incidence when either petal formation or plugging has reached a stage of maturity.

At lower velocities achievable with the pneumatic gun, plugs were produced only by the impact of blunt projectiles. The mass of the buttons separated in the ballistic limit determinations listed in Table 3 was of the order of 0.9 to 1.0 g. At the higher velocities of the powder gun, plugs were also generated by cylindro-conical projectiles. Table 4 summarizes both projectile and plug data for certain selected high-speed runs. The mass of the recovered central portion of the hole, or "plug," does not usually correspond to the total mass of the target material removed. Rings and small petals spalled from the distal side of the target that could most frequently not be recovered. At the higher velocities, petals generated by cylindro-conical projectiles not infrequently separated from the pierced target. At these speeds, the blunt hard-steel projectiles burst frequently into fragments and also caused fragmentation of the harder targets in a number of instances. The blunt aluminum projectiles shortened and mushroomed under all impact conditions.

Figures 67 through 72 are photographs of the projectiles, plugs, and a few other target components; Table 4 contains associated information. These data may be valuable for purposes of comparison with possible future analytical predictions of penetration involving both hard, brittle, or deformable projectiles against targets of this type, both at normal incidence and at obliquity. No phenomenological model of cylindrical or cylindro-conical penetration or perforation has been developed thus far other than for normal incidence.

TABLE 4. Selected Plug Data.

Run No.	Projectile dimensions			Projectile mass, g	Plug dimensions		Plug mass, g	Comments
	Length, mm	Diameter, mm	Minimum		Height, mm	Diameter, mm		
C-10	---	---	---	---	---	---	3.8	Oval shaped plug.
C-27	---	---	---	---	6.56	14.42	2.6	
C-30	---	---	---	---	---	18.94	2.7	
C-47	---	---	---	---	---	---	5.9	
C-96	35.80	14.55	14.55	---	---	---	5.6	Three peripheral target pieces of total mass 2.0 g recovered
C-99	32.28	17.44	12.56	---	6.51	14.40	---	
C-100	30.82	16.06	12.42	---	---	---	---	
C-101	---	---	---	5.9*	---	---	22.1*	
C-102	26.36	17.06	15.70	13.0	9.11	14.93	2.6	Peripheral target piece of mass 7.3 g recovered
C-103	21.18	19.12	11.78	11.1	---	---	---	
C-104	19.22*	15.70	---	---	---	---	7.6	
C-105	31.28	14.93	---	---	---	---	---	
C-106	37.35	12.60	12.60	36.6	6.40	13.36	2.1	Base of projectile curved. Oval shaped plug.
C-107	37.40	12.70	12.70	36.7	12.23	10.78	2.7	
C-108	37.53	12.60	12.60	36.3	12.50	16.83	3.6	
C-111	16.90	20.66	12.76	10.9	13.90	17.74	5.9	
C-112	---	---	---	21.3	---	19.56	---	Projectile in five pieces
C-113	37.22	12.62	12.62	36.5	8.73	12.78	2.2	
C-114	37.78#	---	---	29.9*	7.64	14.49	3.7	
C-115	---	---	---	21.4*	---	---	2.6	
C-116	36.78	13.32	12.56	36.4	6.14	13.38	1.3	Total 4-piece mass removed 3.4 g
C-119	24.52	20.05	20.05	15.2	11.74	11.76	5.2	
C-120	---	---	---	---	9.18	21.38	16.0	
C-123	34.90	14.42	12.52	14.2	6.50	13.94	2.0	
C-125	37.18	13.18	12.66	36.4	7.18	12.20	1.4	Recovered part may be striker together with target

*As recovered
#Broken

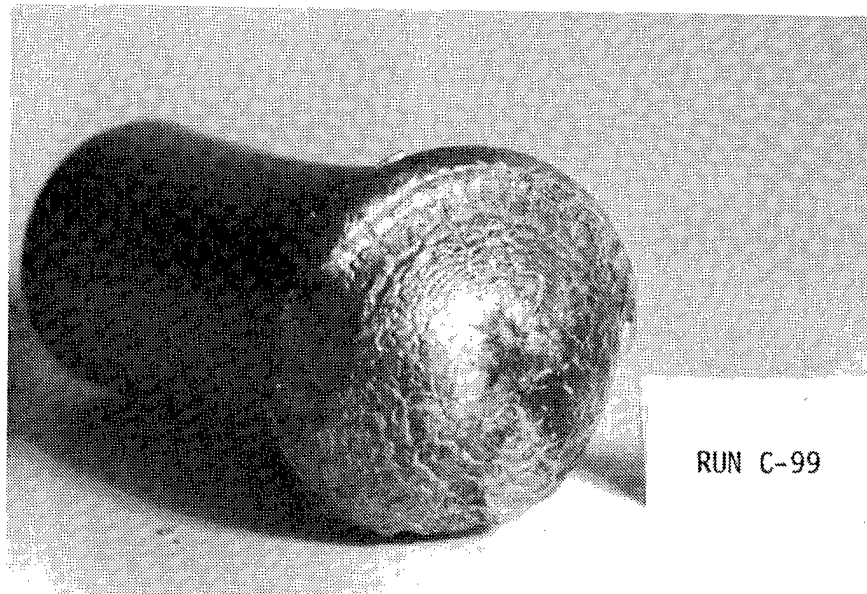
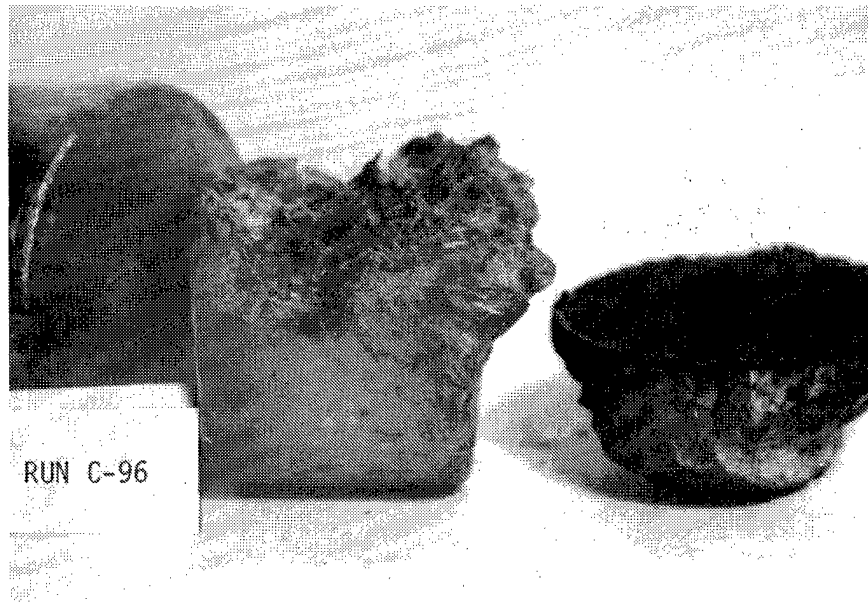


FIGURE 67. Projectile and Plug Photographs of Runs C-96, C-99, and C-100.

NWC TP 6479

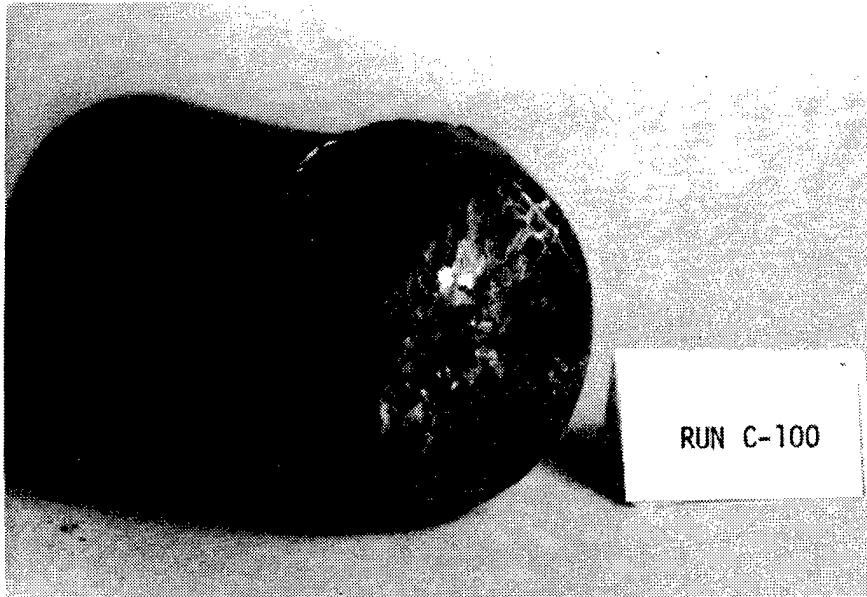


FIGURE 67. (Contd.)

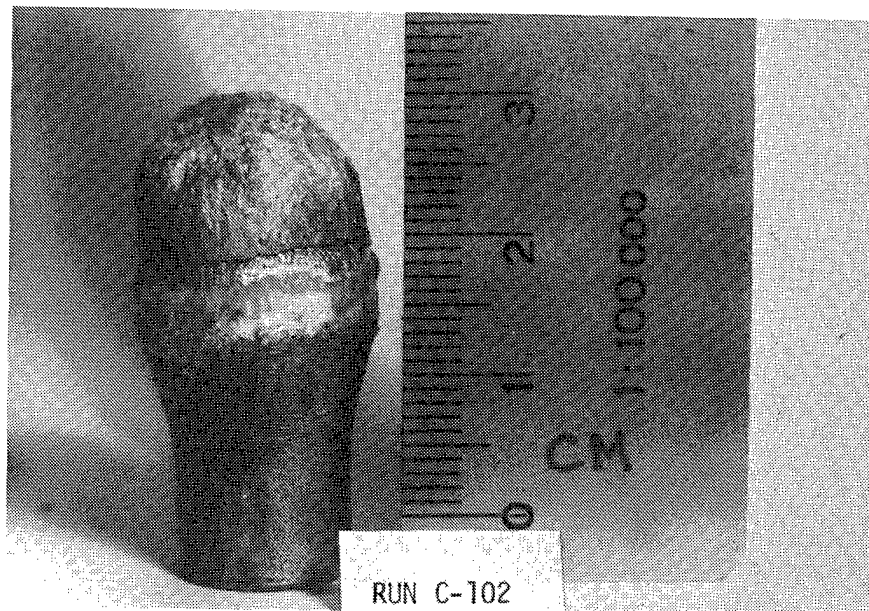
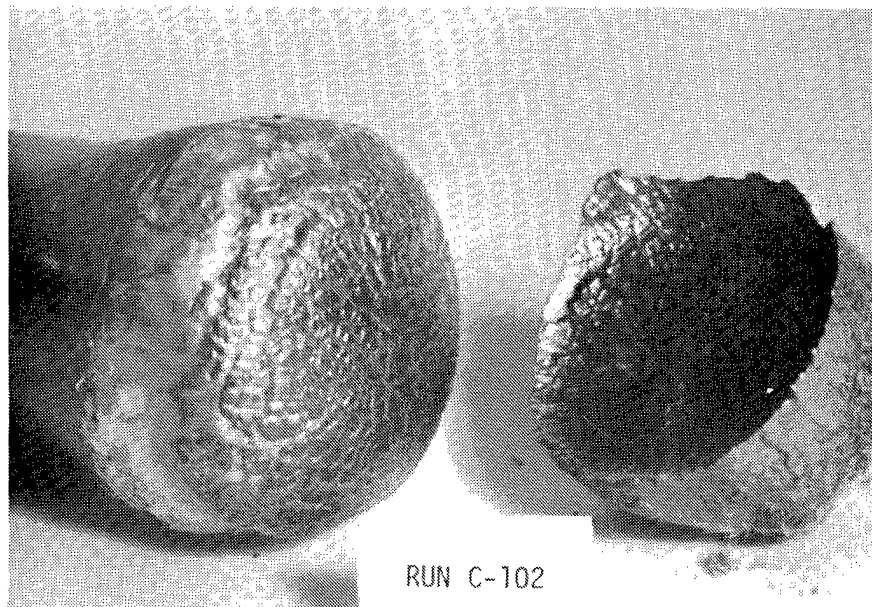


FIGURE 68. Projectile, Plug, and Peripheral Target Fragment Photographs of Runs C-102 and C-103.

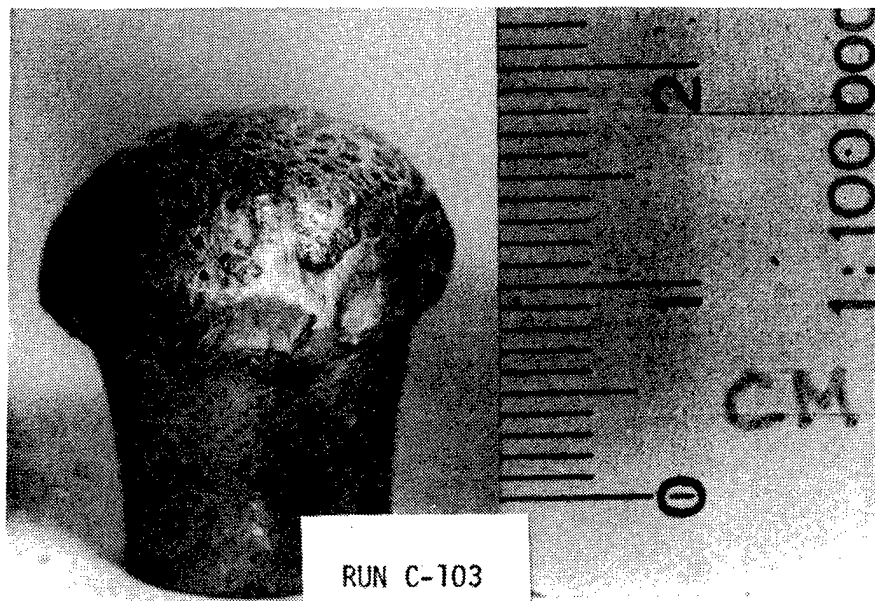
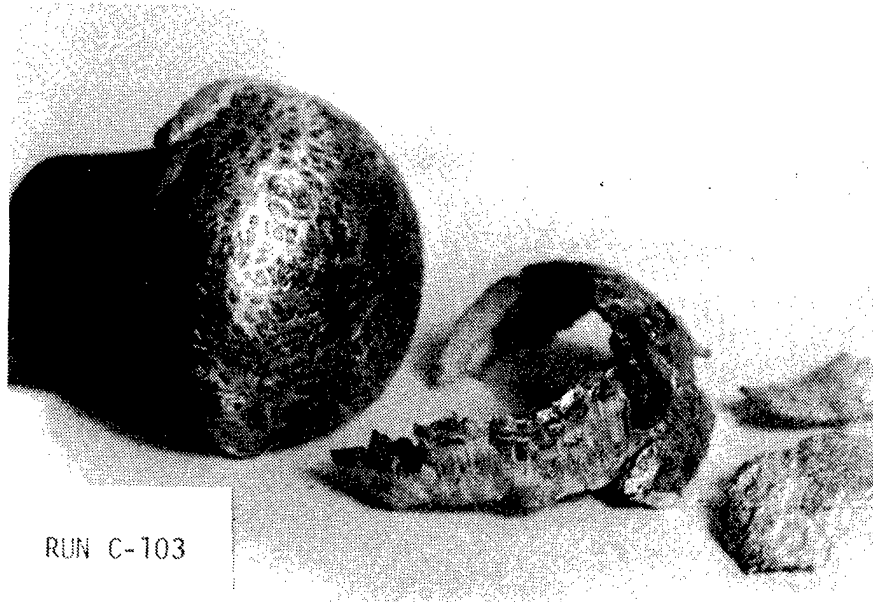


FIGURE 68. (Contd.)

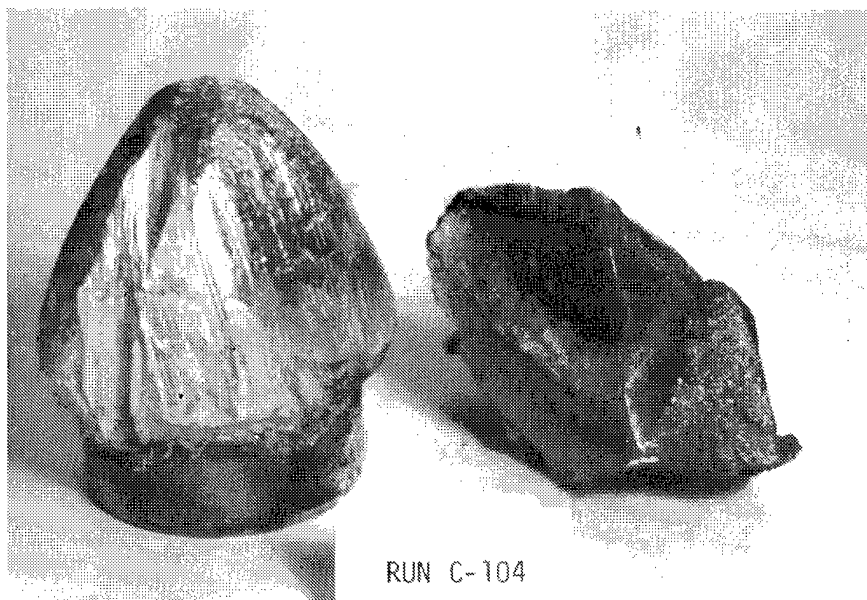
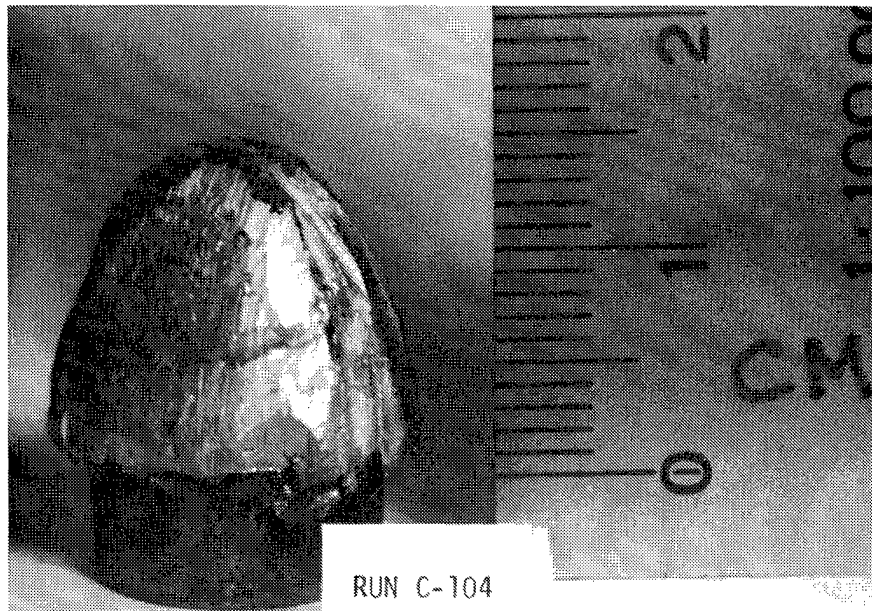


FIGURE 69. Projectile and Plug Photographs for Runs C-104, C-105, and C-106.

NWC TP 6479

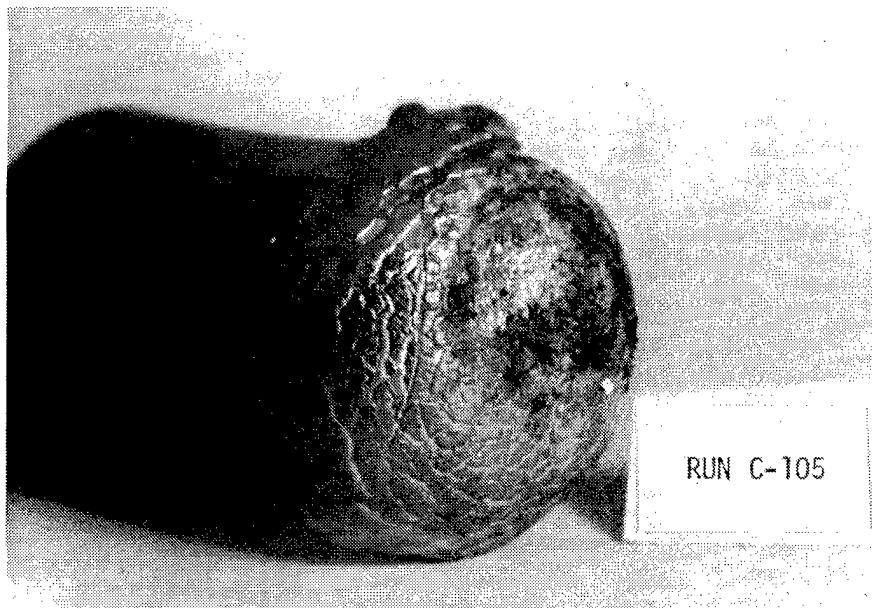


FIGURE 69. (Contd.)

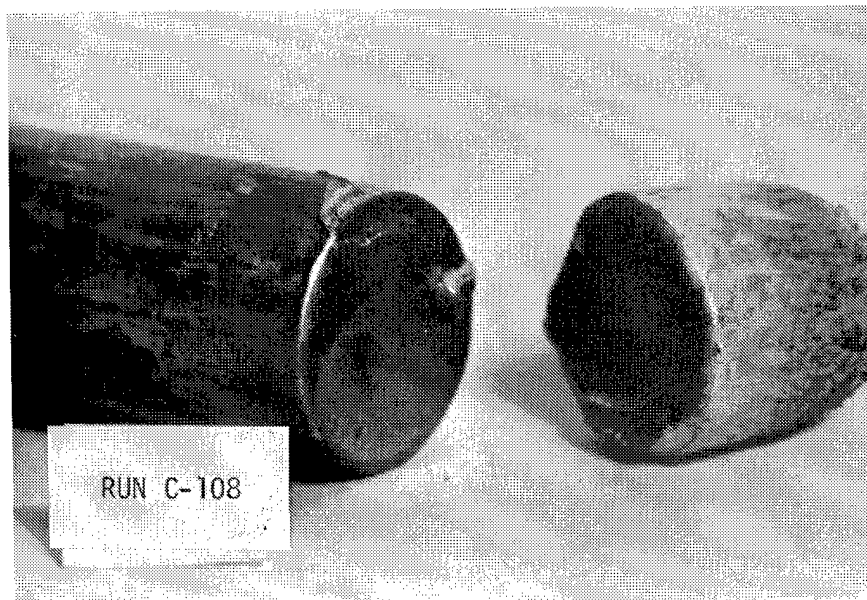
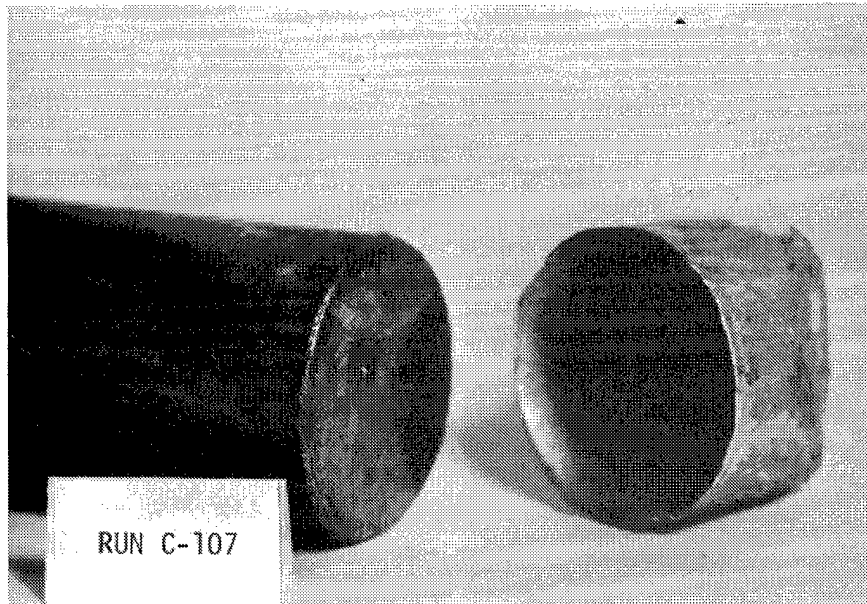


FIGURE 70. Projectile and Plug Photographs for Runs C-107, C-108, C-112, and C-113.

NWC TP 6479

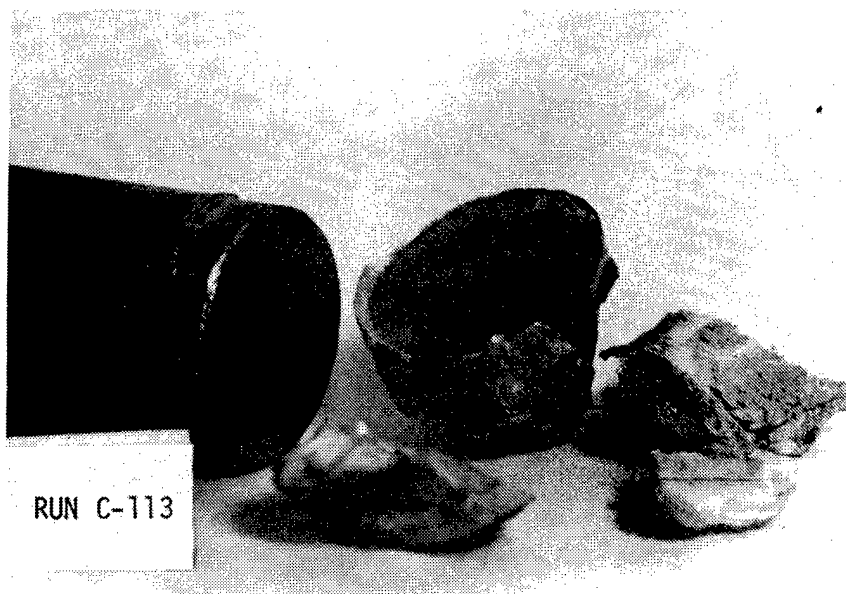
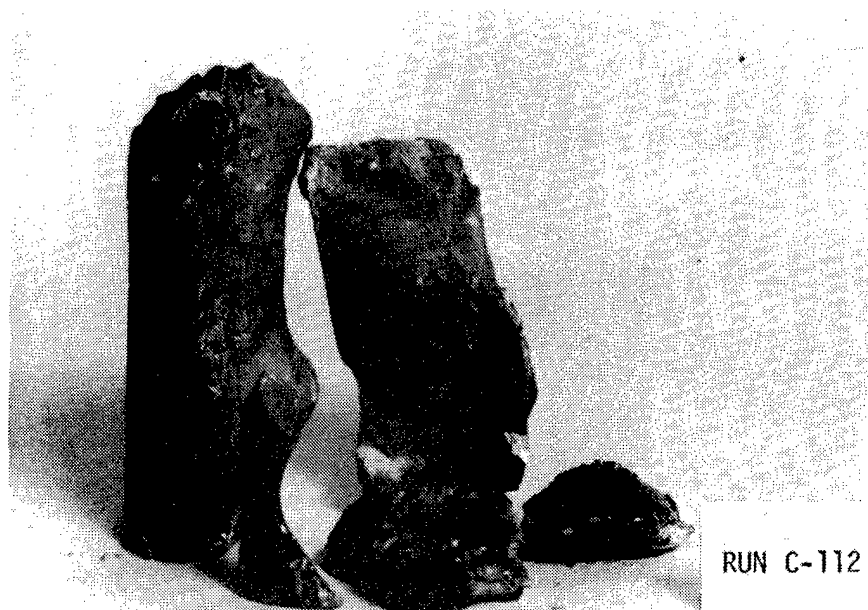


FIGURE 70. (Contd.)



FIGURE 71. Projectile and Plug Photographs for Runs C-115, C-116, C-118, and C-120.

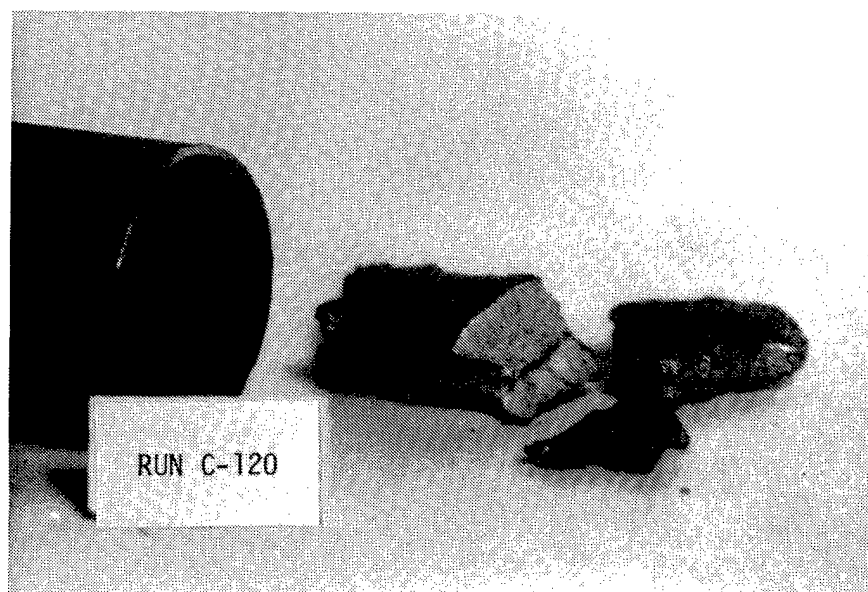
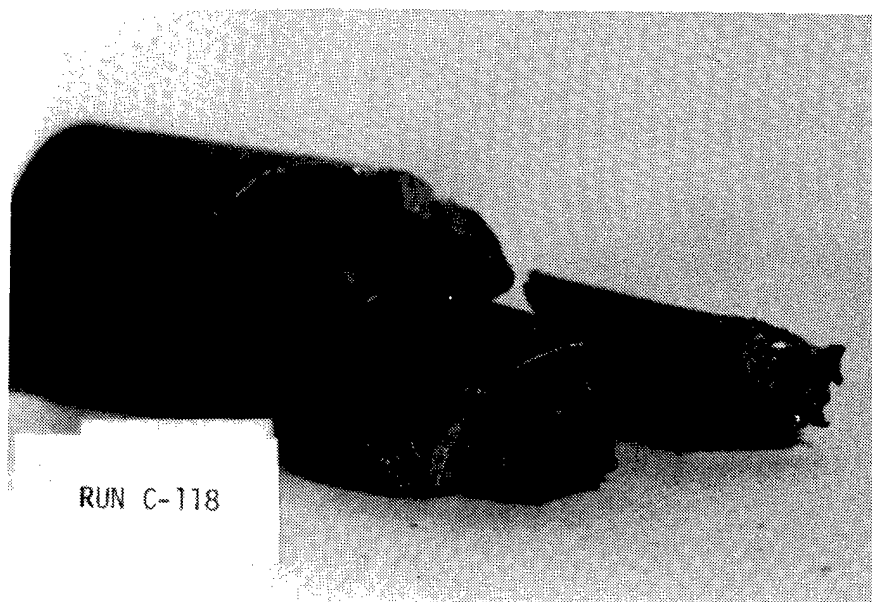


FIGURE 71. (Contd.)

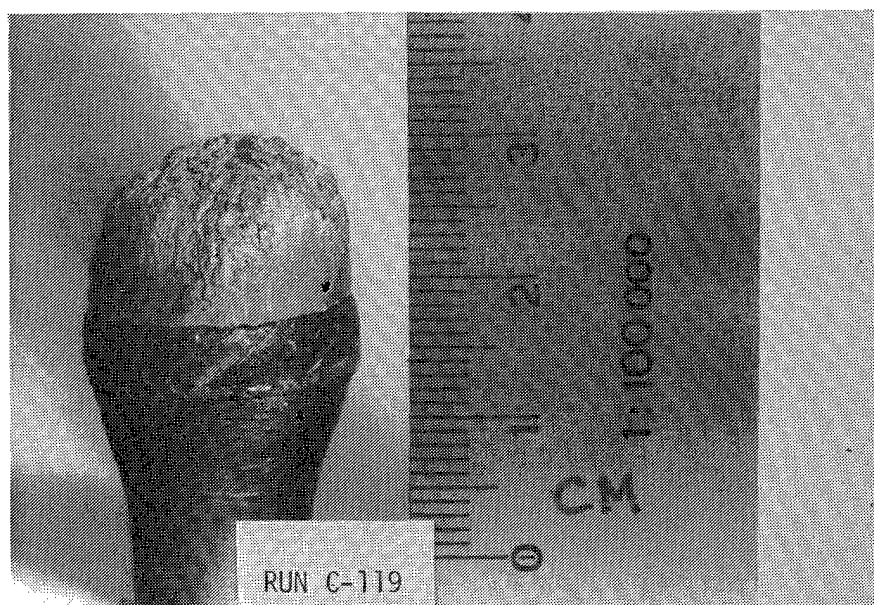
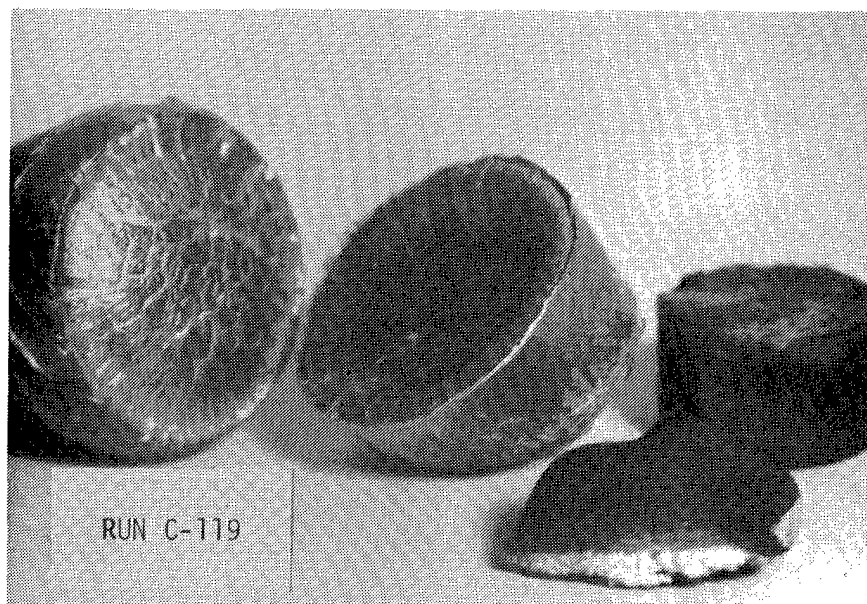


FIGURE 72. Projectile and Plug Photographs for Runs C-119 and C-121.

NWC TP 6479

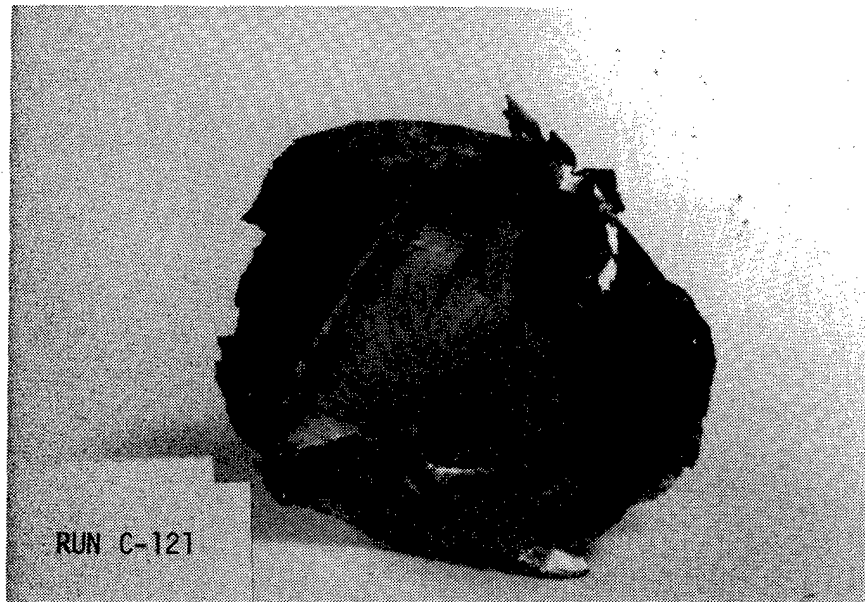


FIGURE 72. (Contd.)

Two force histories measured with the special projectile are presented in Figures 73 and 74 for the shank embedment and complete perforation, respectively, of a 60-degree conically headed steel projectile striking a 3.175-mm-thick 2024-0 aluminum target at normal incidence. The curves are nearly identical in shape and peak value, differing only slightly in overall duration and the extent of the inflection during the rising portion of the curve; the initial velocities also differ by only about 4 percent. The process up to the inflection point represents the penetration process up to the onset of fracture, consisting of striker indentation and target deflection due to bending and shear. The subsequent increase in force to the peak value is due to the enlargement of the initial protrusion accompanied by crack extension and further bulk deformation of the target. The reduction in the force occurs when the resistance to the motion of projectile decreases, most likely beginning at the instant of the emergence of the shank. This period is somewhat shorter than the rising portion, approximately 40 percent of the total impact duration.

A comparison of these force curves with that generated by the perforation well above the ballistic limit of a 1.27-mm-thick 2024-0 aluminum plate by a 39.4 g hemispherically-nosed cylindrical steel projectile of 12.7-mm-diameter shows major similarities in the shape, but some differences (Reference 8). The former data were obtained under conditions of plugging, whereas the present information pertains to processes involving crack propagation and petal bending. In consequence, a second knee occurs in the descending portion of the force curve for the hemispherically nosed striker that is attributed to a small amount of additional plate deformation after initial separation of the plug from the target and projectile. Furthermore, the initial discontinuity during force ascent is attributable to the initiation of shearing of the plug instead of the present onset of cracking on the distal side. The rise time of this curve is approximately one-third of the overall duration.

Since the principal information obtained in this series of tests concerns the drop in velocity and change in direction of the projectile as the result of target impact, the errors to be expected in the data will be estimated. The initial velocity was determined both by the signals generated from the interruption of light beams traversing the terminal end of the gun barrel and from measurements of the projectile position in the photographic data. Agreement between these two modes was generally satisfactory, i.e., within 2 percent; however, in some instances, substantial differences were found. These can be attributed to (a) spurious early triggering of the photocells due to the advance of combustion products ahead of the projectile, (b) planar recording of a three-dimensional event, so that slight yaw would introduce a discrepancy, estimated at no

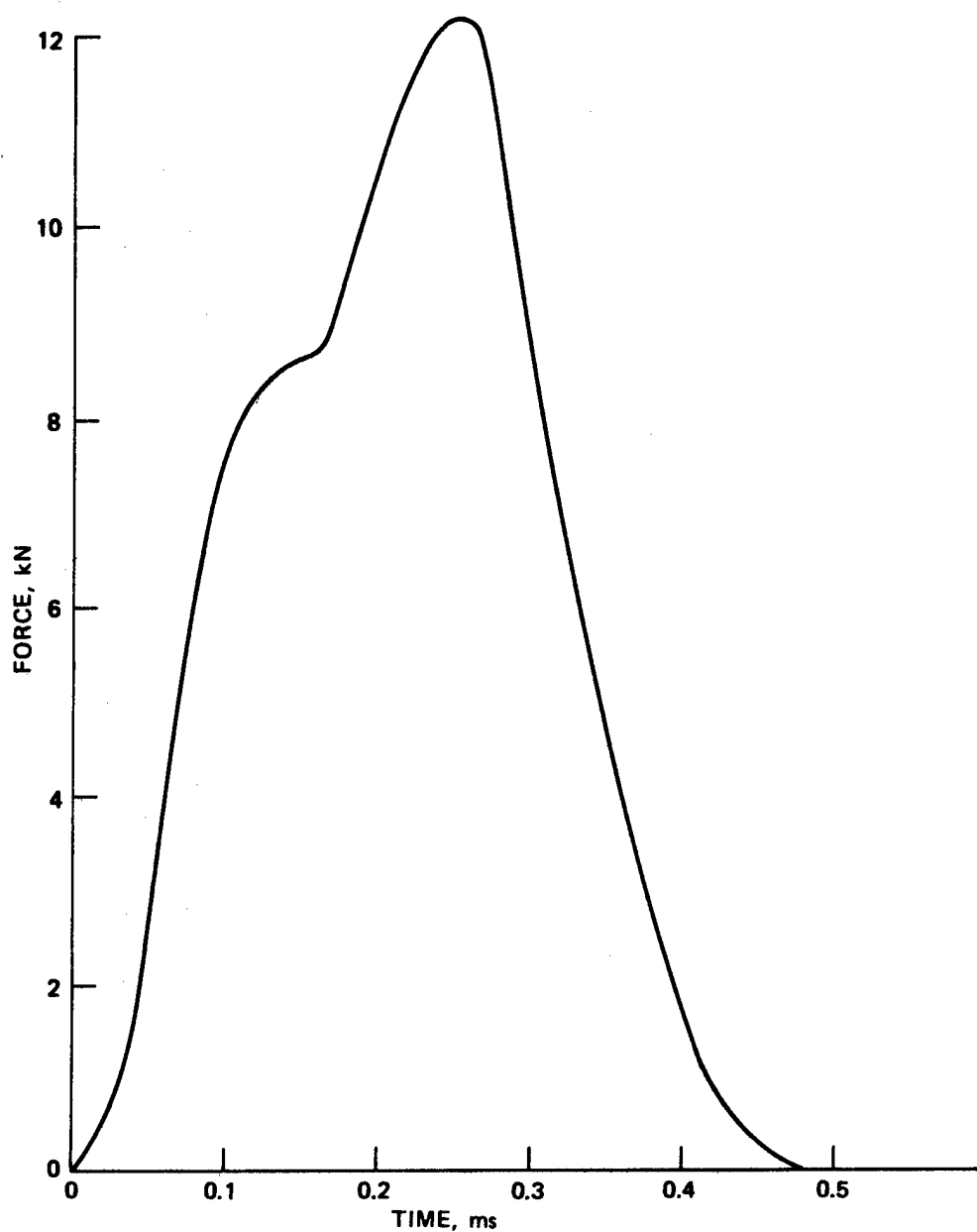


FIGURE 73. Force History, Normal Impact of 30.5-g, 12.7-mm-Diameter Hard-Steel Projectile on 3.175-mm-Thick 2024-0 Aluminum Target, Velocity 94.8 m/s. Result was embedment of shank.

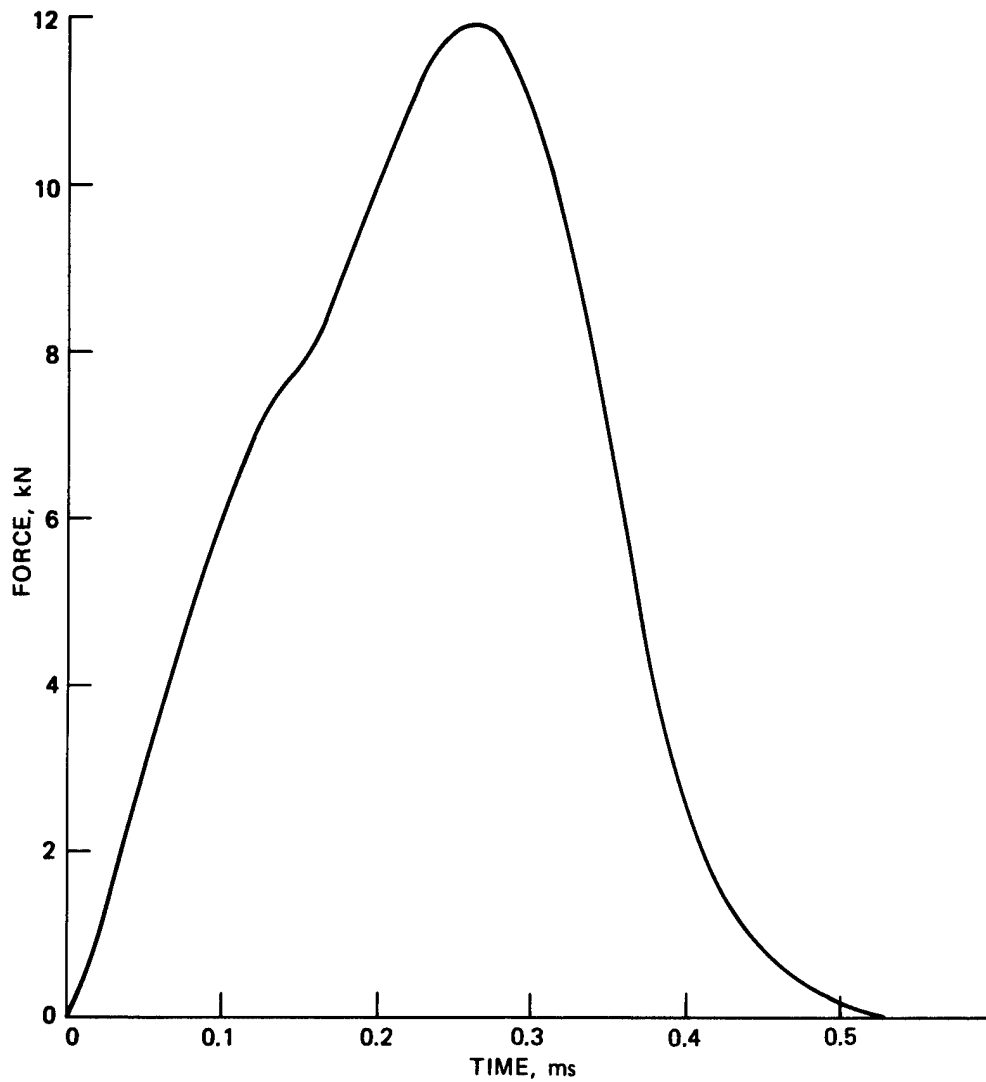


FIGURE 74. Force History, Normal Impact of 30.5-g, 12.7-mm-Diameter Hard-Steel Projectile on 3.175-mm-Thick 2024-0 Aluminum Target, Velocity 98.5 m/s. Result was complete perforation.

more than 5 percent, and (c) difficulties in the photographic results of identifying a common position reference for all pictures of a set, requiring some adjustments. The last two problems also apply to the evaluation of the terminal velocity. In consequence, the photographic results were utilized whenever a discrepancy was noted. In addition, there were alignment errors in the positioning of the target relative to the gun and camera and in measurement of the terminal trajectories from the witness papers. It is estimated that the maximum error in absolute quantities did not exceed 5 percent and was generally much better. However, parameters involving differences of quantities with nearly identical magnitude might evidence a substantially greater error. Hence caution should be utilized when examining the angular variation in the projectile trajectory and the non-dimensional velocity drop in the vicinity of the ballistic limit.

METALLURGICAL ANALYSIS OF TARGET IMPACT REGIONS

Target plates from six different tests (C-5, C-18, C-48, C-110, C-122, and C-124, Table 2) were subjected to metallurgical analysis. These particular tests were considered to be representative for normal incidence of the impact conditions encountered in this experimental program. This group included two impacts that resulted in embedment of the striker, one ricochet, two impacts each by conical-nosed steel, blunt steel, and blunt aluminum projectiles and impacts involving a range of projectile speeds (305-915 m/s) and against several different targets (6.35-mm-thick steel, 6.35-, 12.7-, and 19.05-mm-thick aluminum). Unfortunately, due to time constraints, only one oblique impact could be examined, but the one chosen was considered to be one of the more interesting in the group.

The vast majority of the impacts in the entire series resulted in the perforation of the target, and the recovery of ejected target material was thus only a secondary objective of the experiment. Consequently, a complete set of ejected target fragments was recovered only where residual (exit) projectile speeds were low or where target ejecta occurred in the form of one or, at the most, a few large plug fragments traveling at small angles to the original flight path. As a result, a metallurgical examination of the entire target zone affected by the impact could not be carried out for many shots involving target perforation. Instead, the failure patterns in the regions adjacent to the perforation hole were closely examined in these cases in an attempt to identify the probable failure processes in the central impact region.

The perforation of target plates by projectiles (particularly blunt or rounded ones) usually involves punching out a whole or

fragmented plug of target material (Reference 1). The formation and ejection of this plug result from shear failures that initiate along or near the boundary of the impact surface. During impact, these shear failures are often caused by the initiation and propagation of very narrow zones of intense plastic deformation within the target, typically 10-30 microns wide. These localized bands of deformation, termed concentrated or adiabatic shear bands (References 17-19), are the result of large temperature gradients that occur in bodies loaded at very high strain rates when the rate of local heat production by mechanical work exceeds the rate of dissipation. These temperature gradients result in isolated hot spots in the body where thermal softening of the material, yielding, and eventually failure can initiate. Once started, these tiny yield zones propagate outward in narrow bands along directions of maximum shear stress propelled by the same heating/softening/yielding sequence that continues to develop along the boundaries of the yielded zone. When fully formed, these zones become planes of weakness where fracturing can take place.

Among the six targets examined metallurgically, only the 6.35-mm high-carbon steel contained concentrated shear bands in the impact region, as shown in Figures 75 and 76. Based on the number of bands found in the wall adjacent to the perforation hole, it is highly probable that the plugging perforation process associated with the impact of a blunt cylinder resulted from the formation of and failure along concentrated shear bands. In this same target, additional material in the shape of a ring was also torn away around the edges of the distal side of the hole. The removal of this peripheral material involved delamination of the plate, a phenomenon termed "scabbing" (Reference 1), which occurs in metals and alloys that have been formed by rolling processes. This process tends to produce grain and impurity orientations that are retained in varying degrees after subsequent heat treating operations and result in a laminated material containing zones of weakness (Reference 20). Plate materials typically acquire planes of weakness parallel to the main surfaces. For the particular impact shown in Figure 75, shear displacements occurred along these planes in and around the impact area causing delamination of the material there. A ring-like piece of this delaminated material then became detached from the distal side by the impact process leaving a crystalline-appearing fracture surface along the outer periphery. Figure 77 shows a magnified view of the microstructure along the boundary of this fracture surface.

A few bands of concentrated shear were found in the same target material when struck by a conical-nosed projectile at a 30-degree angle of obliquity, as shown in Figures 78 and 79. Although these clearly did not dominate the fracture process in this situation, their presence demonstrates the susceptibility of this particular

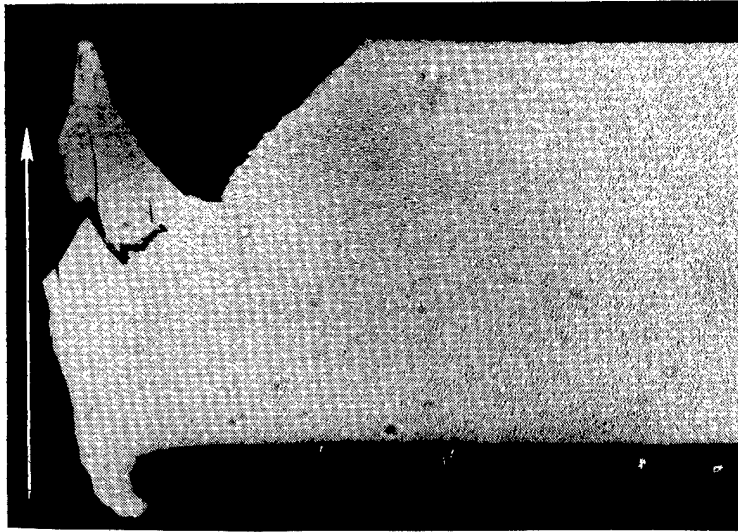


FIGURE 75. Section View of One Side of the Crater in a 6.35-mm Steel Target Perforated by a 12.7-mm Blunt-Ended Steel Cylinder Initially Traveling at 883 m/s. Penetration path shown by arrow. (Run C-48.)

target material to localized shear deformations. Target fractures in this instance appeared to take place largely by petal formation. Some delamination along one side of the perforation hole also occurred which involved both shear and tensile modes of separation, the latter dominating in this instance.

The remainder of the targets examined were annealed 2024 series aluminum. Two contained an embedded blunt aluminum projectile, shown in Figures 80 and 81, the second of which had mushroomed upon impact. The other two were perforated by hard-steel strikers, one blunt-nosed (Figure 82) and the other conical-tipped (Figure 83). All of these targets were characterized by the complete absence of concentrated shear bands around the impact region. Although the wall adjacent to the central impact zone in one target (Figure 82) appeared very similar to that seen in the steel target shown in Figure 75, shear failures in that location did not involve the prior formation of shear bands. Instead, they looked more like the ductile shear failures presented in Figure 84 that are responsible for plugging perforations of low-carbon or ductile steel targets (Reference 21). Concentrated shear bands were found along the impact surface of the blunt aluminum cylinder that had been severely deformed (mushroomed) within the target, as depicted in Figures 85 and 86. This may be indicative of the greater degree of deformation experienced by the projectile in this instance and may also reflect differences in the initial processing treatments experienced by the projectile alloy prior to testing compared to the target material.

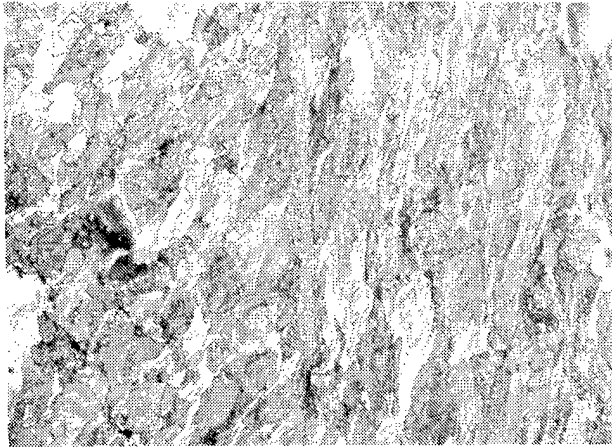


FIGURE 76. Micrograph of Concentrated Shear Band Adjacent to Impact Crater in the Target Shown in Figure 75. (400X magnification.)

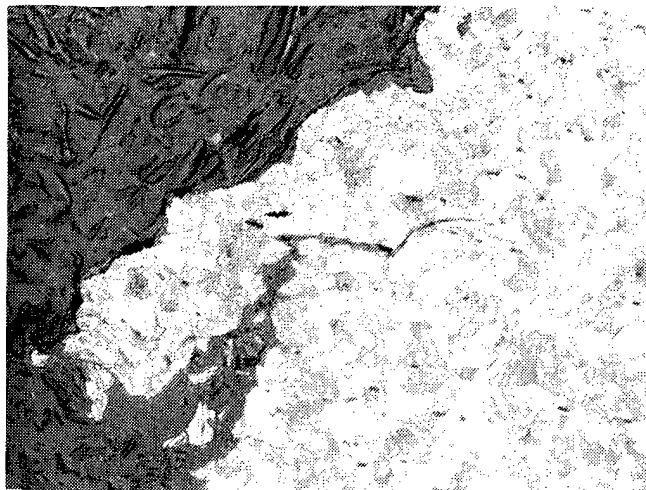


FIGURE 77. Micrograph of Brittle-Appearing Fracture Surface Near the Distal Side of the Perforation Crater Shown in Figure 75. (200X magnification.)



FIGURE 78. Section View of the Crater in a 6.35-mm-Thick Steel Target Struck by a 12.7-mm Conical-Tipped Steel Cylinder at 30 Degrees Obliquity and a Speed of 325 m/s. Initial penetration path shown by arrow (projectile ricocheted). (Run C-18.)

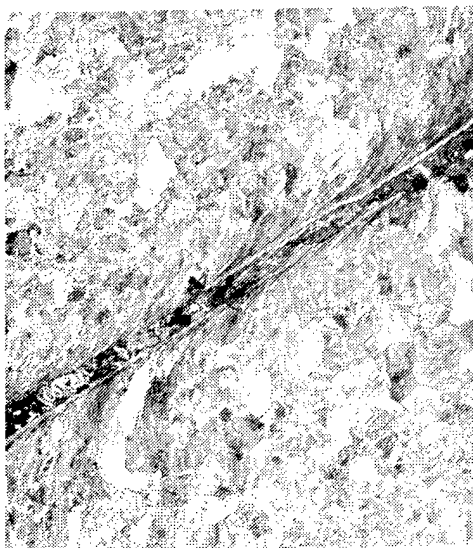


FIGURE 79. Micrograph of Fractured Concentrated Shear Band in the Target Shown in Figure 78. (200X magnification.)

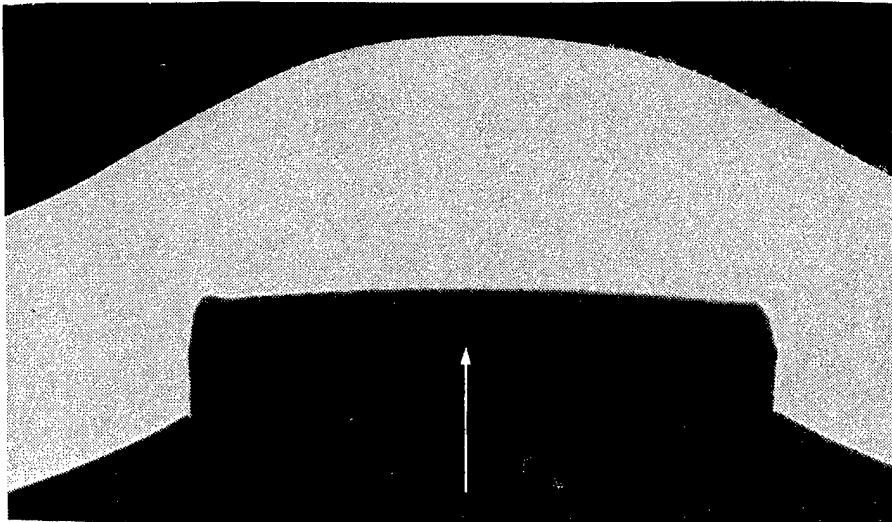


FIGURE 80. Section View of the Crater Formed in a 6.35-mm-Thick Aluminum Target Struck by a 12.7-mm Blunt-Ended Aluminum Cylinder at a Speed of 265 m/s. Penetration path shown by arrow (projectile embedded and was subsequently removed). (Run C-122.)

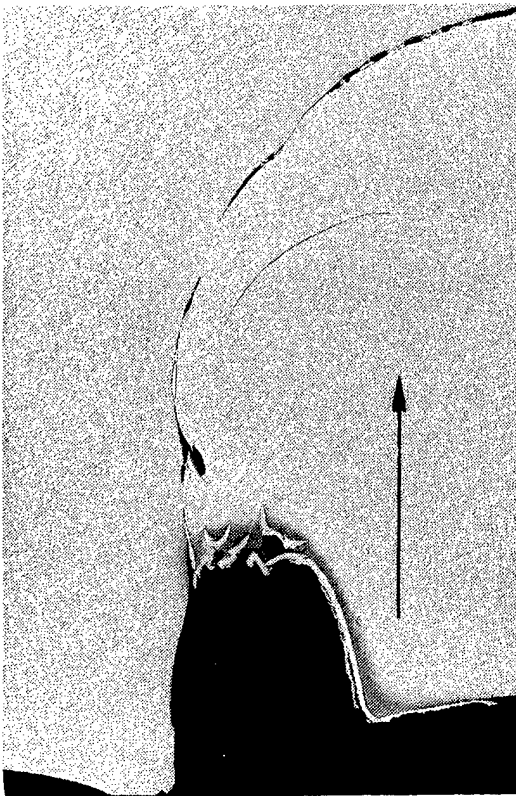


FIGURE 81. Section View of One Side of the Crater Formed in a 25.4-mm-Thick Aluminum Target by the Impact of a 12.7-mm Blunt-Ended Aluminum Cylinder at a Speed of 921 m/s. Penetration path shown by arrow (projectile embedded and mushroomed). (Run C-110.)

FIGURE 82. Section View of One Side of the Crater Formed in a 12.7-mm-Thick Aluminum Target Perforated by a 12.7-mm-Diameter Blunt-Ended Steel Cylinder Initially Traveling at 594 m/s. Penetration path shown by arrow. (Run C-124.)



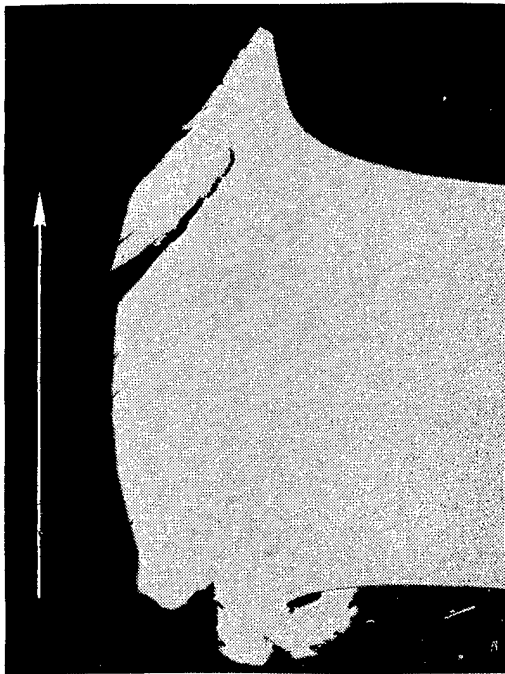
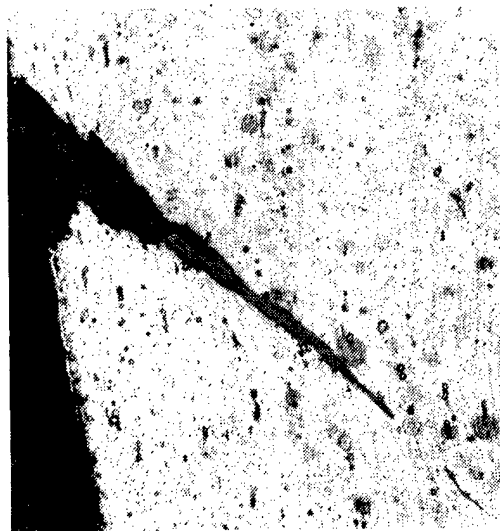


FIGURE 83. Section View of One Side of the Crater Formed in a 6.35-mm-Thick Aluminum Target Perforated by a Conical-Tipped Steel Cylinder Initially Traveling at 915 m/s. Penetration path shown by arrow. (Run C-5.)

FIGURE 84. Micrograph of Shear Fracture Adjacent to Impact Crater in Target Shown in Figure 82. (100X magnification.)



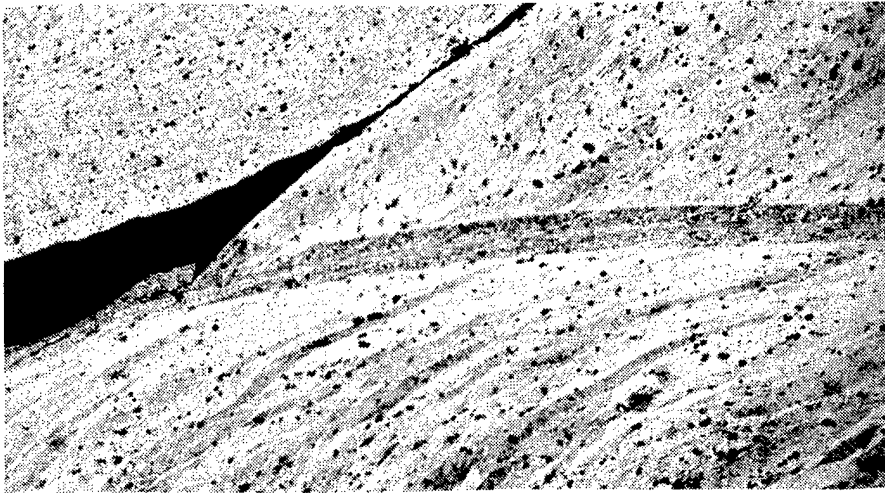


FIGURE 85. Micrograph of Concentrated Shear Band Adjacent to the Impact Surface in a Mushroomed Aluminum Cylinder Shown in Figure 81. (100X magnification.)

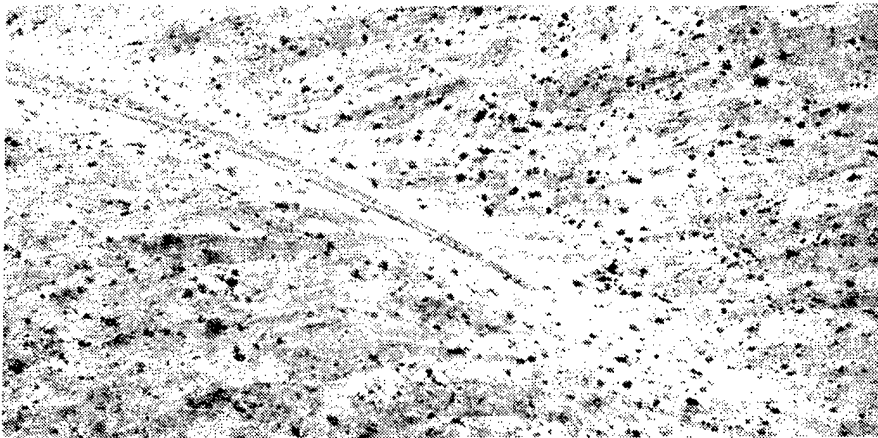


FIGURE 86. Micrograph of Inward Terminus of Concentrated Shear Band Seen in Figure 85. (100X magnification.)

CONCLUSIONS

Approximately 200 tests were conducted to determine the velocity drop and change in angular orientation of projectiles striking soft aluminum and mild and medium-carbon steel plates at angles of obliquity ranging from normal to 50 degrees over the velocity range from about 20 to 1025 m/s. Impacts in the lower speed range were generated by a pneumatic device, whereas those above 200 m/s were achieved by means of a powder gun. The targets, whose thickness ranged from 1.25 to 25.4 mm, were clamped on a 114.7-mm-diameter ring in a holder whose configuration prevented employment of greater angles of attack without the certainty of projectile ricochet. The strikers were composed of hard-steel or soft aluminum cylinders of 12.7 mm nominal diameter with blunt or 60-degree conical nose shapes for the former and only blunt noses for the latter.

The ballistic limit of a 3.175-mm-thick 2024-0 aluminum target struck by a 60-degree cylindro-conical steel projectile was found to be about 95 m/s at normal incidence; a slight increase in this value was noted with increasing obliquity up to 55 degrees. On the other hand, a 12.7-mm-thick target of this type struck at 40 degrees by a blunt steel projectile evidenced a ballistic limit of 600 m/s, whereas the limit for the normal impact of the same striker on a 19.05-mm-thick plate of this material was 305 m/s. The sharp-nosed projectile was stopped by a 3.175-mm-thick mild steel target at 195 m/s at normal incidence, whereas a 19.05-mm-thick mild steel plate exhibited a limit of 905 m/s when struck normally by a blunt aluminum projectile. The final obliquity angle increased more rapidly with initial angle of incidence for 3.175-mm-thick aluminum targets, but varied nearly linearly with this parameter for 6.35-mm-thick aluminum plates and both thicknesses for mild steel. Photographs of the crater resulting from projectile embedment or perforation clearly showed the petalling nature of the phenomenon for cylindrical noses and the plug removal, together with a brittle band separation on the distal plate side for blunt-nosed strikers, both at normal incidence. Obliquity completely alters the petal pattern for both types of targets, with petals more frequently shorn from the target plate for aluminum and a somewhat larger number of distal side petals at low obliquity just above the ballistic limit for steel. Large angles of obliquity in the latter material produced lips on the distal side with brittle fracture evident on the opposite crater side.

The initiation of fracture in thin aluminum plates subjected to normal incidence by cylindrically tipped projectiles was carefully studied by slight variation of the initial velocity. The first evidence of deformation was found to be a bulge without a crack evident on the distal side; the impact side exhibited a conical crater.

This was followed by crack initiation, generally by two sets of cracks crossing at right angles, that leads to the familiar four- or five-petal combination at higher velocities. However, in at least one case, a single linear crack was formed at a particular speed. Symmetry of the bulges and holes generated for normal impact was established by profilometer measurement.

In general, the hard-steel strikers remained intact with either no or slight plastic deformation as the result of plate perforation. However, at higher impact speeds with thicker steel targets, these sometimes broke into a relatively small number of parts. Under extreme conditions, such strikers shattered and only a small portion of the rearward sections could be recovered. Aluminum strikers mushroomed as the result of processes quite similar to the generation of the Munroe jet. Plugs produced by impact of blunt-nosed strikers also exhibited some sideways deformation and curved surfaces were frequently noted on both lateral edges. An unusual case of both plugging and petalling of an aluminum target struck normally by an aluminum projectile was noted at a high initial velocity.

The force histories generated by the impact of a striker at normal incidence on a 3.175-mm-thick 2024-0 aluminum target did not differ significantly under conditions of shank embedment and complete perforation just above the ballistic limit. It is speculated that the curves will not significantly change at substantially higher velocity except for the gradual disappearance of the knee found in the rising portion of the curve that is attributed to crack initiation. Some similarities and some differences are observed between these curves and that reported for a hemispherically tipped cylindrical striker where plugging rather than petalling occurs.

Metallurgical examination of the virgin and perforated targets indicated preferred orientations of the material, associated with direction of rolling, which affect the direction of initial cracking. Substantial evidence of shear banding due to localized adiabatic shear was observed in both projectiles and targets. Propagation of these zones is considered to be a controlling factor in the plugging process, whereas petalling and the removal of bands from distal target surfaces represents a tensile fracture phenomenon.

REFERENCES

1. M. E. Backman and W. Goldsmith. "The Mechanics of Penetration of Projectiles Into Targets," Int. J. Eng. Sci., Vol. 16, 1978, pp. 1-99.
2. W. Goldsmith and S. A. Finnegan. "Penetration and Perforation Processes in Metal Targets at and Above Ballistic Velocities," Int. J. Mech. Sci., Vol. 13, 1971, pp. 843-66.
3. J. Awerbuch and S. R. Bodner. "Analysis of the Mechanics of Perforation of Projectiles in Metallic Plates," Int. J. Solids and Structures, Vol. 10, 1974, pp. 671-84.
4. J. Liss, W. Goldsmith, and J. M. Kelly. "A Phenomenological Penetration Model of Thin Plates," Int. J. Impact Eng., Vol. 1, 1983, pp. 321-41.
5. J. Liss and W. Goldsmith. "Plate Perforation Phenomena Due to Normal Impact by Blunt Cylinders," Int. J. Impact Eng., Vol. 2, 1984, pp 37-64.
6. B. Landkof and W. Goldsmith. "Petalling of Thin, Metallic Plates During Penetration by Cylindro-Conical Projectiles," Int. J. Solids Structures (in press).
7. N. Levy and W. Goldsmith. "Normal Impact and Perforation of Thin Plates by Hemispherically-Tipped Projectiles, I. Analytical Considerations," Int. J. Impact Eng., Vol. 2, 1984, pp. 209-29.
8. _____. "Normal Impact and Perforation of Thin Plates by Hemispherically-Tipped Projectiles, II. Experimental Results," Int. J. Impact Eng., Vol. 2, 1984, pp.299-324.
9. R. F. Recht and T. W. Ipson. "Ballistic Perforation Dynamics," J. Appl. Mechanics, Vol. 30, 1963, pp. 384-90.
10. R. L. Woodward and M. E. DeMorton. "Penetration of Targets by a Flat-Ended Projectile," Int. J. Mech. Sci., Vol. 18, 1976, pp. 119-27.
11. J. Nishiwaki. "Resistance to the Penetration of a Bullet Through an Aluminum Plate," J. Phys. Soc. Japan, Vol. 6, 1951, pp. 374-78.

12. B. Paul and M. Zaid. "Oblique Perforation of a Thin Plate by a Truncated Conical Projectile," J. Franklin Inst., Vol. 268, 1959, pp. 24-45.
13. Naval Weapons Center. Dynamics of the Oblique Impact and Ricochet of Nondeforming Spheres Against Thin Plates, by M. E. Backman and S. A. Finnegan. China Lake, Calif., NWC, August 1976. (NWC TP 5844, publication UNCLASSIFIED.)
14. M. E. Backman, S. A. Finnegan, and K. G. Whitham. "Dynamics of the Oblique Impact and Ricochet of Nondeforming Projectiles Against Thin Plates," Proc. of the 14th Annual Meeting of the Society for Engineering Science, 14-16 November 1977. Bethlehem, Pa., Lehigh University. Pp. 9-20.
15. J. Awerbuch and S. R. Bodner. "An Investigation of Oblique Perforation of Metallic Plates by Projectiles," Experimental Mechanics, Vol. 17, 1977, pp. 147-153.
16. Army Ballistic Research Laboratories. Ricochet and Penetration of Steel Spheres Impacting Aluminum Targets, by J. Zook, W. Slack, and B. Izdebski. BRL, Aberdeen Proving Ground, Md., February 1983. (Memorandum Report ARBRL-MR-02343, publication UNCLASSIFIED.)
17. L. E. Samuels and I. R. Lamborn. "Failures of Armament Hardware," Metallography in Failure Analysis, ed. by James L. McCall and P. M. French, New York, Plenum Press, 1978. Pp. 167-90.
18. Harry C. Rogers. "Adiabatic Plastic Deformation," Ann. Rev. Mater. Sci., Vol. 9, 1979, pp. 283-311, Annual Reviews, Inc., Palo Alto, Calif.
19. A. J. Bedford, A. L. Wingrove, and K. R. L. Thompson. "The Phenomenon of Adiabatic Shear Deformation," J. Australian Inst. of Metals, Vol. 19, No. 1, (1974), pp. 61-73.
20. Charles S. Barrett and T. B. Massalski. Structure of Metals, New York, McGraw-Hill, 1966.
21. Naval Weapons Center. Experimental Data for Characterizing Perforating Impacts: Fragmentation Processes, by Marvin E. Backman and Stephen A. Finnegan. China Lake, Calif., NWC (in process). (NWC TP 6490, publication UNCLASSIFIED.)

INITIAL DISTRIBUTION

- 8 Naval Air Systems Command
 - AIR-301 (2)
 - AIR-320, B. Warren (1)
 - AIR-320D (1)
 - AIR-541 (2)
 - AIR-7226 (2)
- 5 Chief of Naval Operations
 - OP-03 (2)
 - OP-05 (1)
 - OP-098 (1)
 - OP-55 (1)
- 1 Chief of Naval Material (MAT-05)
- 3 Chief of Naval Research, Arlington
 - ONR-102 (1)
 - ONR-461 (1)
 - ONR-474 (1)
- 7 Naval Sea Systems Command
 - SEA-09B312 (2)
 - SEA-62R (5)
- 1 Commander in Chief, U.S. Pacific Fleet (Code 325)
- 1 Air Test and Evaluation Squadron 5
- 1 Commander, Third Fleet, Pearl Harbor
- 1 Commander, Seventh Fleet, San Francisco
- 1 David W. Taylor Naval Ship Research and Development Center, Bethesda
- 2 Naval Academy, Annapolis (Director of Research)
- 1 Naval Air Force, Atlantic Fleet
- 2 Naval Air Force, Pacific Fleet
- 1 Naval Air Station, North Island
- 2 Naval Air Test Center, Patuxent River (CT-252, Bldg. 405)
- 1 Naval Avionics Center, Indianapolis (Technical Library)
- 1 Naval Explosive Ordnance Disposal Technology Center, Indian Head
- 1 Naval Ocean Systems Center, San Diego (Code 447)
- 1 Naval Ordnance Station, Indian Head (Technical Library)
- 1 Naval Postgraduate School, Monterey
- 3 Naval Ship Weapon Systems Engineering Station, Port Hueneme
 - Code 5711, Repository (2)
 - Code 5712 (1)
- 3 Naval Surface Weapons Center, Dahlgren
 - G13
 - D. Dickinson (1)
 - T. Wasmund (1)
 - G22, W. Holt (1)
- 5 Naval Surface Weapons Center, White Oak Laboratory, Silver Spring
 - R10, S. Jacobs (1)
 - R12, J. Erkman (1)
 - R13, R. Liddiard (1)
 - Guided Missile Warhead Section (1)
 - Technical Library (1)

NWC TP 6479

- 1 Naval War College, Newport
- 1 Office of Naval Research, Pasadena Branch Office
- 1 Office of Naval Technology, Arlington (MAT-07)
- 1 Operational Test and Evaluation Force, Atlantic
- 2 Pacific Missile Test Center, Point Mugu
 - Code 1245, Nofrey (1)
 - Technical Library (1)
- 1 Marine Corps Air Station, Beaufort
- 1 Army Armament Munitions and Chemical Command, Rock Island (DRSAR-LEP-L, Technical Library)
- 4 Army Armament Research and Development Command, Dover
 - DRDAR-LCU-SS, J. Pentel (1)
 - Technical Library (3)
- 1 Aberdeen Proving Ground (Development and Proof Services)
- 10 Army Ballistic Research Laboratory, Aberdeen Proving Ground
 - AMSAA
 - C. Alston (1)
 - Blomquist (1)
 - AMXAR-SEI-B (1)
 - AMXAR-T, Detonation Branch (1)
 - AMXAR-TSB-S (STINFO) (1)
 - AMXBR-TBD
 - J. Dahn (1)
 - J. Kenecke (1)
 - AMXBR-VLDA, T. Bentley (1)
 - AMXSY-AD (1)
 - AMXSY-J (1)
- 1 Army Materiel Systems Analysis Activity, Aberdeen Proving Ground (K. Meyers)
- 21 Army Research Office, Research Triangle Park
 - DRXPO-IP-L, Information Processing Office (1)
 - Dr. E. Saible (20)
- 1 Harry Diamond Laboratories, Adelphi (Technical Library)
- 1 Radford Army Ammunition Plant
- 1 Redstone Arsenal (Rocket Development Laboratory, Test and Evaluation Branch)
- 2 Rock Island Arsenal
 - Navy Liaison Office (NVLNO) (1)
 - Technical Library (SARRI-ADM-P) (1)
- 1 White Sands Missile Range (STEW-AD-L)
- 1 Yuma Proving Grounds (STEYT-GTE, M&W Branch)
- 1 Tactical Air Command, Langley Air Force Base (TPL-RQD-M)
- 1 Air Force Armament Division, Eglin Air Force Base (AFATL/DLJW)
- 1 Air Force Armament Division, Eglin Air Force Base (AFATL/DLODL, Technical Library)
- 1 Air Force Armament Division, Eglin Air Force Base (AFATL/DLYV, K. McArdle)
- 1 Air Force Armament Division, Eglin Air Force Base (AFATL/DLYV, A. Rutland)
- 1 Air Force Intelligence Service, Bolling Air Force Base (AFIS/INTAW, Maj. R. Lecklider)
- 1 Air University Library, Maxwell Air Force Base
- 1 Tactical Fighter Weapons Center, Nellis Air Force Base (CC/CV)
- 2 57th Fighter Weapons Wing, Nellis Air Force Base
- 1 554th Combat Support Group, Nellis Air Force Base (OT, FWW/DTE)
- 1 554th Combat Support Group, Nellis Air Force Base (OT, FWW/DTO)
- 1 Defense Advanced Research Projects Agency, Arlington (Materials Science Division, Snow)
- 1 Defense Nuclear Agency (Shock Physics Directorate)
- 12 Defense Technical Information Center
 - 1 Department of Defense-Institute for Defense Analyses Management Office (DIMO), Alexandria
- 2 Colorado Seminary, Denver Research Institute, Denver, CO
 - R. Recht (1)
 - J. Yatteau (1)
- 1 Lewis Research Center (NASA), Cleveland
- 1 California Institute of Technology, Jet Propulsion Laboratory, Pasadena, CA (Technical Library)
- 2 Hercules Incorporated, Allegany Ballistics Laboratory, Cumberland, MD
- 1 IIT Research Institute, Chicago, IL (Department M, Document Librarian)

- 1 Los Alamos National Laboratory, Los Alamos, NM (Reports Library)
- 1 Princeton University, Forrestal Campus Library, Princeton, NJ
- 1 Stanford Research Institute, Poulter Laboratories, Menlo Park, CA
- 1 The Boeing Company, Seattle, WA (MS 8C-61, E. Wilhelm)
- 2 The Johns Hopkins University, Applied Physics Laboratory, Laurel, MD (Document Library)
- 2 The Johns Hopkins University, Applied Physics Laboratory, Chemical Propulsion Information Agency,
Laurel, MD
- 1 The Rand Corporation, Santa Monica, CA (Technical Library)
- 10 University of California, Berkeley, CA (Prof. W. Goldsmith)
- 1 University of California, Lawrence Livermore National Laboratory, Livermore, CA (Code L39, Landingham)